

**SEMICONDUCTOR IN-LINE FIBER DEVICES FOR OPTICAL
COMMUNICATION SYSTEMS**

**A DISSERTATION SUBMITTED TO THE DEPARTMENT OF
ELECTRICAL ENGINEERING AND THE COMMITTEE ON
GRADUATE STUDIES OF STANFORD UNIVERSITY IN PARTIAL
FULFILLMENT OF THE REQUIREMENTS FOR THE DEGREE OF
DOCTOR OF PHILOSOPHY**

Erji Mao

June 2000

© Copyright by Erji Mao 2000

All Rights Reserved

I certify that I have read this dissertation and that in my opinion it is fully adequate, in scope and quality, as a dissertation for the degree of Doctor of Philosophy.

Prof. James S. Harris, Jr. (Principal Advisor)

I certify that I have read this dissertation and that in my opinion it is fully adequate, in scope and quality, as a dissertation for the degree of Doctor of Philosophy.

Prof. David A. B. Miller

I certify that I have read this dissertation and that in my opinion it is fully adequate, in scope and quality, as a dissertation for the degree of Doctor of Philosophy.

Prof. Olav Solgaard

Approved for the University Committee on Graduate Studies:

Abstract

Optical fibers are becoming increasingly important for communication systems because of their large bandwidth and low propagation losses. The rapid growth of the fiber-optic industry has resulted in significant research effort being directed towards the development of high-performance, low cost optoelectronic devices, such as diode lasers, modulators and detectors. Traditionally, the fabrication of fiber-coupled devices involves the interruption of the fiber and the insertion of the device. Several drawbacks are associated with this approach, including high insertion loss, mechanical instability, and high packaging costs. In-line fiber devices, in which light is evanescently coupled between single mode fibers and multimode high index waveguides, offer solutions to these problems.

This work focuses on gallium arsenide (GaAs) based in-line devices. GaAs and other compound semiconductors offer advantages over other materials such as lithium niobate, electro-optic polymer and liquid crystal, in that they can be monolithically integrated with lasers and high-speed electronics, thereby reducing fabrication costs. The difficulty in phase-matching the modes of the single mode fiber and the GaAs waveguide, which are made of materials of vastly different refractive indices, is overcome by the use of dielectric mirrors in the semiconductor structure. The demonstrated devices include a filter with a minimum linewidth of 0.5nm, a wavelength selective detector with a linewidth of 1.6nm and a external quantum efficiency of 75%, an intensity modulator with an on/off ratio of 4:1, as well as a resonant light emitter. The theory, design, fabrication and characterization of these novel optoelectronic devices are discussed in detail.

Acknowledgements

A number of people have contributed to this work. First and foremost I would like to thank my advisor, James Harris, who has created an open research environment in which students are given incredible freedom in pursuit of their research interests. The qualities of self-guidance and self-motivation that I have acquired over the last few years will surely benefit me for the rest of my career.

I would like to thank Prof. David Miller, Prof. Olav Solgaard for serving both on my oral defense committee and on my reading committee. Prof. Solgaard should also be thanked for his role in initiating the work described in this dissertation. I am grateful to Prof. Len Tyler for agreeing to be my oral committee chairman while still on sabbatical.

A large part of this work was done at the University of California at Davis, where Prof. Andre Knoblesdorff generously agreed to let me use his laboratory facilities. Dr. Diego Yankelevich has been very helpful when it comes to discussions about fiber half couplers, as well as building the measurement setup.

There are a number of past and present Harris group members who deserve credit for their help and support. John Trezza got me started on the path of photonic device research. The MBE gurus — Chris Coldren and Chien-Chung Lin, grew all the wafers for this work. Alan Massengale and Guoying Ding taught me the basics of GaAs device processing. Wayne Martin, Vijit Sabnis, Barden Shimbo, Vincent Gambin and Hong Liu helped maintain the various computer systems for the group. Martijn Vugts showed me how to use the HP Advanced Design System for transmission line simulations. Gail Chun-Creech and Lu Miao deserve special thanks for their administrative skills.

Finally I would like to thank my family and friends for their support before and during my years at Stanford. I am especially indebted to my parents for their unconditional love, and for teaching me early on the importance of intellectual independence.

The work for this dissertation was funded by the Defense Advanced Research Project Agency and the Office of Naval Research under contract #N00014-98-1-0537.

Table of Contents

1. INTRODUCTION	1
1.1 INTRODUCTION	1
1.1.1 Why fiber optics	1
1.1.2 In-line fiber devices	2
1.2 ORGANIZATION	5
2. THEORETICAL BACKGROUND	6
2.1 PLANAR DIELECTRIC WAVEGUIDE	6
2.2 TRANSFER MATRIX METHOD FOR ANALYZING MULTI-LAYER WAVEGUIDES	8
2.3 OPTICAL FIBERS	11
2.4 EVANESCENT WAVE COUPLING	15
3. ARROW AND COUPLED WAVEGUIDE SIMULATION	18
3.1 GaAs/AlGaAs MATERIAL SYSTEM	18
3.2 ANTI-RESONANT REFLECTIVE OPTICAL WAVEGUIDES	19
3.2.1 Distributed Bragg reflector mirrors	20
3.2.2 ARROW design example	22
3.3 COUPLED-MODE ANALYSIS OF ARROW-FIBER SYSTEMS	24
3.3.1 Propagation losses in an ARROW	25
3.3.2 Coupling strength between a fiber and an ARROW	29
3.3.3 Coupled ARROW-fiber waveguide system	31
4. IN-LINE FIBER FILTER AND DETECTOR	33
4.1 EPITAXIAL GROWTH	33
4.2 IN-LINE FIBER FILTER	35
4.2.1 Device design	35
4.2.2 Experiment	37
4.2.3 Results and discussion	38
4.3 WAVELENGTH SELECTIVE IN-LINE FIBER PHOTODETECTOR	41

4.3.1 Device design	41
4.3.2 Experiment	43
4.3.3 Results and discussion	44
5. IN-LINE FIBER MODULATOR	46
5.1 QUANTUM WELL PHYSICS	46
5.1.1 Quantum confined Stark effect	46
5.1.2 Kramers-Kronig relations	51
5.2 MODULATOR WITH SINGLE-MIRROR ARROW	53
5.2.1 Device design	53
5.2.2 Experimental results and discussion	54
5.3 MODULATOR WITH DOUBLE-MIRROR ARROW	57
5.3.1 Device design	57
5.3.2 Experimental results	58
5.3.3 Discussion	59
5.4 SIMULATION OF TRAVELING WAVE MODULATORS	62
5.4.1 Transmission line basics	63
5.4.2 Electrode design	65
5.4.3 Frequency response	69
6. IN-LINE FIBER LIGHT EMITTER	73
6.1 DEVICE DESIGN AND EXPERIMENT	73
6.2 RESULTS AND DISCUSSION	74
7. CONCLUSION	78
7.1 SUMMARY	78
7.2 SUGGESTIONS FOR FUTURE WORK	79
APPENDIX A: DERIVATION OF MICROWAVE RESISTIVE LOSS CAUSED BY A DOPED SEMICONDUCTOR LAYER	81

**APPENDIX B: SIMULATION OF NON-PLANAR TRANSMISSION
LINES USING HP MOMENTUM** **84**

REFERENCES **87**

List of Tables

Table 3-1. The calculated coupling characteristics between a single mode fiber and
an ARROW.

30

List of Figures

Fig. 1-1. The basic elements of a fiber-optic communication system.	2
Fig. 1-2. Two different approaches to coupling an optical fiber to information processing elements: (a) conventional “insertion” method, and (b) in-line fiber architecture where evanescent wave coupling occurs.	3
Fig. 1-3. The schematic of a GaAs in-line fiber device. The fiber is side-polished so that the remaining cladding thickness is about $1\mu\text{m}$.	4
Fig. 2-1. A planar dielectric waveguide. A mode is represented as a TEM plane wave bouncing between the surfaces of the core. The lines AB and BC are perpendicular to each other.	7
Fig. 2-2. The incidence of a plane wave at an angle θ_0 onto a layered structure.	9
Fig. 2-3. Schematic of a step index optical fiber.	11
Fig. 2-4. Illustration of the graphical approach to solving the characteristic equation (2-19). The left-hand and right-hand sides are plotted as functions of k, a . The intersections are the solutions.	14
Fig. 2-5. The field intensity distribution of a typical single mode fiber operating at 830nm. The parameters are $n_1=1.4583358$, $n_2=1.45253$ and $a=2.27\mu\text{m}$.	14
Fig. 2-6. Coupling between two waveguides. The optical field in waveguide 1 overlaps slightly with the core of waveguide 2, which induces gradual power transfer. On the left, light is mostly in waveguide 1, while on the right, it is mostly in waveguide 2.	15
Fig. 2-7. Exchange of power between two waveguides: (a) when the two guides are phase-matched; (b) when the two guides are not phase-matched.	16
Fig. 3-1. An illustration of a conventional dielectric slab waveguide (a) and an ARROW (b). In (a), the mode angle θ has to be larger than the critical angle ($\sin^{-1}(n_{\text{cladding}}/n_{\text{core}})$) for a guided mode, while in (b), θ can be independent of the core and mirror indices.	19
Fig. 3-2. Schematic of a DBR mirror. The drawing on the right illustrates the incident and reflected rays for a constituent layer in a DBR structure.	20

Fig. 3-3. The calculated reflectivity for a DBR with 25 pairs of AlAs/Al _{0.33} Ga _{0.67} As (791Å/671Å). The incident medium is Al _{0.33} Ga _{0.67} As. (a) Reflectivity as a function of wavelength for a 25° incident angle; (b) Reflectivity as a function of angle at 8300Å. TE (TM) polarization means that the incident electric (magnetic) field components lies in the plane of the layers.	21
Fig. 3-4. Structure of a GaAs/AlGaAs ARROW designed to phase-match to a single mode fiber at 830nm.	22
Fig. 3-5. The calculated TE optical transmission of the ARROW structure as a function of the propagation index (at 830nm). The peak corresponds to an effective index of 1.4553, which is the same as the fiber propagation index.	23
Fig. 3-6. The calculated dispersion curves for the fiber mode and the highest order confined ARROW mode (TE).	23
Fig. 3-7. The calculated field profile for the highest order confined mode in the ARROW (TE). The wavelength is 830nm.	24
Fig. 3-8. A propagating Gaussian beam.	25
Fig. 3-9. The calculated power decay due to lateral diffraction in a planar waveguide. The thick line is based on the Gaussian beam expansion model and the thin line is an exponential fit.	27
Fig. 3-10. An illustration of an ARROW with propagation losses: mirror leakage and core material absorption.	27
Fig. 3-11. The fiber in the polished half coupler shown on the left can be replaced by its equivalent slab waveguide shown on the right.	29
Fig. 3-12. The calculated field profiles for the two coupled modes of the ARROW-fiber structure. The solid line corresponds to the bonding state (higher effective index), and the dashed line corresponds to the anti-bonding state (lower effective index).	31
Fig. 3-13. The calculated fiber transmission of a coupled ARROW-fiber waveguide system. The coupling coefficient is 0.004μm ⁻¹ , and the values in the legend are the propagation losses in the ARROW.	32
Fig. 3-14. The calculated fiber transmission of a coupled ARROW-fiber	

waveguide system. The ARROW propagation loss is $0.01\mu\text{m}^{-1}$, and the values in the legend are the coupling coefficients.	32
Fig. 4-1. Illustration of the MBE growth of gallium arsenide.	34
Fig. 4-2. The calculated difference in propagation constants between the fiber mode and the TE ARROW mode. The three curves represent three ARROWS with the same DBR (as the one shown in Fig. 4-3) but different core thicknesses (core material = $\text{Al}_{0.33}\text{Ga}_{0.67}\text{As}$). The unit for y-axis is μm^{-1} .	36
Fig. 4-3. The epitaxial structure of the ARROW used in the filter.	36
Fig. 4-4. The calculated dispersion curves for the single mode fiber and the highest order confined mode of the ARROW. The y-axis shows the effective propagation indices.	37
Fig. 4-5. The experimental setup for testing in-line fiber filters.	38
Fig. 4-6. (a) The measured transmission spectra at 25°C ; (b) The simulated spectra. The parameters used for the simulation are: $C = 0.005\mu\text{m}^{-1}$, $\alpha = 0.003\mu\text{m}^{-1}$ (TE) and $\alpha = 0.018\mu\text{m}^{-1}$ (TM).	39
Fig. 4-7. The experimental TE (a) and TM (b) transmission spectra of the in-line fiber filter under different temperatures.	40
Fig. 4-8. Cross section views of an in-line fiber filter. The drawing on the left depicts the current device. The drawing on the right shows an ARROW with a ridge structure for controlling lateral diffraction.	40
Fig. 4-9. The epitaxial structure of the ARROW used in the in-line detector.	41
Fig. 4-10. The structures of two ARROWS: (a) with a leaky DBR, and (b) without a leaky DBR. The phase-matched wavelength is 830nm for both waveguides.	42
Fig. 4-11. The calculated dispersion characteristics of the two ARROWS illustrated in Fig. 4-10.	43
Fig. 4-12. Illustration of photodetector testing arrangement: (a) cross-sectional view, and (b) top view.	44
Fig. 4-13. (a) The measured photocurrent response. (b) The measured device transmission.	45

Fig. 5-1. Schematic of a semiconductor absorption spectrum. Coulomb interaction not only creates excitonic resonances below the bandgap, but also enhances the above-bandgap continuum absorption.	47
Fig. 5-2. Illustration of the change in confinement energies and wave function overlap when a perpendicular electric field is applied to a quantum well.	49
Fig. 5-3. The measured absorption spectra for 75Å GaAs quantum wells with 35Å AlAs barriers. The polarization of the light is TE (parallel to the MQW plane). Details of the experimental procedures can be found in reference 34.	50
Fig. 5-4. The calculated refractive index for 75Å GaAs quantum wells with 35Å AlAs barriers. The index changes with respect to bulk GaAs values are calculated using the Kramers-Kronig relationship. The bulk GaAs index values are taken from reference 11.	52
Fig. 5-5. The epitaxial structure of the MQW single mirror ARROW used in the Modulator.	53
Fig. 5-6. The calculated TE absorption (a) and refractive index (b) values for the MQW in the modulator. At 0V, the built-in electric field of the device is 45kV/cm, and at 5V reverse bias, the electric field is 150kV/m. The refractive index was calculated using the absorption data and the Kramers-Kronig relationship.	54
Fig. 5-7. The TE transmission spectra for: (a) device #1, which is near the center of the wafer; (b) device #2, which is halfway between the center and the edge of the wafer; (c) device #3, which is near the edge of the wafer.	55
Fig. 5-8. The band diagram of a reverse-biased p-i-n junction. The thin p-type contact layers can be completely depleted at high biases, therefore electrons can tunnel from the metal contact to the intrinsic region, causing junction breakdown.	56
Fig. 5-9. The detailed epitaxial structure of the double mirror ARROW structure. The intrinsic MQW core region is surrounded by a highly reflective DBR (n-doped) and a leaky DBR (p-doped).	57
Fig. 5-10. The calculated TE effective propagation indices for the ARROW and the	

fiber. The ARROW mode is the highest order confined mode.	58
Fig. 5-11. (a) The transmission spectra of the modulator under different bias conditions. (b) Transmission at 845.5nm as a function of applied bias.	59
Fig. 5-12. An illustration of the “double dip” effect in the experimental transmission spectra: (a) and (c) are the assumed wavelength-dependent ARROW propagation loss at two different biases; (b) and (d) show the corresponding transmission spectra calculated with the coupled-mode equations and the dispersion relations shown in Fig. 5-10. The assumed coupling coefficient is 3mm^{-1} , and the interaction length is 1mm.	60
Fig. 5-13. The transmission spectra of a 5mm long in-line modulator, as calculated with the coupled-mode equations. The low- and high-loss cases correspond to the ARROW absorption curves shown in Fig. 5-12a and 5-12c.	61
Fig. 5-14. The calculated transmission spectra of an in-line modulator with a tapered ARROW. The coupling coefficient is 3mm^{-1} for (a) and 8mm^{-1} for (b).	61
Fig. 5-15. The concept of a traveling wave modulator: the modulation signal (electrical) travels at the same speed as the modulated signal (optical).	62
Fig. 5-16. (a) A parallel plate transmission line; (b) A planar microstrip transmission line.	64
Fig. 5-17. The cross-sectional view of a traveling wave electrode design for an in-line fiber modulator.	66
Fig. 5-18. (a) The actual transmission line structure; (b) The model used for HP Momentum calculation.	67
Fig. 5-19. The calculated characteristic impedance (a), effective propagation index (b), and the attenuation coefficient (c) of the traveling wave electrode structure shown in Fig. 5-17.	68
Fig. 5-20. The transmission line model used to calculate the modulator frequency response.	69
Fig. 5-21. The calculated frequency responses for 1mm long devices (a) with only a fiber, and (b) with a fiber block.	70
Fig. 5-22. Top view of microwave probing arrangements: (a) with only a fiber	

where no extra sections of transmission line are needed for microwave input and termination; (b) with fiber block where extra sections are needed to connect the microwave input and termination to the polished interaction region.	71
Fig. 5-23. The calculated frequency responses for devices with different interaction lengths, assuming that no fiber block is used.	72
Fig. 6-1. The cross-sectional view of the light-emitting device testing arrangement.	74
Fig. 6-2. The measured emission spectra as a function of injection currents.	75
Fig. 6-3. The calculated transmission spectra of the device for different ARROW propagation gains. The calculation was performed using the coupled-mode equations (described in Chapter 3), with an assumed coupling constant of 3mm^{-1} .	76
Fig. 6-4. The transmission spectra under different current injection levels for TE-polarized light (a) and TM polarized light (b).	76
Fig. 6-5. The band diagram of a semiconductor quantum well. The split in the heavy and light hole bands results in most injected holes falling into heavy hole states.	77
Fig. 7-1. Two possible configurations for an in-line fiber coupled semiconductor laser: (a) the feedback loop is formed between a fiber Bragg grating and a HR-coated air-semiconductor interface; (b) the feedback loop is formed between two fiber Bragg gratings.	80
Fig. A-1. (a) The physical structure of a p-i-n diode with a p-contact; (b) An equivalent circuit model used to simulate the situation in (a).	81
Fig. B-1. (a) The experimental transmission line structure. The dimensions are: $d=2.3\mu\text{m}$, $s=6\mu\text{m}$, $w=3\mu\text{m}$, $h=0.9\mu\text{m}$, $g=2.5\mu\text{m}$ and $d_p=0.8\mu\text{m}$. The contact metal (Au) thickness is $0.6\mu\text{m}$. (b) The model used for HP Momentum calculation.	84
Fig. B-2. Comparison between HP Momentum simulation results and published experimental data for the structure shown in Fig. B-1.	86

Chapter 1

Introduction

1.1 Introduction

1.1.1 Why fiber optics?

The tremendous increase in the availability of inexpensive, high-speed personal computers has led to an exponential growth in internet traffic, resulting in greatly expanded demands for high-speed digital communication channels. Other applications such as the transmission of video and voice over long distances also require high bandwidth links.

Until recently, virtually all communication systems have relied on the transmission of information at radio or microwave frequencies over electrical cables or free space. The use of light for communications allows much greater transmission capacity due to its higher carrier frequency (10^{14}Hz compared with 10^{10}Hz for microwave). The burst in optical communication research started in the early 1960s with the invention of the laser¹ and the investigation of semiconductor diode lasers.^{2,3} Concurrent with this work, research on optical fibers was conducted, since they promised to provide a much more reliable and versatile optical channel than the atmosphere. In 1970, continuous-wave (CW) operation of a semiconductor laser at room temperature was realized,⁴ and fused silica fibers with a 20dB/km attenuation were developed.⁵ Later on, laser diodes operating at 0.85 , 1.3 and $1.55\mu\text{m}$ were made available, and fiber attenuation has decreased to below 0.2dB/km ($1.55\mu\text{m}$).⁶

Apart from having low transmission loss and wide bandwidth, optical fibers have several other advantages over conventional copper cables:

1. *Immunity to interference.* The dielectric nature of optical fibers means that they are immune to electromagnetic interference (EMI), such as inductive pickup from signal-carrying wires and lightning.
2. *Signal security.* Using an optical fiber ensures a high degree of data security, since the optical signal is well confined within the waveguide (with any leakage being absorbed by the opaque jacketing around the fiber).
3. *Small size and weight.* The low weight and small (hair-sized) dimensions of fibers are especially important for use in aircraft, satellites, and ships, where lightweight cables are advantageous.
4. *Abundant raw material.* Silica is the principal material in an optical fiber. This raw material is abundant and inexpensive, since it can be found in ordinary sand.

1.1.2 In-line fiber devices

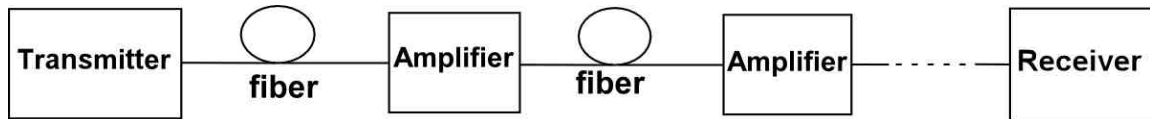


Fig. 1-1. The basic elements of a fiber-optic communication system.

Fig.1-1 shows the schematic diagram of a fiber-optic communication system. The transmitter converts an electrical signal into an optical one and sends it along the fiber. It consists of a laser source, which can either be directly modulated or externally modulated with a modulator. The modulator is useful because of the poor high-frequency performance of directly modulated laser diodes.^{7,8} The middle part of the link consists of optical fibers along with optical amplifiers which are used to counter fiber propagation losses.^{9,10} When the signal reaches its destination, it is converted back into electrical form at the receiver, of which a photodetector is an important part.

In a standard point-to-point link, an optical fiber has one source at the transmitting end. Since an optical source has a narrow spectral width, this type of transmission scheme makes use of only a very narrow portion of the fiber bandwidth. For example, the loss minimum for silica fibers at $1.55\mu\text{m}$ is about 25THz wide, while present-day optical

devices (lasers, modulators, switches and detectors) have bandwidths that are less than 100GHz. By simultaneously transmitting multiple optical signals over the same fiber, each having a different emission wavelength, a dramatic increase in the information capacity of a fiber can be achieved. The development of this technology, known as wavelength division multiplexing (WDM),^{11,12} promises to meet our insatiable demand for bandwidth and is what is responsible for the explosive growth in the fiber-optics industry since the late 1990s.

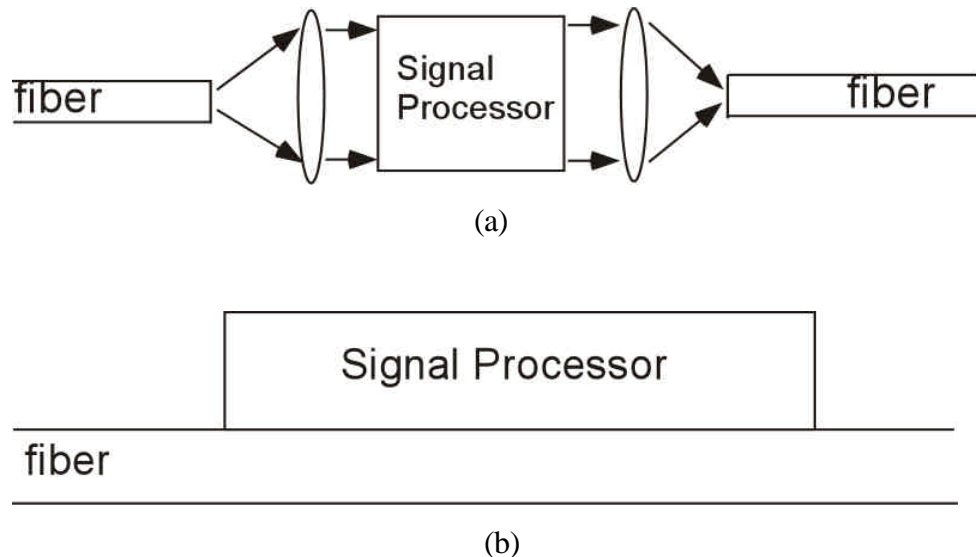


Figure 1-2. Two different approaches to coupling an optical fiber to information processing elements: (a) conventional “insertion” method, and (b) in-line fiber architecture where evanescent wave coupling occurs.

A high-performance optical communication system requires high-performance optoelectronic devices. The conventional approach to fabricating fiber-coupled devices involves the interruption of the fiber and the insertion of the device. Several drawbacks are associated with this approach, including high insertion loss, mechanical instability, and high packaging costs. In-line fiber devices, in which light is evanescently coupled between single mode fibers and multimode high index waveguides, offer solutions to these problems. Fig. 1-2 illustrates the two approaches. Materials that have been used in the implementation of in-line fiber devices include liquid crystals,¹³ electro-optic polymers¹⁴ and lithium niobate substrates.¹⁵ Gallium arsenide and other compound semiconductor devices offer significant advantages over the above materials in that they

can be monolithically integrated with lasers and high-speed electronics, thereby reducing fabrication costs. In addition, the sharp index contrast between the semiconductor and the fiber leads to wavelength-selective coupling, which can be exploited for WDM applications.

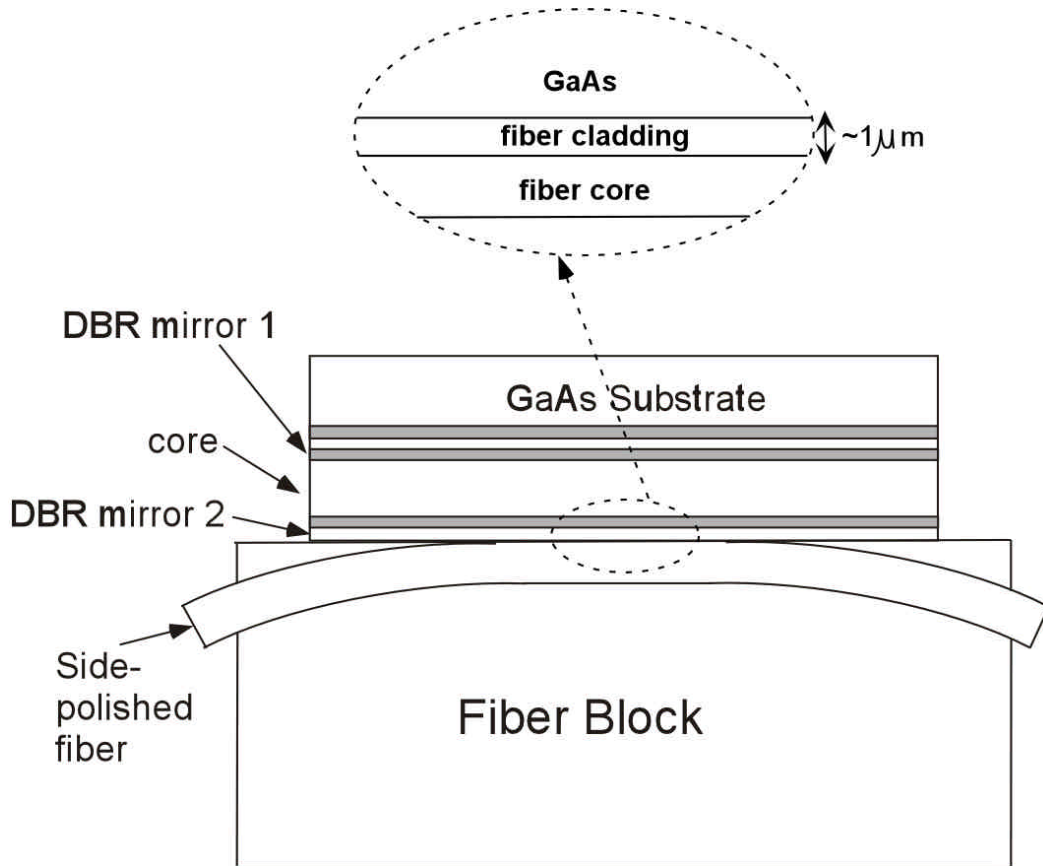


Figure 1-3. The schematic of a GaAs in-line fiber device. The fiber is side-polished so that the remaining cladding thickness is about $1\mu\text{m}$.

The goal of this thesis work is to demonstrate various compound semiconductor in-line fiber devices. The operation of these devices requires evanescent wave coupling, and hence phase-matching, between a side-polished single mode fiber and a high-index semiconductor waveguide. Compound semiconductor materials usually have refractive indices in the range of 3~3.5, while the index of glass fibers is about 1.45. Therefore this large index mismatch has to be overcome in order for phase-matching to occur between the modes of the two waveguides. This can be accomplished by the use of dielectric

mirrors in the semiconductor waveguide. The mirrors can be designed to provide high reflection for a specific mode angle, therefore the optical wave inside the semiconductor waveguide can propagate with an effective index much lower than the material index. This class of optical waveguides, where guiding is achieved by reflections from dielectric mirrors rather than total internal reflection at dielectric interfaces, is commonly referred to as anti-resonant reflecting optical waveguides (ARROW).^{16,17} By incorporating quantum well absorption/gain layers in the core of the ARROW, active devices such as modulators, detectors and light emitters can be realized in this configuration. This thesis is concerned with the design, fabrication and characterization of these devices, whose generic diagram is shown in Figure 1-3.

1.2 Organization

The organization of this thesis is as follows. Chapter 2 provides the theoretical background necessary for understanding guided wave optics. Chapter 3 discusses the modeling and design of ARROWS and in-line fiber coupled waveguide systems. Chapters 4-6 present the experimental results of a variety of in-line fiber devices. Chapter 4 focuses on passive wavelength selective devices, including narrow linewidth filters and detectors. Chapter 5 highlights the design and demonstration of multiple-quantum-well modulators based on the quantum confined Stark effect. The results from a light-emitting device are shown in Chapter 6. Finally, chapter 7 provides a brief summary of the thesis and suggests directions for future research.

Chapter 2

Theoretical background

The work described in this thesis concerns the interaction between optical waveguides and the ability to electronically change the interaction. The reader is therefore presented with a brief introduction to guided wave optics in this chapter. The emphasis is on the analysis and design of planar dielectric waveguides and optical fibers. The optical coupling between waveguides is also discussed.

2.1 Planar dielectric waveguides

Long distance free-space optical transmission is difficult to realize due to diffraction, along with obstruction and scattering by various objects in the beam path. In order to transmit light efficiently over long distances, a relatively new technology, guided wave optics, has been developed, whereby the light beam is confined in some sort of “dielectric conduit”. The basic concept of optical confinement is rather simple. A slab, strip, or cylinder of material that is embedded in a reflecting medium, which can be either a mirror or a material of lower refractive index, acts as a light “trap” in which optical rays remain confined by multiple reflections at the interfaces.

A planar dielectric waveguide is a slab of dielectric material surrounded by reflecting media. The light inside the slab, which is usually referred to as the “core”, is guided by reflection from the upper and lower media, which are called the “cladding”. A mode of a dielectric waveguide is a solution to the wave equation

$$\nabla^2 \mathbf{E}(\mathbf{r}) + k_0^2 n^2(\mathbf{r}) \mathbf{E}(\mathbf{r}) = 0 , \quad (2-1)$$

where $k_0^2 = (2\mathbf{p} / \mathbf{l})^2$, \mathbf{E} is the electric field, n is the refractive index and \mathbf{r} is the position. To determine the modes of a waveguide, a formal approach involves solving equation (2-1) with the appropriate boundary conditions (namely, the continuity of the tangential components of \mathbf{E} and \mathbf{H} at the interfaces). There is, however, a more intuitive approach to this problem — by writing the solution in terms of TEM plane waves bouncing between the surfaces of the core and imposing the self-consistency condition, the bounce angles and therefore the propagation constants can be determined.

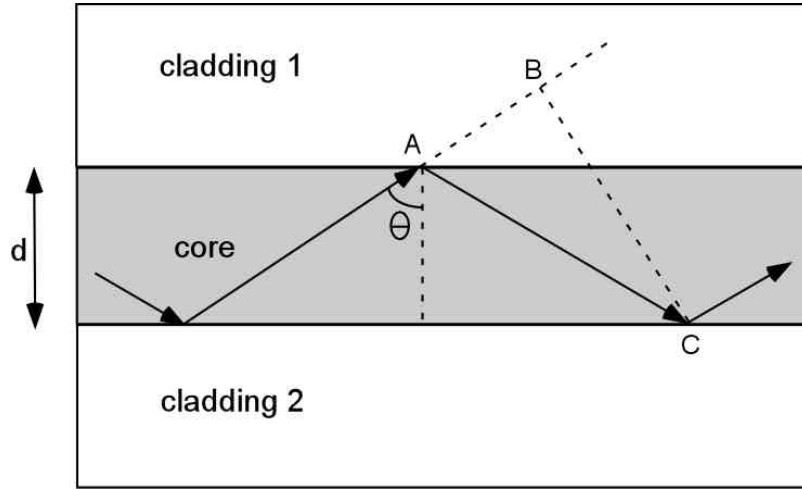


Figure 2-1. A planar dielectric waveguide. A mode is represented as a TEM plane wave bouncing between the surfaces of the core. The lines AB and BC are perpendicular to each other.

The self-consistency condition requires a wave to reproduce itself after each round trip. As shown in Fig. 2-1, the twice-reflected wave lags behind the original wave by a distance $AC - AB = d / \cos \theta - d \cos(\pi - 2\theta) / \cos \theta$, which can be simplified to yield $AC - AB = 2d \cos \theta$. At each dielectric interface, the reflection can introduce additional phase shifts, represented as ϕ_1 and ϕ_2 . For self-consistency, the net phase shift between the two waves must be zero or a multiple of 2π ,

$$\frac{2\pi}{\lambda} n_{core} 2d \cos \theta - \phi_1 - \phi_2 = 2\pi m \quad m = 0, 1, 2, \dots , \quad (2-2)$$

where ϕ_1 and ϕ_2 are in general functions of the core and cladding refractive indices, the wavelength, the field polarization as well as the incident angle θ . For a given wavelength, polarization and index profile, the transcendental equation (2-2) can be solved to yield the bounce angles of the modes, θ_m . The effective propagation index of the waveguide is then $n_{\text{eff}} = n_{\text{core}} \sin \theta_m$.

In a conventional dielectric slab waveguide, the claddings have lower refractive indices than the core. When the angle θ is greater than the critical angles θ_{c1} and θ_{c2} , where $\theta_{ci} = \sin^{-1}(n_{\text{cladding}_i} / n_{\text{core}})$, waveguiding occurs through total internal reflection of the plane wave at the interfaces. In an anti-resonant reflecting optical waveguide (ARROW), however, the core does not necessarily have to have a higher refractive index than the claddings, as long as the claddings are made of structures that efficiently reflect the plane wave coming from the core (for example, dielectric mirrors).

2.2 Transfer matrix method for analyzing multi-layer waveguides

Equation (2-2) provides an intuitive understanding of the behavior of dielectric slab waveguides. However, solving this transcendental equation can become tedious and time-consuming, and is not the method of choice for obtaining numerical solutions, especially for multi-layer (>3) or graded index waveguides. Throughout this thesis work, the approach chosen for waveguide analysis and design is the so-called transfer matrix method. This method, which is commonly used in studying thin film optical filters,¹⁸ is a simple and efficient approach that can be applied to arbitrary multi-layer optical waveguide structures.¹⁹

In essence, the transfer matrix method involves the multiplication of 2x2 matrices from which one can obtain the transmission resonances, and hence the propagation constants as well as the field configurations for a multi-layer waveguide structure. In the structure shown in Fig. 2-2, the electric field at each layer can be expressed in the form

$$\mathbf{E}_i = \hat{\mathbf{e}}^+ E_i^+ \exp[j(-k_i \cos \theta_i x - k_i \sin \theta_i z)] + \hat{\mathbf{e}}^- E_i^- \exp[j(k_i \cos \theta_i x - k_i \sin \theta_i z)], \quad (2-3)$$

where $\hat{\mathbf{e}}^+$ and $\hat{\mathbf{e}}^-$ represent the unit vectors along which the electric fields point, E_i^+ and E_i^- are the complex electric field amplitudes at the interface between layers i and $i+1$, and $k_i = 2\pi n_i / \lambda$.

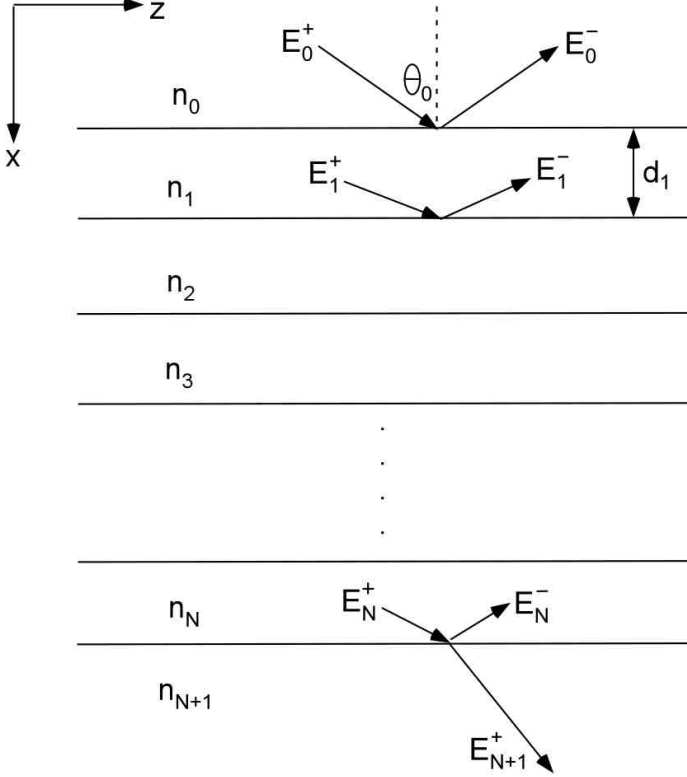


Figure 2-2. The incidence of a plane wave at an angle θ_0 onto a layered structure.

In the TE case, the electric fields point along the y-direction, therefore $\hat{\mathbf{e}}^+ = \hat{\mathbf{e}}^- = \hat{\mathbf{y}}$. The continuity of E_y and H_z at the interface between layers $i-1$ and i requires

$$E_{i-1}^+ + E_{i-1}^- = E_i^+ \exp(j\delta_i) + E_i^- \exp(-j\delta_i) \quad (2-4)$$

and

$$k_{i-1} \cos \theta_{i-1} E_{i-1}^+ - k_{i-1} \cos \theta_{i-1} E_{i-1}^- = k_i \cos \theta_i E_i^+ \exp(j\delta_i) - k_i \cos \theta_i E_i^- \exp(-j\delta_i), \quad (2-5)$$

where $\mathbf{d}_i = k_i \cos \theta_i \mathbf{d}_i$. Equations (2-4) and (2-5) can be combined to obtain

$$\begin{pmatrix} E_{i-1}^+ \\ E_{i-1}^- \end{pmatrix} = \frac{1}{t_i} \begin{pmatrix} \exp(j\delta_i) & r_i \exp(-j\delta_i) \\ r_i \exp(j\delta_i) & \exp(-j\delta_i) \end{pmatrix} \begin{pmatrix} E_i^+ \\ E_i^- \end{pmatrix} = S_i \begin{pmatrix} E_i^+ \\ E_i^- \end{pmatrix}, \quad (2-6)$$

where t_i and r_i are the field amplitude transmission and reflection coefficients respectively. They can be expressed as

$$\begin{aligned} t_i &= \frac{2n_{i-1} \cos \theta_{i-1}}{n_{i-1} \cos \theta_{i-1} + n_i \cos \theta_i} \\ r_i &= \frac{n_{i-1} \cos \theta_{i-1} - n_i \cos \theta_i}{n_{i-1} \cos \theta_{i-1} + n_i \cos \theta_i}. \end{aligned} \quad (2-7)$$

In the TM case (H-field pointing along the y-direction), it can be shown that equation (2-6) is also valid provided

$$\begin{aligned} t_i &= \frac{2n_{i-1} \cos \theta_{i-1}}{n_i \cos \theta_{i-1} + n_{i-1} \cos \theta_i} \\ r_i &= \frac{n_i \cos \theta_{i-1} - n_{i-1} \cos \theta_i}{n_i \cos \theta_{i-1} + n_{i-1} \cos \theta_i}. \end{aligned} \quad (2-8)$$

In both cases, t_i and r_i are the Fresnel transmission and reflection coefficients at the interface between layers i-1 and i. If equation (2-6) is applied at each interface, we obtain

$$\begin{pmatrix} E_0^+ \\ E_0^- \end{pmatrix} = S_1 S_2 \cdots S_N \begin{pmatrix} E_N^+ \\ E_N^- \end{pmatrix} = \begin{pmatrix} m_{11} & m_{12} \\ m_{21} & m_{22} \end{pmatrix} \begin{pmatrix} E_N^+ \\ E_N^- \end{pmatrix}. \quad (2-9)$$

To arrive at an expression relating the input field (E_0) to the output field (E_{N+1}), we need to find the relationship between E_N and E_{N+1} , which is straightforward due to the lack of a backward traveling wave in layer N+1 ($E_{N+1}^- = 0$),

$$\begin{aligned} E_{N+1}^+ &= E_N^+ t_{N+1} \\ E_N^- &= E_N^+ r_{N+1} \end{aligned} \quad (2-10)$$

Combining equations (2-9) and (2-10), the transmission coefficient of the multi-layer stack can be expressed as

$$t = \frac{E_{N+1}^+}{E_0^+} = \frac{t_{N+1}}{m_{11} + m_{12} r_{N+1}}. \quad (2-11)$$

In order to use the transfer matrix method to calculate the propagation characteristics of planar waveguides, layers 1 to N (in Fig. 2-2) may correspond to the actual waveguide structure (claddings and core), while layers 0 and N+1 are high index input and output layers added for the ease of computation. The transmission of the structure ($|E_{N+1}^+ / E_0^+|$) can be calculated as a function of the input angle θ_0 , and the values

of θ_0 at which the resonance peaks appear are related to the real part of the propagation constants by the simple expression $\beta = k_0 \sin \theta_0$. Once the propagation constant of a particular mode is determined, the relative field strength at each interface can be calculated using equation (2-6) and the mode shape is obtained.

2. 3 Optical fibers

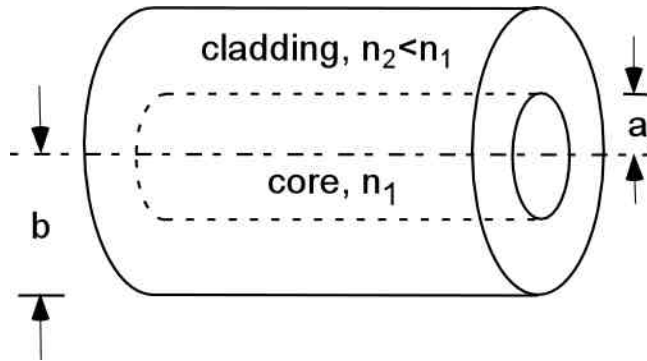


Fig. 2-3. Schematic of a step index optical fiber.

An optical fiber is a cylindrical waveguide made of low-loss materials, such as silica glass. The core in which the light is guided is embedded in a cladding of slightly lower refractive index (Fig. 2-3). As in the case of a conventional slab waveguide, light rays incident at angles greater than the critical angle at the core-cladding interface undergo total internal reflection and are guided inside the core.

The propagation characteristics of an optical fiber are determined by solving the wave equation (2-1). The cladding radius (b) is usually much larger than the core radius (a) such that it can be safely assumed to be infinite when examining the guided waves in the core and near the core-cladding boundary. Since the refractive index profile $n(r)$ of a fiber is cylindrically symmetric, it is convenient to use the cylindrical coordinate system, where the field components are $E_r, E_\phi, E_z, H_r, H_\phi$ and H_z . Because the unit vectors \hat{r} and $\hat{\phi}$ are not constant vectors in a Cartesian coordinate system, only for the z component of the field vectors does the wave equation retain its simple form,

$$\nabla^2 U + n^2 k_0^2 U = 0, \quad (2-12)$$

where $U(r,\phi,z)$ represents E_z or H_z in cylindrical coordinates, and ∇^2 is the Laplacian operator given by

$$\nabla^2 = \frac{\partial^2}{\partial r^2} + \frac{1}{r} \frac{\partial}{\partial r} + \frac{1}{r^2} \frac{\partial^2}{\partial \phi^2} + \frac{\partial^2}{\partial z^2}. \quad (2-13)$$

For a wave traveling in the z -direction with a propagation constant β , the z -dependence of U takes the form $e^{-j\beta z}$. Because U must be a periodic function of the angle ϕ with a period of 2π , its ϕ -dependence can be expressed as $e^{-jl\phi}$, where l is an integer. Substituting

$$U(r,\phi,z) = u(r)e^{-jl\phi}e^{-j\beta z}, \quad l = 0, \pm 1, \pm 2, \dots \quad (2-14)$$

into (2-12), an ordinary differential equation for $u(r)$ is obtained,

$$\frac{d^2u}{dr^2} + \frac{1}{r} \frac{du}{dr} + (n_1^2 k_0^2 - \beta^2 - \frac{l^2}{r^2})u = 0. \quad (2-15)$$

By requiring the solution be bounded (i.e., $n_2 k_0 < \beta < n_1 k_0$), the solutions to (2-18) are given by

$$u(r) = \begin{cases} AJ_l(k_t r), & r < a \text{ (core)} \\ BK_l(\gamma r), & r > a \text{ (cladding)} \end{cases}, \quad (2-16)$$

where $k_t^2 = n_1^2 k_0^2 - \beta^2$, $\gamma^2 = \beta^2 - n_2^2 k_0^2$, A and B are constants, J_l is the Bessel function of the first kind and order l , K_l is the modified Bessel function of the second kind and order l . The z -component of the field is continuous at $r = a$, therefore

$$A = BK_l(\gamma a)/J_l(k_t a). \quad (2-17)$$

The remaining field components E_r, H_r, E_ϕ and H_ϕ are determined in terms of E_z and H_z with the help of Maxwell's equations $j\omega\epsilon_0 n^2 \mathbf{E} = \nabla \times \mathbf{H}$, and $-j\omega\mu_0 \mathbf{H} = \nabla \times \mathbf{E}$. By matching the boundary conditions at $r = a$ (i.e., the continuity of E_z, H_z, E_ϕ and H_ϕ), a characteristic equation relating the propagation constant β to the known parameters n_1, n_2, a and λ is found.

In practice, most fibers are weakly guiding (i.e., $n_1 \approx n_2$) so that the guided rays are almost parallel to the fiber axis. As a result, the longitudinal components of the electric and magnetic fields are much smaller than the transverse ones and the guided

waves are essentially transverse electromagnetic (TEM). The linearly polarized modes in the x- and y-directions then form the orthogonal states of polarization. In this case, the wave equation (2-12) can be applied to the Cartesian field components E_x, E_y, H_x and H_y , which are much larger than the z-components. And the general solution is given by (2-16). Since E_ϕ can be expressed as

$$E_\phi = -E_x \sin \phi + E_y \cos \phi, \quad (2-18)$$

it becomes simply proportional to either E_x or E_y if one of the components vanishes. Therefore the continuity of E_ϕ is equivalent to the continuity of E_x or E_y , and the boundary condition (2-17) is still valid.

In the limit of $n_1 \approx n_2$, k_t and γ are both much smaller than β . Taking into account this approximation and after some laborious algebra,²⁰ the characteristic equation can be written as

$$k_t \frac{J_{l\pm 1}(k_t a)}{J_l(k_t a)} = \pm \gamma \frac{K_{l\pm 1}(\gamma a)}{K_l(\gamma a)}. \quad (2-19)$$

The two equations above (with + and – signs) are mathematically equivalent given the following properties of Bessel functions

$$\begin{aligned} \frac{l}{x} J_l(x) &= \frac{1}{2} [J_{l-1}(x) + J_{l+1}(x)] \\ \frac{l}{x} K_l(x) &= -\frac{1}{2} [K_{l-1}(x) - K_{l+1}(x)] \end{aligned} . \quad (2-20)$$

Equation (2-19) may be solved graphically by plotting the its left- and right-hand sides as functions of $k_t a$, given the constraint

$$(k_t a)^2 + (\gamma a)^2 = \left(\frac{2\pi a}{\lambda}\right)^2 (n_1^2 - n_2^2) = V^2. \quad (2-21)$$

For each azimuthal index l , the characteristic equation yields multiple solutions of the propagation constant β_{lm} , $m = 1, 2, 3, \dots$, each representing a mode. Fig. 2-4 shows an example of the graphical solution of the characteristic equation (2-19) with $l=0$ and $V=5$.

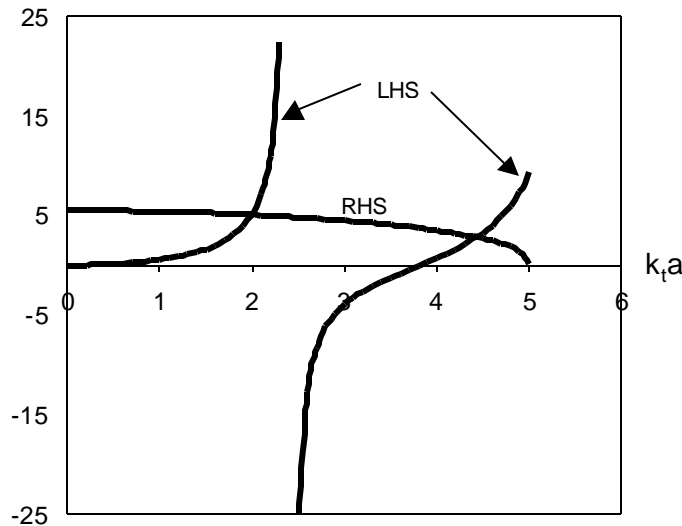


Fig. 2-4. Illustration of the graphical approach to solving the characteristic equation (2-19). The left-hand and right-hand sides are plotted as functions of $k_t a$. The intersections are the solutions.

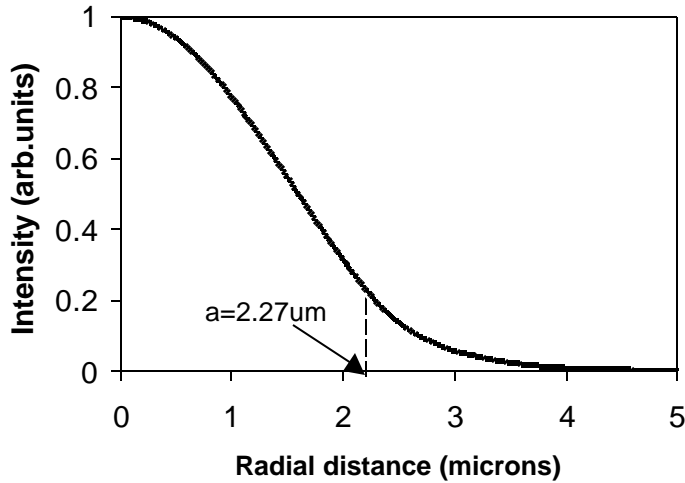


Fig. 2-5. The field intensity distribution of a typical single mode fiber operating at 830nm. The parameters are $n_1=1.4583358$, $n_2=1.45253$ and $a=2.27\mu m$.

It is evident from Fig. 2-4 that the number of guided modes is equal to the number of roots of $J_{l\pm 1}(k_t a)=0$ that are smaller than V . Considering the minus sign in the characteristic equation, the smallest root of $J_{l-1}(k_t a)=0$ is 0 (when $l=0$) and the next

smallest is 2.405 (when $l = 1$). Thus for $V < 2.405$, the fiber becomes a single mode waveguide. Physically, single mode operation can be achieved by using a small core diameter, a small numerical aperture (making $n_1 - n_2$ small), or a longer wavelength. The mode of a single mode fiber has a bell shaped distribution (Fig. 2-5) and provides the highest confinement of light power within the core. In a multimode fiber, modal dispersion (different modes travel at different group velocity) causes pulse spreading and limits the transmission bit rate. Therefore it is advantageous to use single mode fibers in an optical communication system.

2.4 Evanescent wave coupling

When two waveguides are sufficiently close to each other such that their fields overlap, light can be coupled from one guide to the other and optical power transfer occurs. This can be regarded as a scattering effect. The presence of waveguide 1 scatters the field outside waveguide 2, thus creating a source of optical radiation which modifies the field amplitude in waveguide 2. Conversely, waveguide 2 has the same effect on waveguide 1. This phenomenon is known as evanescent wave coupling, which is the basis for making waveguide couplers and switches, as well as the various devices described in this dissertation.

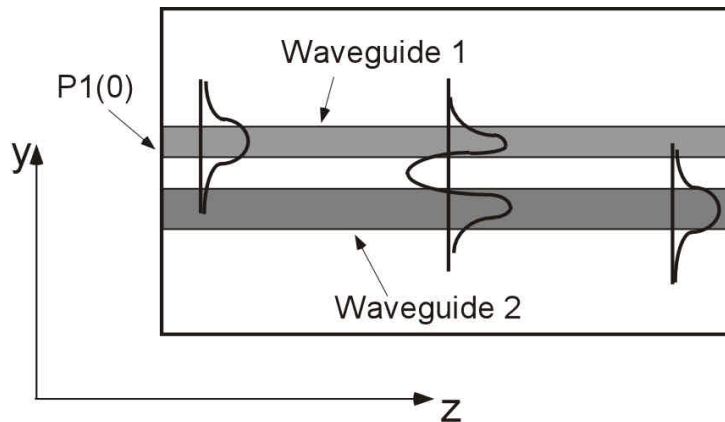


Fig. 2-6. Coupling between two waveguides. The optical field in waveguide 1 overlaps slightly with the core of waveguide 2, which induces gradual power transfer. On the left, light is mostly in waveguide 1, while on the right, it is mostly in waveguide 2.

The formal approach to investigating the propagation of light in a coupled-waveguide structure involves solving Maxwell's equations with the appropriate boundary conditions for the overall system. An exact analysis is difficult and is usually carried out with complex numerical routines.^{21,22,23} However, in the case of weak coupling, where the optical field amplitudes vary only slowly over the distance of one wavelength (always true for practical devices), a simple approximate theory, known as coupled-mode theory, usually suffices.

The coupled-mode theory assumes that the mode shape of each waveguide remains approximately the same in the absence of the other, and that coupling affects the amplitude of these modes without modifying their transverse field distribution and propagation constants. Using the coordinate system shown in Fig. 2-6, when the two waveguides are not interacting, the complex field amplitudes can be written as

$$E_1(y, z) = a_1 u_1(y) \exp(-j\beta_1 z) \quad . \quad (2-22)$$

$$E_2(y, z) = a_2 u_2(y) \exp(-j\beta_2 z)$$

The amplitudes a_1 and a_2 are constant. Under the premises of the coupled-mode theory, when coupling occurs, a_1 and a_2 become functions of z but the transverse field distribution $u_1(y)$ and $u_2(y)$, and the propagation constants β_1 and β_2 remain unchanged.

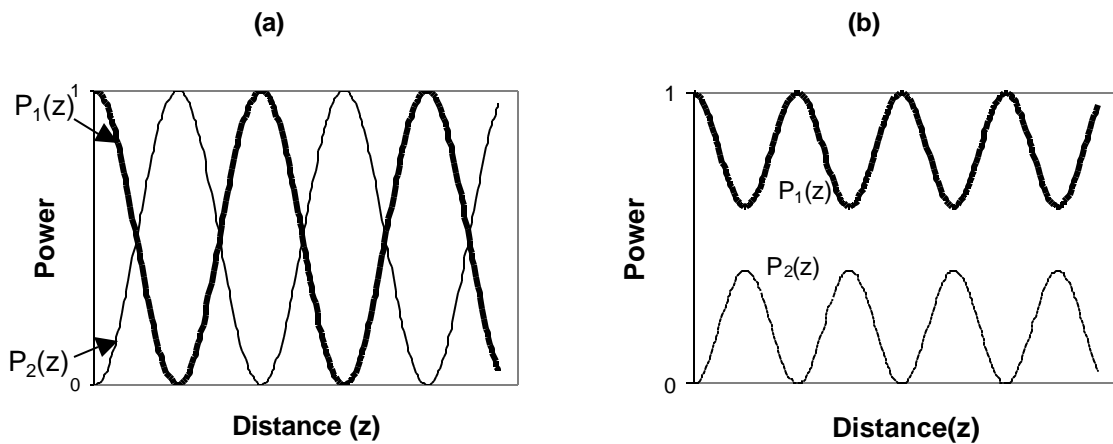


Fig. 2-7. Exchange of power between two waveguides: (a) when the two guides are phase-matched; (b) when the two guides are not phase-matched.

In the case where both waveguides are lossless, it can be shown²⁴ that the amplitudes a_1 and a_2 are related by two coupled first-order differential equations

$$\begin{aligned}\frac{da_1}{dz} &= -jC \exp(j\Delta\beta z) a_2(z) \\ \frac{da_2}{dz} &= -jC \exp(-j\Delta\beta z) a_1(z)\end{aligned}, \quad (2-23)$$

where $\Delta\beta = \beta_1 - \beta_2$, and C is the coupling coefficient which is proportional to the field overlap between the waveguides.

Assuming that at $z=0$, light is completely confined in waveguide 1 (i.e., $a_1(0)=1$ and $a_2(0)=0$), then (2-23) can be solved to yield

$$\begin{aligned}a_1(z) &= \exp\left(\frac{j\Delta\beta z}{2}\right) \left(\cos \gamma z - j \frac{\Delta\beta}{2\gamma} \sin \gamma z\right) \\ a_2(z) &= \frac{C}{j\gamma} \exp\left(-\frac{j\Delta\beta z}{2}\right) \sin \gamma z\end{aligned}, \quad (2-24)$$

where

$$\gamma^2 = \left(\frac{\Delta\beta}{2}\right)^2 + C^2. \quad (2-25)$$

The optical powers are therefore

$$P_1(z) \propto |a_1(z)|^2 = \left[\cos^2(\gamma z) + \left(\frac{\Delta\beta}{2\gamma}\right)^2 \sin^2(\gamma z)\right]. \quad (2-26)$$

$$P_2(z) \propto |a_2(z)|^2 = \frac{|C|^2}{\gamma^2} \sin^2(\gamma z)$$

In the case of phasematching (i.e., $\Delta\beta = 0$), (2-26) becomes

$$\begin{aligned}P_1(z) &= \cos^2(Cz) \\ P_2(z) &= \sin^2(Cz)\end{aligned}. \quad (2-27)$$

The periodic power exchange between the waveguides is illustrated in Fig. 2-7. When $\Delta\beta = 0$, the exchange of power is complete within a distance of $z = L_0 = \pi/2C$, which is called the transfer length or coupling length.

Chapter 3

ARROW and coupled waveguide simulation

This chapter describes the analytical and numerical modeling of anti-resonant reflective optical waveguides (ARROW), which form the basis of this thesis work. In addition, a simplified version of the coupled mode theory as applied to coupled ARROW-fiber waveguide systems is discussed.

3.1 GaAs/AlGaAs material system

In this work, all our ARROWS are based on the GaAs/AlGaAs material system. Gallium arsenide is the second most commonly used semiconductor after silicon. In terms of integrated circuit applications, GaAs is not as popular as Si due to processing problems such as the lack of a stable native oxide. However, this material does possess certain unique advantages. A higher electronic mobility than Si makes it attractive for high speed electronics, and a direct bandgap leads to efficient light generation and absorption.

In one of its rare cases of cooperation, nature has gifted us with the ability to make heterostructures on GaAs using $\text{Al}_x\text{Ga}_{1-x}\text{As}$ alloys. Since the lattice constant of AlAs is very close to that of GaAs, high quality materials can be produced. The bandgap of the AlGaAs alloy increases with Al concentration. At room temperature, the band gap of the alloy is given by Adachi²⁵

$$E_g(\text{Al}_x\text{Ga}_{1-x}\text{As}) = 1.424 + 1.247x \text{ (eV)}, \quad x < 0.45 \quad (3-1)$$

$$E_g(\text{Al}_x\text{Ga}_{1-x}\text{As}) = 1.900 + 0.125x + 0.143x^2 \text{ (eV)}. \quad x > 0.45 \quad (3-2)$$

The split is due to the fact that the bandgap becomes indirect when the Al composition of the alloy is higher than 45%. In the direct gap regime, it is commonly accepted that the band offset for materials with different Al compositions is split between the conduction

band and the valence band in a 65% to 35% ratio. One other physical property that is relevant to this work is the complex index of refraction. Like other material parameters, it is also a function of the Al composition, which makes possible the fabrication of multi-layer optical structures. The formulae for calculating the refractive index are given by Adachi²⁵ and will not be quoted here. At energies close to the GaAs bandgap, which, as shown later, are the energies of interest to this work due to large electro-optic effects, the real part of the refractive index varies from about 3 in AlAs to about 3.5 in GaAs in a more or less linear fashion.

3.2 Anti-resonant reflective optical waveguides

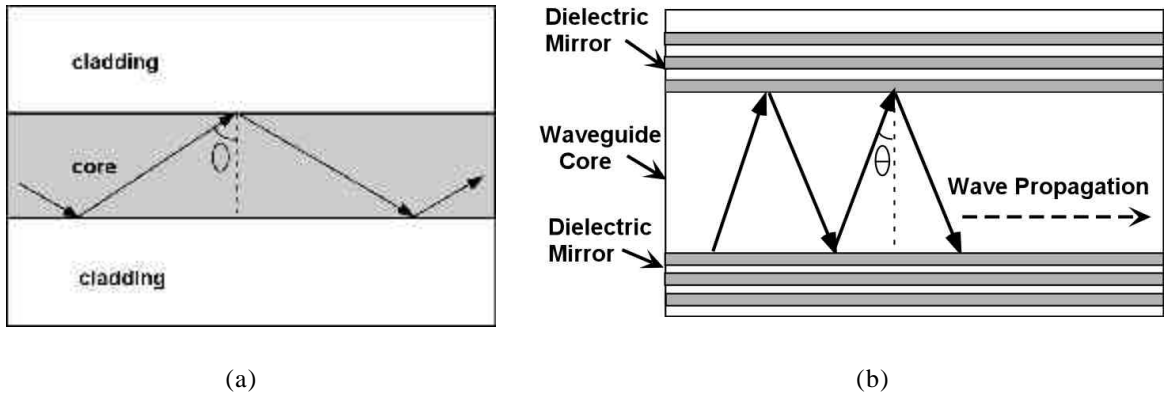


Fig. 3-1. An illustration of a conventional dielectric slab waveguide (a) and an ARROW (b). In (a), the mode angle θ has to be larger than the critical angle ($\sin^{-1}(n_{\text{cladding}}/n_{\text{core}})$) for a guided mode, while in (b), θ can be independent of the core and mirror indices.

In its conventional form, a planar dielectric waveguide consists of a high index core layer sandwiched between two low index cladding layers. With such a configuration, waveguiding is obtained through total internal reflection, therefore the effective propagation index for a guided mode is always larger than the largest cladding index and smaller than the core index. The refractive index of AlAs, which is the material with the lowest index within the GaAs/AlGaAs material system used in this work, is about 3 (at 850nm). This means that for a conventional GaAs/AlGaAs waveguide with AlAs claddings, the effective propagation index of a guided mode cannot be smaller than 3. On the other hand, the propagation index for typical glass fibers is about 1.45. Therefore, a

different waveguide design is needed in order to match the propagation indices of an AlGaAs waveguide and a single mode fiber. One way to achieve this is to use an ARROW structure, where the core layer is surrounded on one or both sides by dielectric mirrors. A dielectric mirror can be designed to provide high reflection at specific shallow angles, so the propagation index of an ARROW is not limited by the material indices of the mirror layers. For example, to phase-match an ARROW with GaAs core to a single mode fiber, the mode angle (θ in Fig. 3-1b) needs to be about 24.5 degrees ($\theta = \sin^{-1}(n_{fiber}/n_{GaAs})$).

3.2.1 Distributed Bragg reflector mirrors

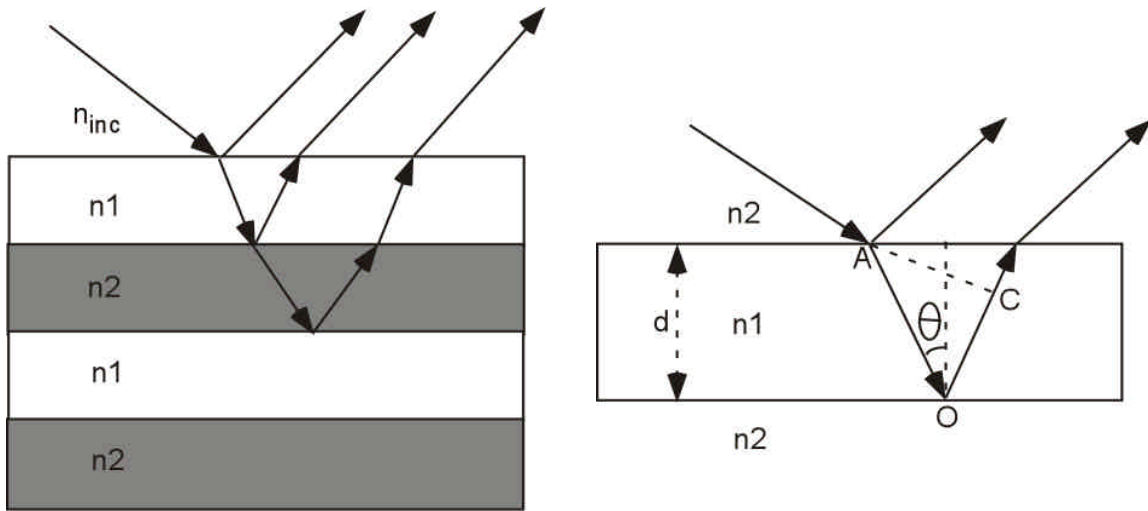


Fig 3-2. Schematic of a DBR mirror. The drawing on the right illustrates the incident and reflected rays for a constituent layer in a DBR structure.

In the GaAs/AlGaAs material system, a dielectric mirror usually consists of a stack of layers with alternating Al contents (and therefore, refractive indices). A schematic diagram of such a mirror, called a distributed Bragg reflector (DBR), is shown in Fig. 3-2. Despite the fact that the reflection from each interface may be small, when added up in phase, the aggregate reflectivity can approach unity. The phase condition is satisfied if the accumulated phase difference between two successive reflections is a

multiple of 2π . Since a phase-shift of π occurs on reflection at one of the two interfaces (according to equations 2-7 and 2-8), the phase contributed by the path length difference should be an odd multiple of π . This condition is expressed as (in terms of the symbols used in Fig. 3-2)

$$\frac{2\pi(AO+OC)n_1}{\lambda} = (2m+1)\pi , \quad (3-3)$$

which can be rearranged to yield

$$d_1 = \frac{\lambda}{4n_1 \cos \theta} . \quad (3-4)$$

In the special case of normal incidence, $\theta = 0$ so $d = \lambda/4n_1$, which is why a DBR is also commonly referred to as a quarter-wave stack.

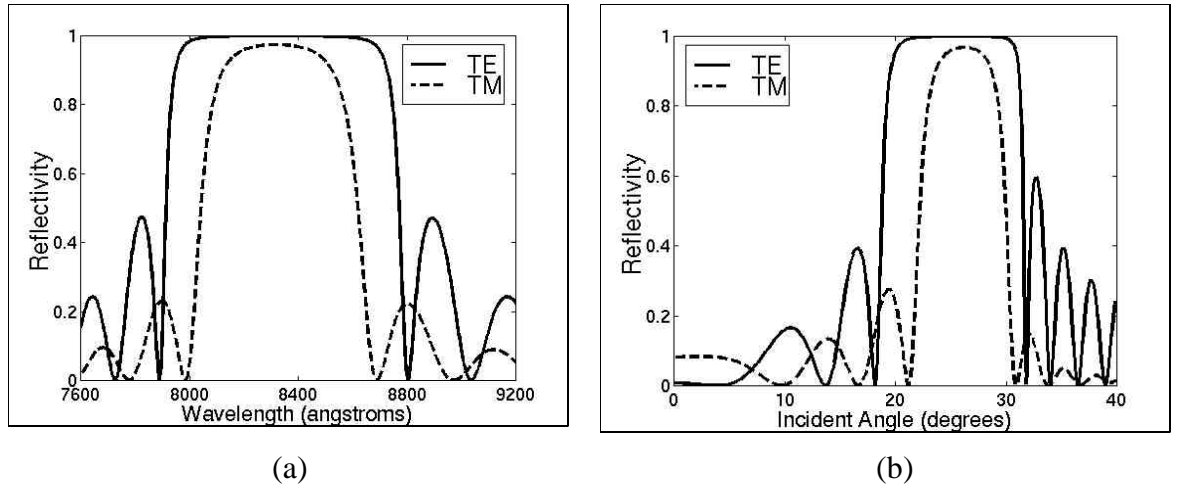


Fig 3-3. The calculated reflectivity for a DBR with 25 pairs of AlAs/Al_{0.33}Ga_{0.67}As (791 Å/671 Å). The incident medium is Al_{0.33}Ga_{0.67}As. (a) Reflectivity as a function of wavelength for a 25° incident angle; (b) Reflectivity as a function of angle at 8300 Å. TE (TM) polarization means that the incident electric (magnetic) field component lies in the plane of the layers.

The transfer matrix method introduced in the chapter 2 can be used to calculate accurately the reflection of a DBR mirror. Rearranging equations (2-9) and (2-10), the reflectivity of a dielectric multilayer is expressed as

$$R = \left| \frac{E_0^-}{E_0^+} \right|^2 = \left| \frac{m_{21} + m_{22}r_{N+1}}{m_{11} + m_{12}r_{N+1}} \right|^2 . \quad (3-5)$$

Fig. 3-3 shows the calculated reflectivity of an AlAs/AlGaAs DBR mirror optimized for 830nm and an incident angle of 25°. The reflectivity remains very close to unity within a certain wavelength and angle range. As the wavelength and the angle changes, the layer thicknesses deviate more and more from the resonant condition (3-4), the reflectivity starts to decrease sharply. The difference between the TE and TM polarizations is due to the different Fresnel reflection coefficients (equations 2-7 and 2-8) at each interface.

3.2.2 ARROW design example

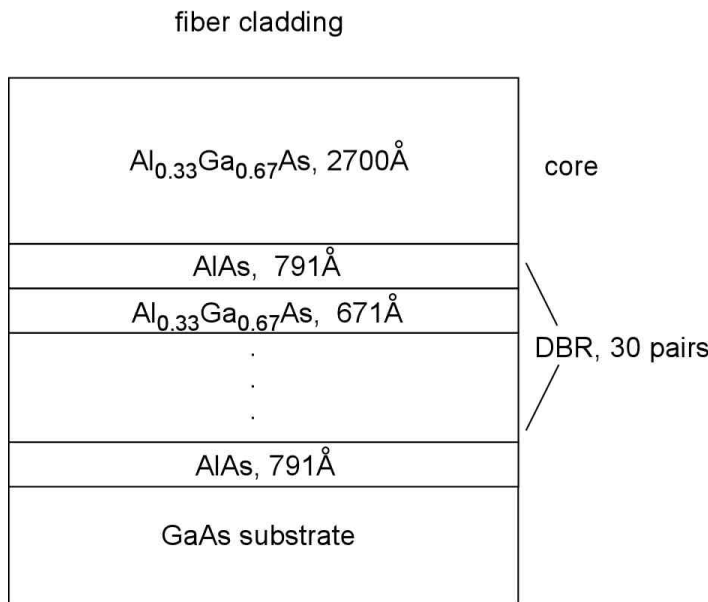


Fig. 3-4. Structure of a GaAs/AlGaAs ARROW designed to phase-match to a single mode fiber at 830nm.

In this section, the design procedure of a GaAs/AlGaAs ARROW is illustrated. First, the phase-matched wavelength is chosen, which, in this particular example, is 830nm. Then, the material composition of each layer is decided. One of the considerations here is that the DBR needs to be lossless, which then limits the mirror materials to those that are transparent at the resonant wavelength. Knowing the component materials, the resonant wavelength, and the fiber propagation index, the structure of the DBR mirror can be determined (Fig. 3-4). The core thickness is then chosen such that the transmission peak of the structure occurs at an index value that is matched to the effective index of the fiber mode (Fig. 3-5). Once the ARROW structure

is determined, the dispersion curve can be obtained by calculating the resonant angle (or index) at different wavelengths (Fig. 3-6).

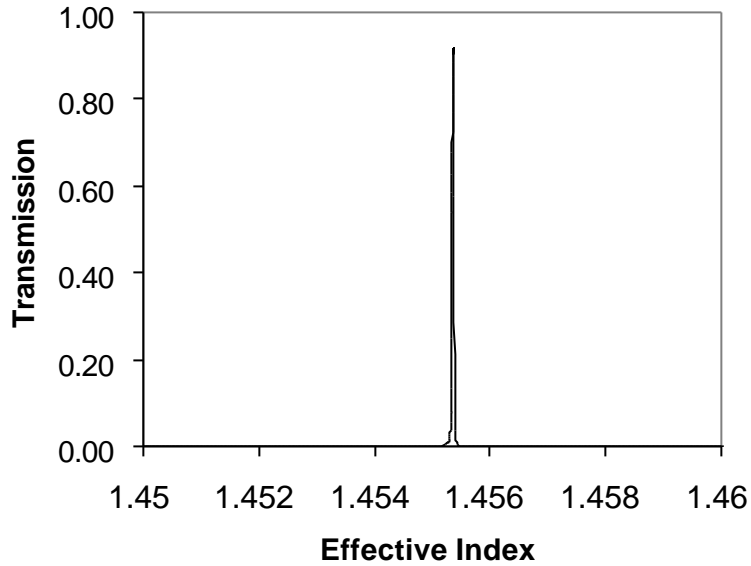


Fig. 3-5. The calculated TE optical transmission of the ARROW structure as a function of the propagation index (at 830nm). The peak corresponds to an effective index value of 1.4553, which is the same as the fiber propagation index.

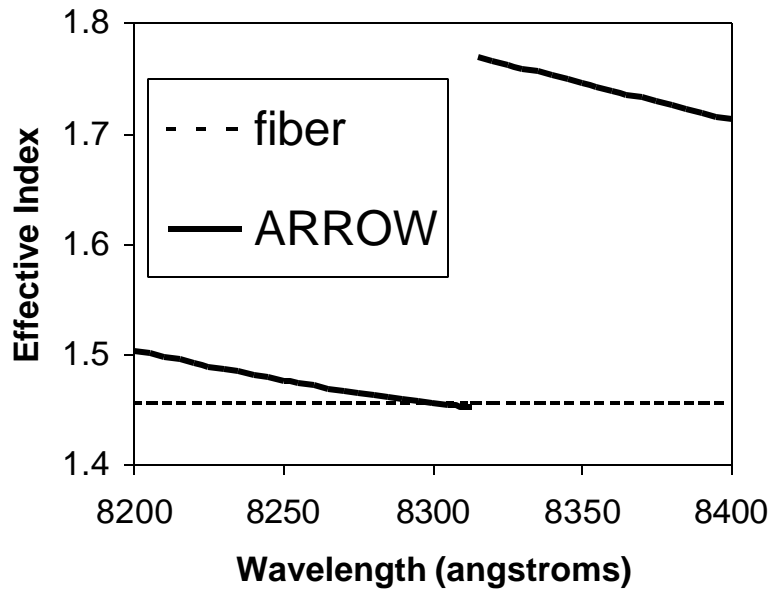


Fig. 3-6. The calculated dispersion curves for the fiber mode and the highest order confined ARROW mode (TE).

The transmission calculation can be performed either by keeping the existing ARROW structure, or by dividing the structure up into thin layers (10Å, for example). The former is faster because of the smaller number of layers. But the latter is useful when one needs to calculate the field distribution inside the waveguide. In this case, a transfer matrix is associated with each thin layer, and the total field amplitude at the interface between two layers is calculated by summing the forward- and backward-traveling wave amplitudes (section 2.2). If the layers are thin enough, a good representation of the modal field shape can be obtained (Fig. 3-7).

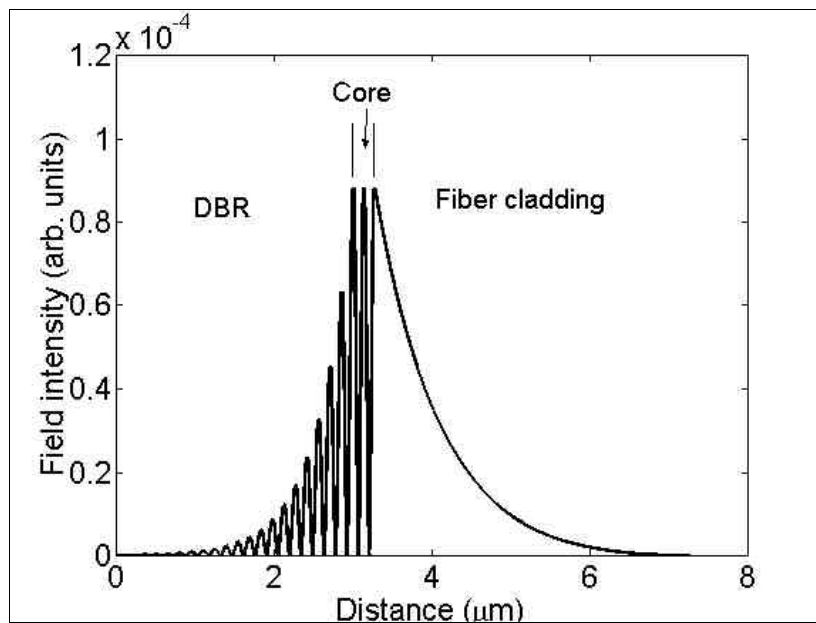


Fig. 3-7. The calculated field profile for the highest order confined mode in the ARROW (TE). The wavelength is 830nm.

3.3 Coupled-mode analysis of ARROW-fiber systems

There exist detailed analytical models which describe the coupling between a single-mode fiber and a simple slab waveguide.^{26,27,28} The case of coupling between a fiber and a semiconductor ARROW, however, is much more complex because of the presence of DBR mirrors. To gain physical insight into a coupled fiber-ARROW system, a phenomenological model based on the coupled-mode theory described in chapter 2 is used. The differential equations for the model are

$$\frac{\partial}{\partial z} A_f(z) = -jC \exp[j\Delta\beta z] A_s(z) \quad (3-6a)$$

$$\frac{\partial}{\partial z} A_s(z) = -jC \exp[-j\Delta\beta z] A_f(z) - \alpha_s A_s(z), \quad (3-6b)$$

where A_f is the complex field amplitude in the fiber, A_s is the field amplitude in the semiconductor ARROW, z is the propagation direction, $\Delta\beta = \beta_f - \beta_s$ is the difference between the propagation constants, C is the coupling coefficient, and α_s is the amplitude loss coefficient in the ARROW. The loss is a phenomenological term which includes mirror leakage, absorption and scattering losses, as well as lateral diffraction in the ARROW which prevents light from coupling back into the fiber.

3.3.1 Propagation losses in an ARROW

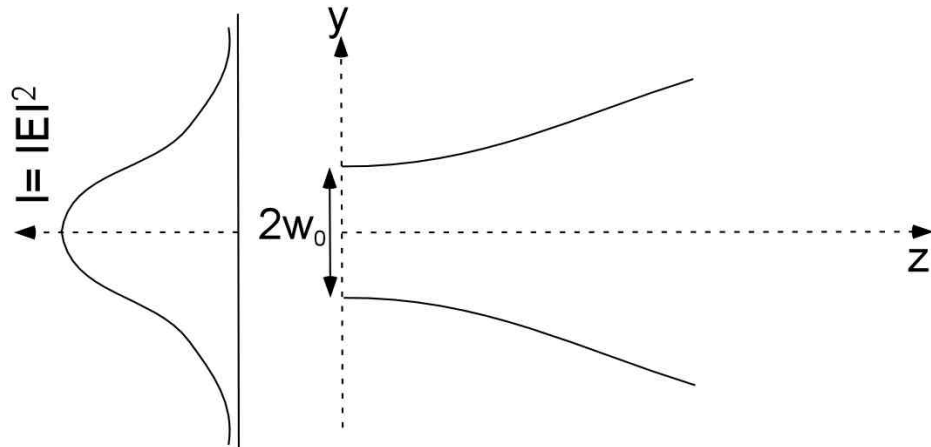


Fig. 3-8. A propagating Gaussian beam.

The lateral diffraction can be modeled as the propagation of a Gaussian beam in the plane of the ARROW core. The expression for the field intensity in a one-dimensional Gaussian beam propagating in the z -direction (Fig. 3-8) is⁷

$$I(y, z) = \frac{I_0 w_0^2}{w^2(z)} \exp\left[\frac{-2y^2}{w^2(z)}\right], \quad (3-7)$$

where I_0 is a constant, w_0 is the minimum spot size, and $w(z)$ is the spot size at position z . The spot size is defined as the lateral distance y at which the field amplitude is down

by a factor 1/e compared with the peak value. The beam expands laterally as it propagates according to the formula

$$w^2(z) = w_0^2 \left(1 + \frac{z^2}{z_0^2}\right) \quad (3-8)$$

$$z_0^2 = \frac{\pi w_0^2 n}{\lambda},$$

where n is the medium refractive index and λ is the free space wavelength.

At $z=0$, the amount of optical power confined within the beam waist is

$$P(z=0) = I_0^2 \int_{-w_0}^{w_0} \exp\left(-\frac{2y^2}{w_0^2}\right) dy, \quad (3-9)$$

which can be simplified into the form

$$P(z=0) = I_0^2 \sqrt{\frac{w_0^2 \pi}{2}} \operatorname{erf}(\sqrt{2}), \quad (3-10)$$

where $\operatorname{erf}(x)$ is the error function. At a distance z from the origin, the amount of optical power within the minimum beam waist decays to

$$P(z) = \frac{I_0^2}{1 + \frac{z^2}{z_0^2}} \int_{-w_0}^{w_0} \exp\left[-\frac{2y^2}{w^2(z)}\right] dy, \quad (3-11)$$

which, in terms of the error function, becomes

$$P(z) = \sqrt{\frac{w_0^2 \pi}{2}} \frac{I_0^2}{\sqrt{1 + \frac{z^2}{z_0^2}}} \operatorname{erf}\left(\sqrt{\frac{2}{1 + \frac{z^2}{z_0^2}}}\right). \quad (3-12)$$

The diffraction loss can be defined as the decrease in optical power within the minimum beam waist, and a fitted parameter α_{diff} is used to describe it

$$\frac{P(z)}{P(0)} = \frac{1}{\sqrt{1 + \frac{z^2}{z_0^2}}} \frac{\operatorname{erf}\left(\sqrt{\frac{2}{1 + \frac{z^2}{z_0^2}}}\right)}{\operatorname{erf}(\sqrt{2})} \approx \exp(-2\alpha_{\text{diff}} z). \quad (3-13)$$

Fig. 3-9 shows an example of graphically extrapolating the diffraction loss coefficient. The ARROW device parameters are typical: $n = 3.5$ (GaAs), $\lambda = 0.83\mu\text{m}$ and $w_0 = 2.5\mu\text{m}$ (which is approximately the radius of a single mode fiber at 830nm). The value of α_{diff} which gives the best fit is $0.0035 \mu\text{m}^{-1}$.

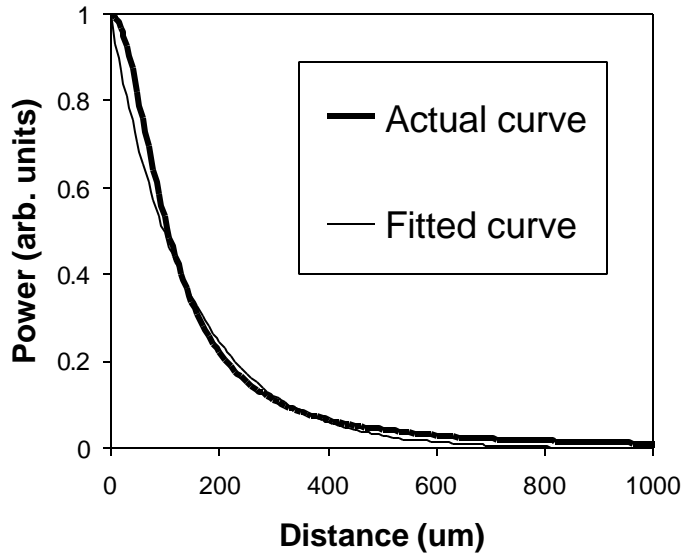


Fig. 3-9. The calculated power decay due to lateral diffraction in a planar waveguide. The thick line is based on the Gaussian beam expansion model and the thin line is an exponential fit.

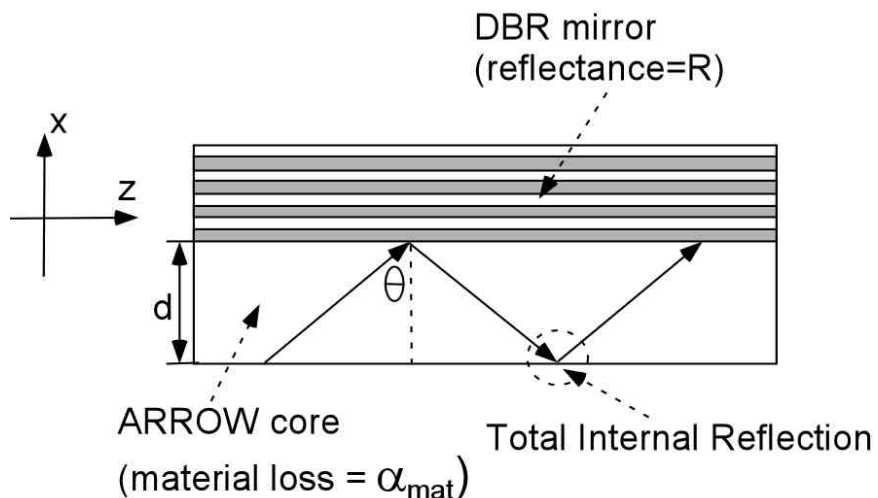


Fig. 3-10. An illustration of an ARROW with propagation losses: mirror leakage and core material absorption.

Apart from lateral diffraction, two other major loss mechanisms are present in an ARROW: material absorption and mirror leakage. For the device shown in Fig. 3-10, the optical power at a distance z from the origin can be expressed as

$$P(z) = P(0) \exp(-2\alpha_{\text{mod } e} z) R^{\frac{z}{2d \tan \theta}}, \quad (3-14)$$

where $\alpha_{\text{mod } e}$ is the modal propagation loss (due to material absorption) coefficient, θ is the mode angle, d is the core thickness and R is the DBR intensity reflectance. The modal loss coefficient is related to the core material absorption coefficient by

$$\alpha_{\text{mod } e} = \frac{\Gamma \alpha_{\text{mat}}}{\sin \theta}, \quad (3-15)$$

where α_{mat} is the material absorption coefficient and Γ is the fraction of the modal power confined in the core,

$$\Gamma = \frac{\int_0^d P(x) dx}{\int_{-\infty}^{+\infty} P(x) dx}. \quad (3-16)$$

Equation (3-14) can be rewritten in terms of the DBR transmittance T as

$$P(z) = P(0) \exp(-2\alpha_{\text{mod } e} z) (1 - T)^{\frac{z}{2d \tan \theta}}, \quad (3-17)$$

which, in the case of a highly reflective mirror ($T \ll 1$), becomes

$$P(z) \approx P(0) \exp(-2\alpha_{\text{mod } e} z) \left(1 - \frac{zT}{2d \tan \theta}\right) \approx P(0) \exp(-2\alpha_{\text{mod } e} z) \exp\left(\frac{-zT}{2d \tan \theta}\right). \quad (3-18)$$

The last approximation requires that $\frac{zT}{2d \tan \theta} \ll 1$, which is not unreasonable considering some typical ARROW parameters: the core thickness d is usually on the order of $1\mu\text{m}$, the waveguide length z is on the order of 1mm , and the DBR transmittance T can be made as low as 10^{-6} . With (3-18), one can now obtain the phenomenological loss coefficient α_s used in (3-6),

$$\alpha_s = \alpha_{\text{mod } e} + \alpha_{\text{DBR}} + \alpha_{\text{diff}} = \frac{\Gamma \alpha_{\text{mat}}}{\sin \theta} + \frac{T}{4d \tan \theta} + \alpha_{\text{diff}}. \quad (3-19)$$

3.3.2 Coupling strength between a fiber and an ARROW

An important parameter in (3-6) is the coupling coefficient C , which is proportional to the field overlap between the fiber and the ARROW. Obtaining a simple analytical expression for it, though, is not a trivial task, due to the complex mode shape of the ARROW. One way to extract a numerical estimate of the coupling coefficient is to analyze the coupled ARROW-fiber waveguide system with the transfer matrix method.

The transfer matrix method works for planar waveguides. In order to apply this to the analysis of a coupled ARROW-fiber system, the fiber somehow needs to be “planarized”. For this purpose, an equivalent slab model for step index single mode fibers developed by Sharma *et al.*²⁹ can be utilized. The basis for this model is that the modal field variation in the direction of interaction (i.e., the direction perpendicular to the plane of the ARROW) and the propagation constant for the fiber are matched, as closely as possible, to the modal field variation and the propagation constant of the equivalent slab waveguide.

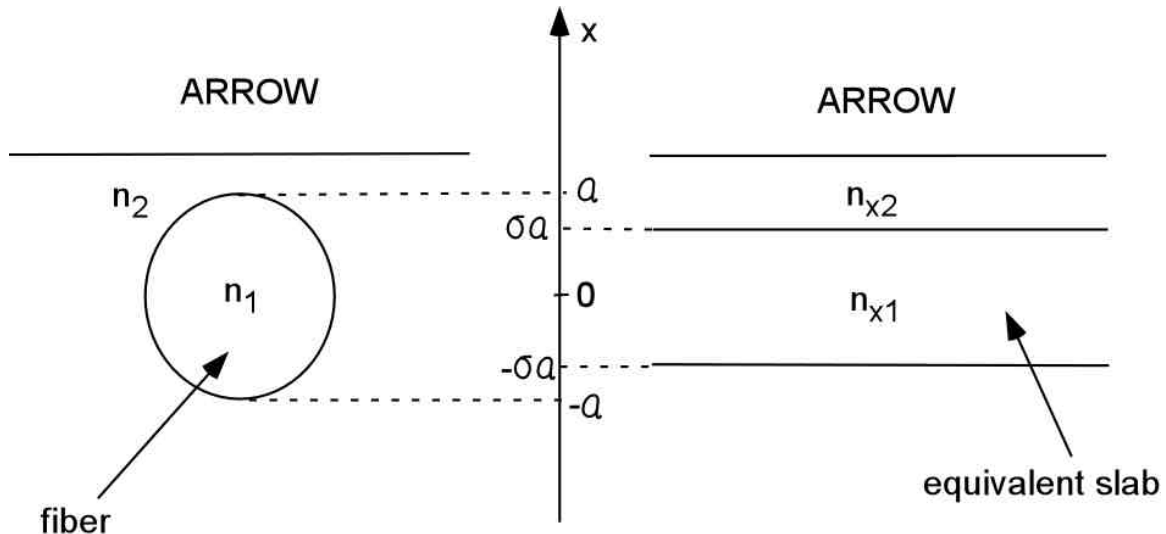


Fig. 3-11. The fiber in the polished half coupler shown on the left can be replaced by its equivalent slab waveguide shown on the right.

The results obtained by Sharma *et al.* are quoted here. For an ARROW-fiber coupler with its polished surface parallel to the y-z plane, the index distribution along the x-axis of the slab waveguide equivalent to the fiber (Fig. 3-11) is given by

$$\begin{aligned} n^2(x) &= n_{x1}^2 = n_1^2 - (U^2 - p^2)/(k_0 a)^2, & |x| < \sigma a \\ &= n_{x2}^2 = n_{x1}^2 - p^2 \sec^2(p\sigma)/(k_0 a)^2, & |x| > \sigma a \end{aligned} \quad (3-20)$$

where a is the core radius of the fiber, n_1 is the core index, $k_0 = 2\pi/\lambda$, the expressions for p and σ are

$$p^3 = -1.3528 + 1.6880V - 0.01894V^2, \quad (3-21)$$

$$\sigma = 0.8404 + 0.0251V - 0.0046V^2, \quad (3-22)$$

where V is defined by (2-21) and $U = a\sqrt{k_0^2 n_1^2 - \beta^2}$. β is the propagation constant of the fiber mode, which can be obtained from either the procedures outlined in section 2.3, or the well established empirical formula:³⁰

$$\beta^2 = k_0^2 n_1^2 - [V^2 - (1.1428V - 0.996)^2]/a^2, \quad 1.5 \leq V \leq 2.5 \quad (3-23)$$

where V is defined by (2-21).

Remaining cladding thickness (μm)	Effective index (Anti-bonding state)	Effective index (Bonding state)	Coupling length (μm)	Coupling Coefficient ($1/\mu\text{m}$)
1	1.45417	1.45663	338	0.004652
1.5	1.45448	1.45620	483	0.003255
2	1.45475	1.45593	699	0.002246
2.5	1.45494	1.45575	1023	0.001535
3	1.45508	1.45563	1502	0.001045

Table 3-1. The calculated coupling characteristics between a single mode fiber and an ARROW.

With a “planarized” fiber, the coupling coefficient can be obtained by calculating the transmission through the combined ARROW-fiber structure. As the distance between the two waveguides is reduced, the individual waveguide modes (with identical effective indices) transform into two coupled modes: an anti-bonding state (lower effective index) and a bonding state (higher effective index). The coupling length is the distance over which a phase difference of π is accumulated between the two modes,

$$L_c = \frac{\pi}{(\beta_b - \beta_a)} = \frac{\lambda}{2(n_b - n_a)}, \quad (3-24)$$

where n_b and n_a are the effective indices of the bonding and anti-bonding states respectively. The coupling coefficient can then be expressed as

$$C = \frac{\pi}{2L_c}. \quad (3-25)$$

In Table 3-1, the calculated coupling lengths and coefficients are tabulated as a function of the cladding thickness between the fiber and ARROW cores. In the calculation, the ARROW is the one described in section 3.2.2 and the fiber is a conventional 830nm single mode fiber (see Fig. 2-5). The field intensity distributions for the coupled modes in the case of 1μm separation are shown in Fig. 3-12. In the bonding state, the mode has the same phase in both wave guides, while in the anti-bonding state, the mode reverses phase (i.e., the field intensity drops to zero) between the wave guides.

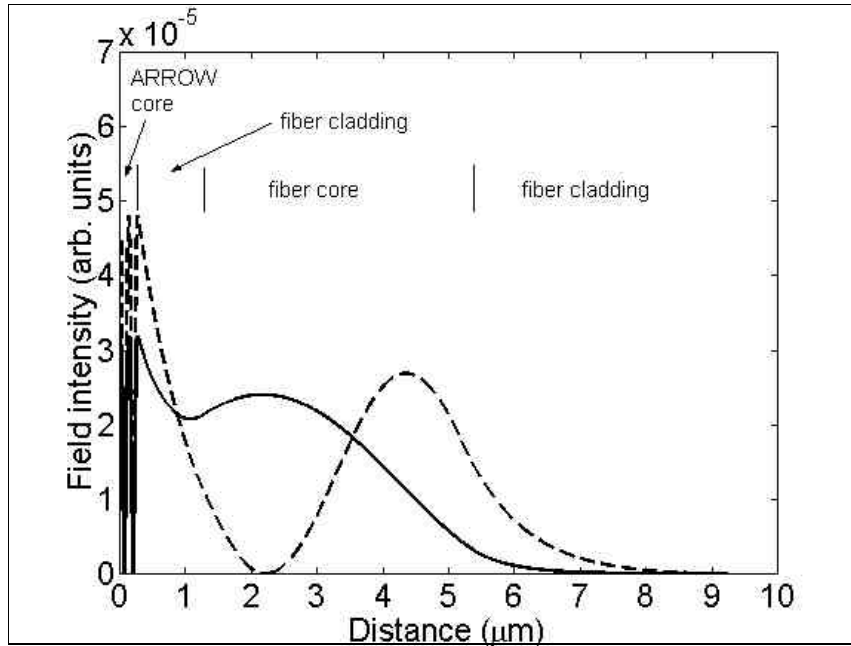


Fig. 3-12. The calculated field profiles for the two coupled modes of the ARROW-fiber structure. The solid line corresponds to the bonding state (higher effective index), and the dashed line corresponds to the anti-bonding state (lower effective index).

3.3.3 Coupled ARROW-fiber wave guide system

After obtaining the values of the coupling coefficient and the ARROW propagation loss, the power transmission through the fiber can be calculated using the

coupled-mode equations (3-6). Fig. 3-13 and Fig. 3-14 show the transmission as a function of the difference in propagation constants between the waveguides. Typical values for the coupling coefficient and the loss are used. The interaction length is assumed to be 1mm. The calculation shows that for a given coupling coefficient, C, an increasing loss, α_s , results in a shallower and broader transmission dip. And for a given loss, α_s , an increasing coupling coefficient, C, leads to a deeper dip.

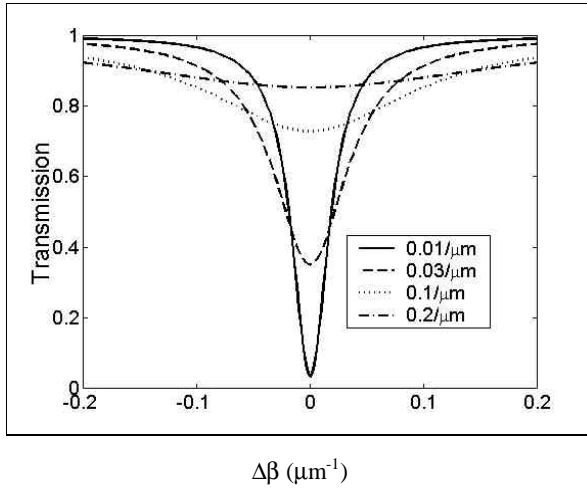


Fig. 3-13. The calculated fiber transmission of a coupled ARROW-fiber waveguide system. The coupling coefficient is $0.004\mu\text{m}^{-1}$, and the values in the legend are the propagation losses in the ARROW.

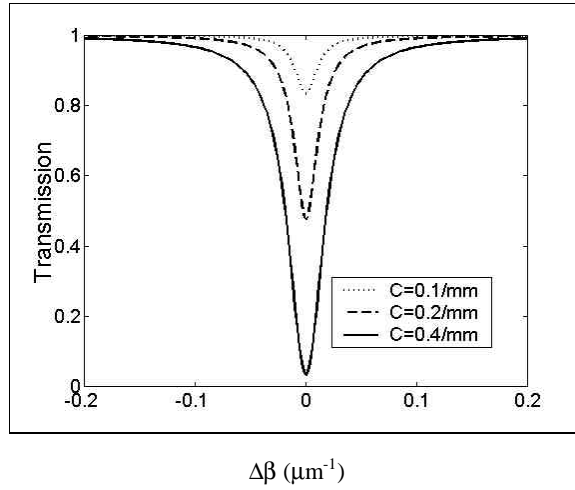


Fig. 3-14. The calculated fiber transmission of a coupled ARROW-fiber waveguide system. The ARROW propagation loss is $0.01\mu\text{m}^{-1}$, and the values in the legend are the coupling coefficients.

Chapter 4

In-line fiber filter and detector

The simplest realizable device in the ARROW-fiber coupled waveguide configuration is a narrow linewidth filter, where light at wavelengths at and near the resonant wavelength is coupled out of the fiber and into the ARROW. By incorporating an absorbing layer in the ARROW, the light signal can be converted into an electrical signal. Hence, a wavelength selective photodetector is realized. The design and experimental demonstration of these devices are described in this chapter.

4.1 Epitaxial growth

All ARROW samples in this work are grown by molecular beam epitaxy (MBE) on (100) GaAs substrates. MBE is basically an ultra-high-vacuum evaporation technique which allows for precise control of growth conditions. Under the correct conditions, the product material is a single crystal extended from the crystal lattice of the substrate. The detailed description of the theory and mechanics of MBE can be found in many excellent works.^{31,32}

A simplified schematic of a MBE growth chamber is shown in Fig. 4-1. The source materials are kept in effusion cells whose temperature can be actively controlled and kept constant throughout the growth process. The temperature of each cell in turn determines the evaporation rate, or molecular beam flux of the material. A common selection of source materials include As, Ga, Al, Si (n-type dopant) and Be (p-type dopant). For normal growth of III-V materials, the column V material (As in this case), is present in excess and the growth rate is controlled by the arrival rate of the column III materials. The substrate is heated during growth so that the absorbed material on the surface has enough thermal energy to find its proper lattice site for incorporation into the

crystal. The growth chamber of a MBE machine achieves ultra-high vacuum to minimize incorporation of undesired impurities, with a background pressure of below 10^{-10} Torr. During growth, typical beam pressures are in the 10^{-5} Torr range, but even at this pressure, the mean free path of the evaporated particles is much larger than the source-to-substrate distance. Therefore the flux of the evaporated material travels unimpeded towards the substrate in a line-of-sight “molecular beam”, which can be switched on or off by mechanical shutters placed in front of each source. Because the molecular beams impinge on the substrate at an angle, there is a large variation of the growth rate across the substrate surface. In order to reduce this inherent non-uniformity, the substrate is usually rotated during growth. The walls of the growth chamber are kept at liquid nitrogen temperature so that any excess material that fails to hit the substrate is absorbed. This prevents re-evaporation and hence the contamination of subsequently grown layers with different composition or dopants.

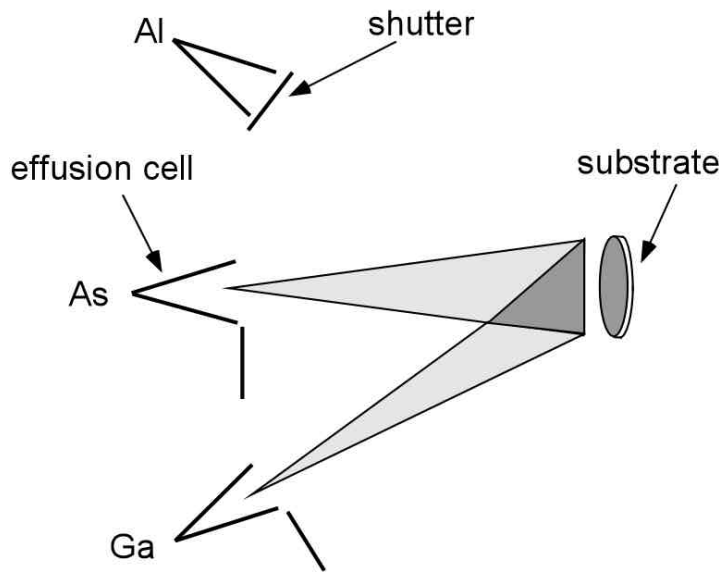


Fig. 4-1. Illustration of the MBE growth of gallium arsenide.

In addition to the capability of growing high quality crystal materials, MBE offers very precise control of layer thicknesses. The typical growth rate of $1\mu\text{m/h}$ corresponds to roughly one atomic layer per second. The switching speed of the shutters is fast

enough to make possible the reproducible growth of layers as thin as 10Å. However, during the growth of thick structures, such as DBR mirrors, the growth rate of a material can vary during growth. In order to limit the final thickness error to within one or two percent, *in situ* corrections can be performed.³³ This method involves measuring the reflectance spectra of a wafer during growth interruptions. Any discrepancy between the theoretical and measured spectra is then used to correct for growth rate variations. This technique is especially important for the growth of vertical cavity or ARROW-based modulators and lasers, where the wavelength spacing between the quantum well absorption or gain peak and the structure resonance is critical.

4.2 In-line fiber filter

Wavelength division multiplexing (WDM) increases the channel capacity of a fiber-optic system by transmitting multiple wavelengths over a single fiber. It is therefore desirable to have a simple method of extracting a specific wavelength without disturbing others going through the fiber. This is especially useful for such systems as multiprocessor interconnects for parallel-processing computers and local area networks (LAN's) with ring topologies.

One way to achieve this goal is to use an asymmetric waveguide coupler consisting of a single-mode fiber and a semiconductor ARROW. At certain discrete wavelengths, light is coupled from the fiber into the ARROW, due to phase-matching conditions. The large difference in the dispersion characteristics between the guides results in very sharp resonances at phase-matched wavelengths. In addition, the in-line architecture is a highly efficient fiber interface, with low insertion loss and good mechanical stability.

4.2.1 Device design

As shown in section 3.2.3, the resonance linewidth of an ARROW-fiber coupler is a function of the dispersion properties and the propagation loss of the ARROW, as well as the coupling strength between the waveguides. The dispersion of an ARROW is determined solely by its layer structure and can be controlled more easily than the other factors under our experimental arrangements, which will be described in the next section.

As shown in Fig. 4-2, the propagation constant of an ARROW becomes more sensitive to wavelength changes as the core thickness increases. This can be explained by examining equation 2-2 (the self-consistency condition of a dielectric waveguide): for a given change in λ , a larger d requires a larger change in $\cos\theta$ to maintain the equality. This is very similar to the case of a Fabry-Perot etalon where a longer cavity length results in narrower resonances.³⁴

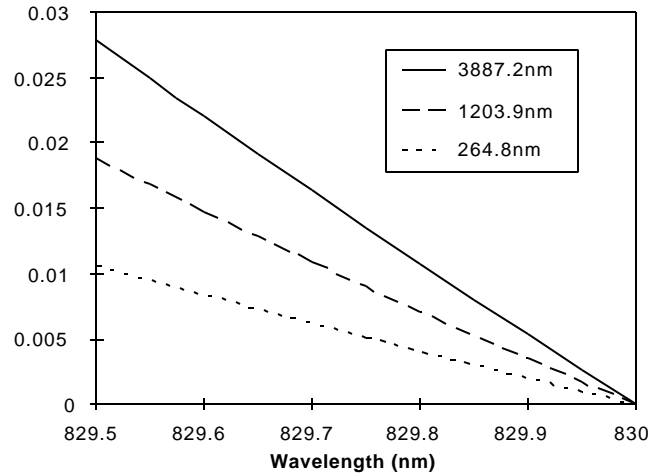


Fig. 4-2. The calculated difference in propagation constants between the fiber mode and the TE ARROW mode. The three curves represent three ARROWS with the same DBR (as the one shown in Fig. 4-3) but different core thicknesses (core material = $\text{Al}_{0.33}\text{Ga}_{0.67}\text{As}$). The unit for y-axis is μm^{-1} .

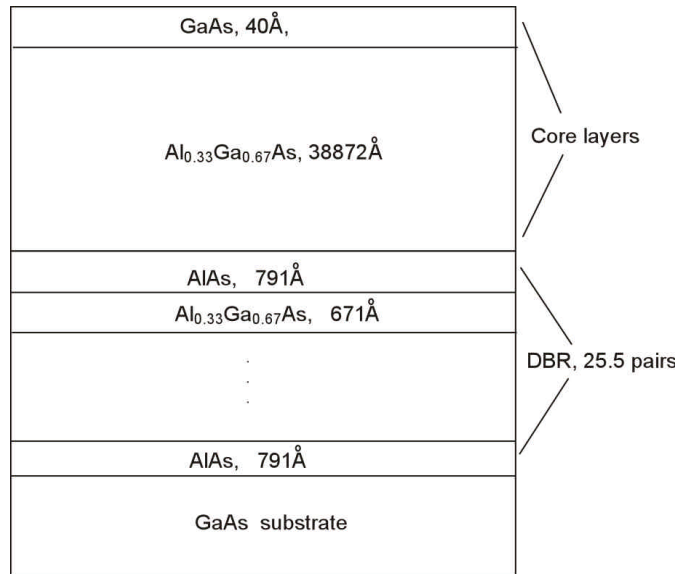


Fig. 4-3. The epitaxial structure of the ARROW used in the filter.

The epitaxial structure of the ARROW is shown in Fig. 4-3. All layers are undoped. An $\text{Al}_{0.33}\text{Ga}_{0.67}\text{As}$ core of $3.887\mu\text{m}$ was chosen for this experiment. $\text{Al}_{0.33}\text{Ga}_{0.67}\text{As}$ was used because its absorption onset wavelength is well below the operating wavelength of 830nm. The core thickness was chosen to minimize the linewidth, while keeping the MBE growth time within a reasonable limit. The AlAs/ $\text{Al}_{0.33}\text{Ga}_{0.67}\text{As}$ DBR was designed to provide maximum reflectance at an incident angle of 25 degrees, which is the mode angle needed for phase-matching to a single-mode fiber. The calculated dispersion curves for the ARROW are shown in Fig. 4-4, showing phase-matching conditions at 818nm (TM) and 830nm (TE). TE polarization here is defined as the case where the electric field vector lies parallel to the GaAs substrate plane.

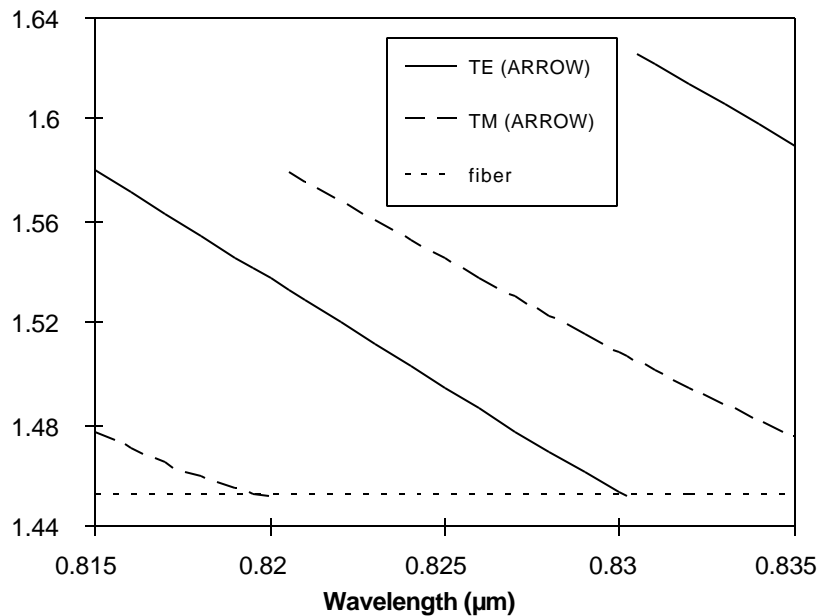


Fig. 4-4. The calculated dispersion curves for the single mode fiber and the highest order confined modes of the ARROW. The y-axis shows the effective propagation indices.

4.2.2 Experiment

Following MBE growth, the ARROW wafer was cleaved into pieces for testing. During testing, a polished fiber half coupler (from Canadian Instrumentation and Research Ltd.) was mounted on an x-y-z stage and positioned on top of the ARROW

piece. The fiber half coupler is made by epoxying a single mode fiber into a curved groove in a glass substrate and then polishing both the substrate and the fiber cladding to within a few microns of the fiber core.³⁵ The polished interaction region is about 1mm in length. The ends of the fiber are spliced to patch cords, which can then be connected to other fibers, optical sources or testing instruments. The ARROW piece was placed on a thermoelectric temperature controller. Drops of index matching fluid ($n=1.458$), whose index was closely matched to that of the fiber cladding ($n=1.452$), were applied between the fiber block and the ARROW to ensure good optical contact. The optical source used was a fiber coupled GaAs (~830nm) laser diode biased just below threshold. A polarizer and a fiber polarization controller were used at the input end. The transmission spectra of the system were measured with a HP70951A optical spectrum analyzer. The experimental setup is shown in Fig. 4-5.

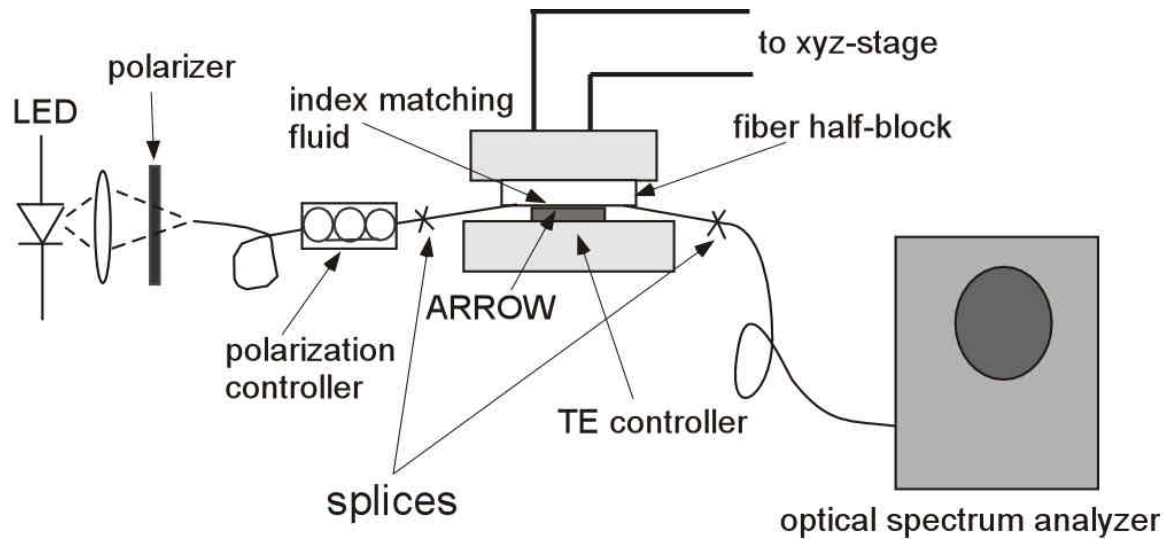


Fig. 4-5. The experimental setup for testing in-line fiber filters.

4.2.3 Results and discussion

Fig. 4-6a. shows the measured transmission spectra of the filter at 25°C. The TE dip has a full-width at half-maximum (FWHM) of 0.5nm and the TM dip has a FWHM of 1.3nm. The TM dip is broader because the DBR mirror reflectance is lower (Fig.3-3) and hence the ARROW propagation loss is higher. Fig. 4-6b shows the simulated results using the coupled mode equations (3-4). The differences between the simulated and

measured results are primarily due to the simplicity of the model (for example, the curvature of the interaction region is ignored). They can also be attributed to measurement errors (such as those due to the finite resolution bandwidth of the optical spectrum analyzer). The positions of the resonance dips are shifted from the design wavelengths due to thickness variations in MBE growth. The off-resonance insertion loss (~ 2 dB) of the system is due to imperfect fiber splicing.

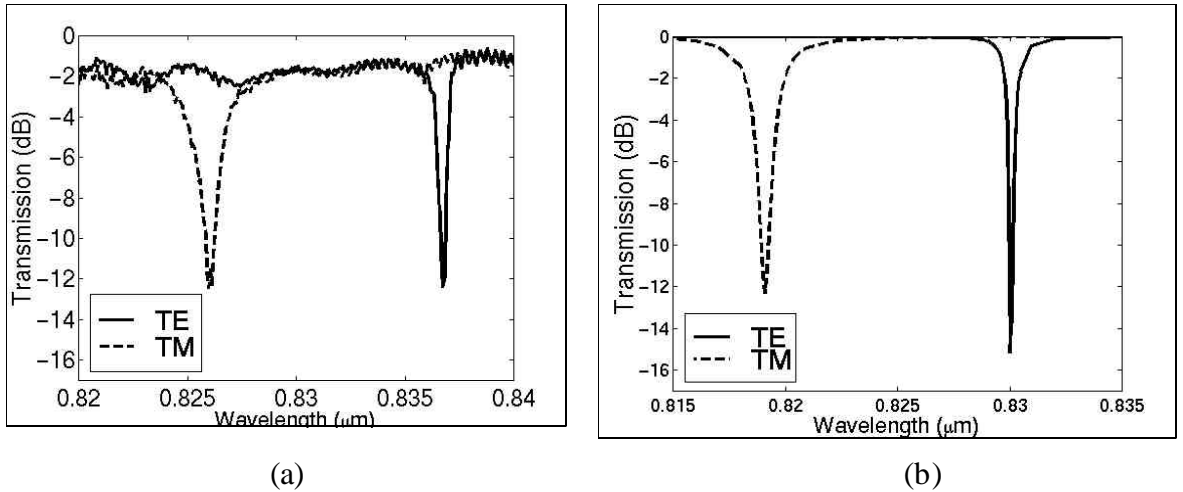


Fig. 4-6. (a) The measured transmission spectra at 25°C; (b) The simulated spectra. The parameters used for the simulation are: $C = 0.005 \mu m^{-1}$, $\alpha = 0.003 \mu m^{-1}$ (TE), $\alpha = 0.018 \mu m^{-1}$ (TM).

The transmission spectra of the filter under different temperatures are shown in Fig. 4-7. As the temperature of the ARROW increases, the refractive index of GaAs/AlGaAs increases and therefore the phase-matched wavelength red-shifts. The total shift of 3nm over a 50°C range corresponds to a core index change of 0.005 ($dn/dT \approx 1 \times 10^{-4}$), which is consistent with values reported in the literature.³⁶

By increasing the layer thicknesses, such structures can be extended to operate at the fiber communication wavelengths of 1300nm or 1550nm. The filter linewidth and the rejection ratio depend on the ARROW propagation loss, the coupling strength and the interaction region curvature and length. The ARROW propagation loss can be controlled by, for example, creating a ridge waveguide structure which limits lateral diffraction (Fig. 4-8). The coupling strength and the interaction region characteristics are essentially determined by the fabrication process of the fiber half coupler, over which we do not

presently have control. The development of silicon V-grooves-based fiber half couplers,³⁷ where both the polishing depth and the interaction length can be lithographically determined, will lend further flexibility to the design of in-line fiber devices.

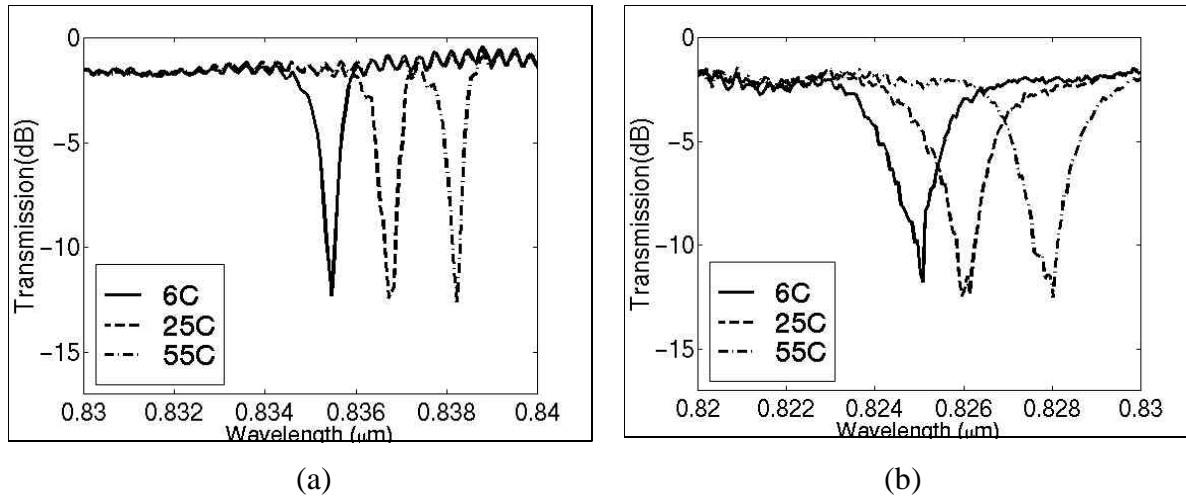


Fig. 4-7. The experimental TE (a) and TM (b) transmission spectra of the in-line fiber filter under different temperatures.

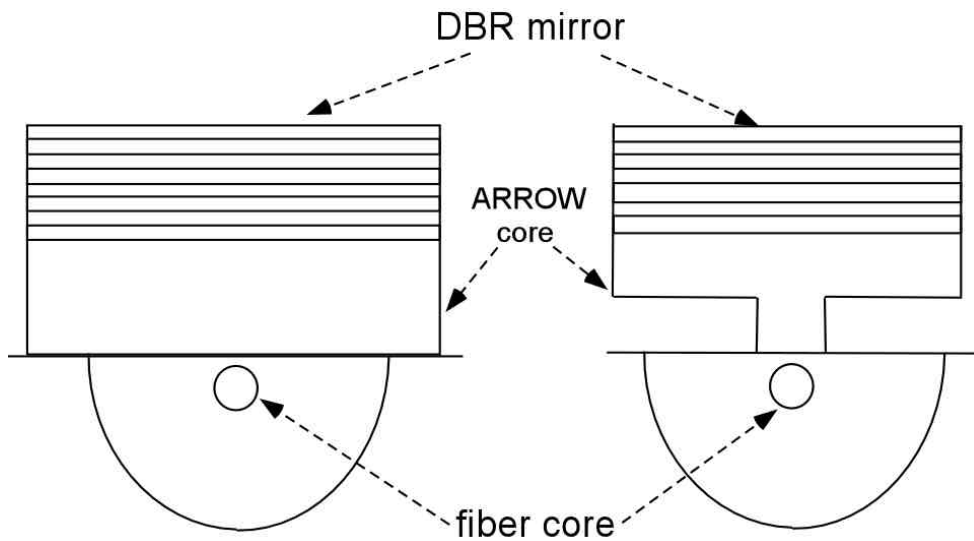


Fig. 4-8. Cross section views of an in-line fiber filter. The drawing on the left depicts the current device. The drawing on the right shows an ARROW with a ridge structure for controlling lateral diffraction.

4.3 Wavelength selective in-line fiber photodetector

In some applications, once light at a specific wavelength is filtered out of a single-mode fiber, it is desirable to convert it into an electrical signal. This can be accomplished by incorporating absorbing quantum wells in the core of the ARROW, turning an in-line fiber filter into a photodetector. At the phase-matched wavelength, the light traveling in the fiber is extracted into the ARROW and absorbed in the quantum well(s), generating a photocurrent. In addition to its wavelength-selective nature, this type of detector has a distributed absorbing structure which is conducive to high-speed, high-power operation.³⁸ The in-line fiber interface also allows for low insertion loss and low cost packaging.

4.3.1 Device design

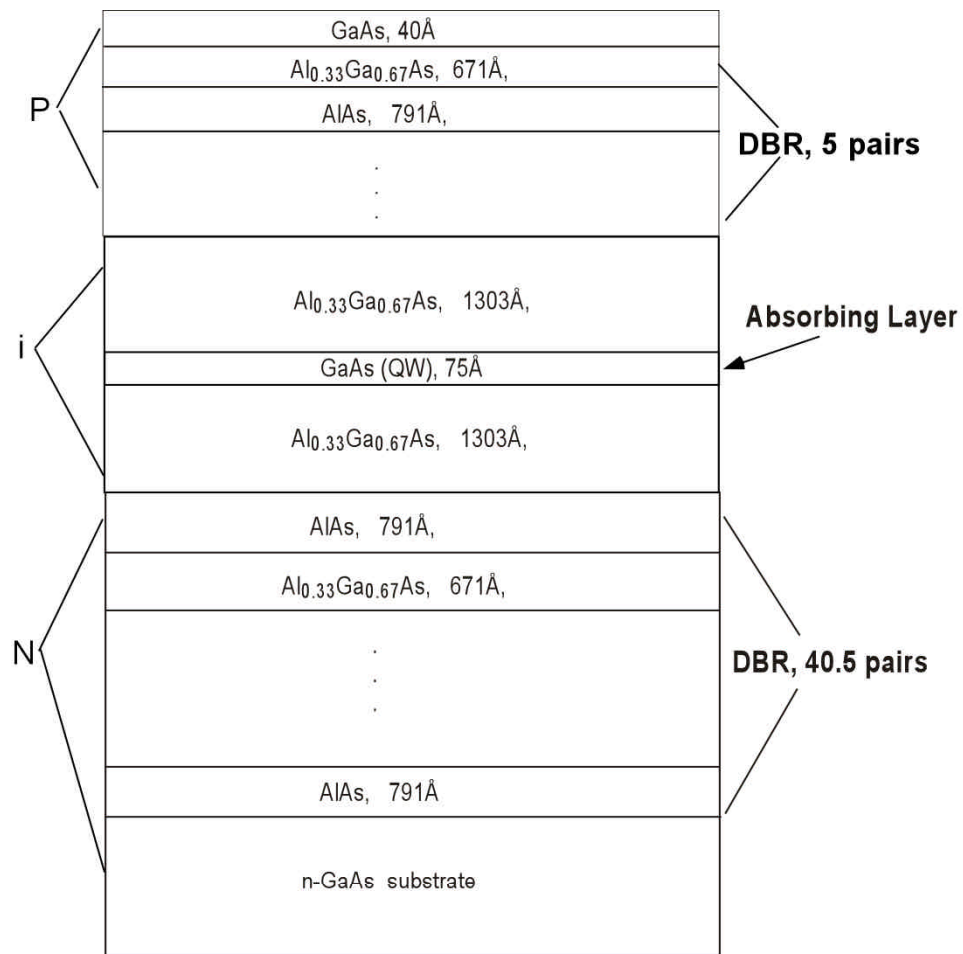


Fig. 4-9. The epitaxial structure of the ARROW used in the in-line detector.

The epitaxial structure of the absorbing ARROW is shown in Fig. 4-9. Similar to conventional photodetectors, the DBR mirrors were doped to form a p-i-n structure, and an absorbing quantum well was placed in the intrinsic region. The doping concentrations are $1 \times 10^{19} \text{ cm}^{-3}$ for the p-type layers and $1 \times 10^{18} \text{ cm}^{-3}$ for the n-type layers. When the ARROW is attached to the polished fiber half coupler, optical waves can be guided in its core by reflection from the n-doped DBR mirror on the one side, and a combination of reflection from the p-doped DBR mirror and total internal reflection from the fiber cladding on the other side. The n-type and p-type DBR mirrors consist of 40 and 5 pairs of AlAs/Al_{0.33}Ga_{0.67}As quarter wave layers, respectively. The p-type mirror was designed to be partially reflective so that there is sufficient field overlap between the guided modes of the fiber and the ARROW. The core of the ARROW is made up of an Al_{0.33}Ga_{0.67}As layer and a 75 Å GaAs quantum well. The quantum well was placed at the center of the core where the intensity peak of the guided ARROW mode occurs, in order to maximize the quantum efficiency.

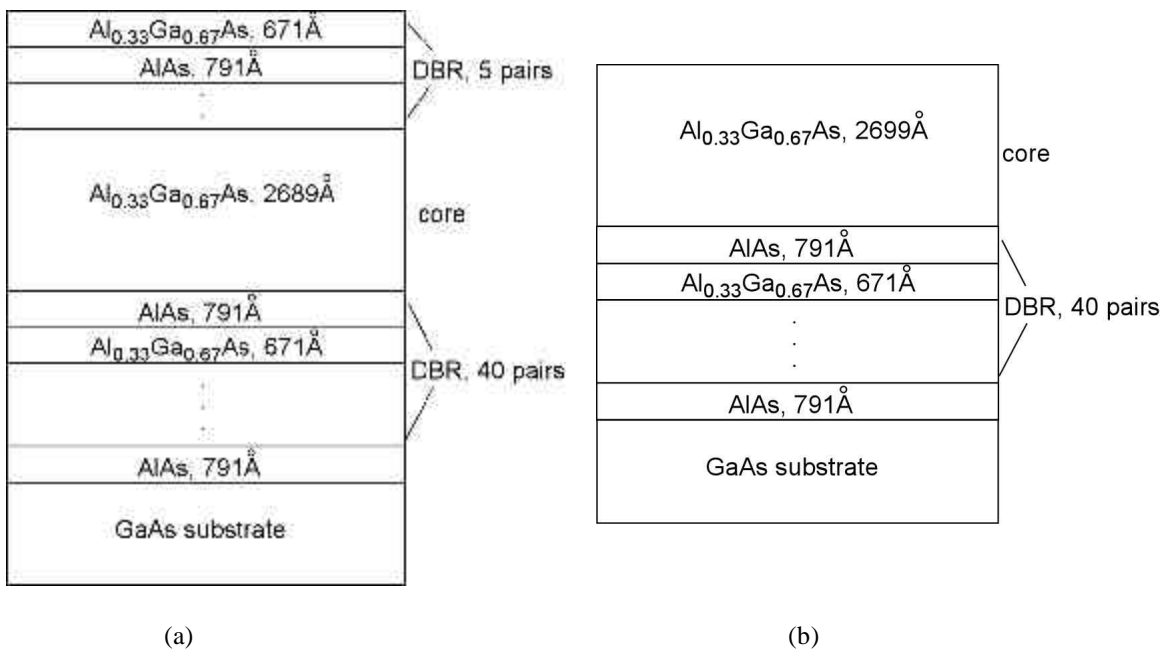


Fig. 4-10. The structures of two ARROWS: (a) with a leaky DBR, and (b) without a leaky DBR. The phase-matched wavelength is 830nm for both waveguides.

An ARROW with two mirrors was chosen because compared with its equivalent single mirror version, it has a steeper dispersion curve and therefore a narrower resonance linewidth. Fig. 4-10 shows the schematic diagram of two ARROWS, one with one mirror and the other with two mirrors, while both having the same phase-matched wavelength. The calculated dispersion curves for the two are plotted in Fig. 4-11. As shown in section 4.2.1, another way to decrease the resonance linewidth is to increase the core thickness. The disadvantage of this approach is that with a thick core, the optical field intensity varies rapidly and any slight misplacement of the quantum well can lead to a large reduction in the detector quantum efficiency.

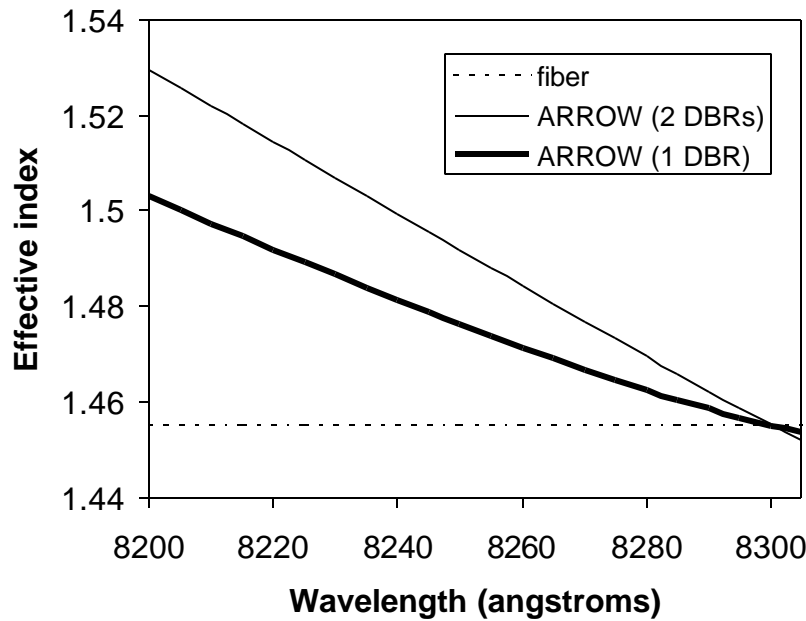


Fig. 4-11. The calculated dispersion characteristics of the two ARROWS illustrated in Fig. 4-10.

4.3.2 Experiment

Individual devices were defined on the MBE-grown wafer by standard wet chemical etching (with a 1:5:160 mixture of $\text{H}_2\text{SO}_4:\text{H}_2\text{O}_2:\text{H}_2\text{O}$). Au/Ge/Ni/Au ($400\text{\AA}/125\text{\AA}/120\text{\AA}/1000\text{\AA}$) layers were evaporated on the backside of the substrate and thermally annealed (405°C for 30 seconds) to form a n-type ohmic contact. Patterned Ti/Au ($250\text{\AA}/1000\text{\AA}$) layers formed a p-type ohmic contact on top of each device. The wafer was then cleaved into pieces (4mm by 3mm). The setup that was used for filter

testing (Fig. 4-5) was used here, with the addition of an infrared CCD camera which can be focused on the polished interaction region of the coupler. The position of the fiber core was determined by launching light from a tunable GaAs laser diode into the fiber half coupler and observing the scattered light with the camera. After aligning the fiber core to the ARROW, the two waveguides were brought into contact, with index matching fluid applied at the interface. The tunable laser diode that was used for aligning then served as the light source for device testing. A 5V reverse bias was applied to the p-i-n junction within the ARROW and a $10\text{k}\Omega$ series resistor. The photocurrent was obtained by measuring and converting the voltage that appeared across the resistor (Fig. 4-12).

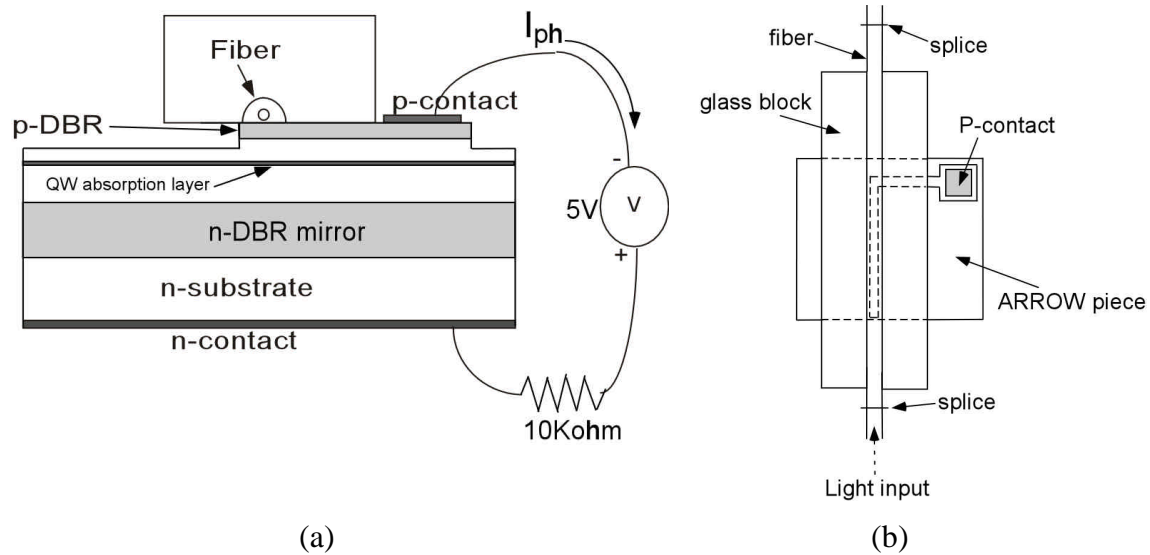


Fig. 4-12. Illustration of photodetector testing arrangement: (a) cross-sectional view, and (b) top view.

4.3.3 Results and discussion

Fig. 4-13a shows the photocurrent as a function of wavelength of TE-polarized light (electric field vector parallel to the plane of the GaAs substrate) traveling through the fiber. The response peaks at 816nm with a FWHM of 1.6nm. The laser power coupled into the input single mode fiber was about $42\mu\text{W}$, which means our detector has an external quantum efficiency of 75%. The TE transmission spectrum of the device measured with an optical spectrum analyzer is shown in Fig. 4-13b. The broadband light

source was the same laser diode biased below threshold. The resonance positions and shapes in the two figures are consistent with each other.

The off-resonance transmission of our device (Fig. 4-13b) is about 70%, with the loss coming from poor fiber splicing. By reversing the light traveling direction and obtaining essentially the same photocurrent response, we concluded that each of the two splices had a power transmission of about 83% ($0.83^2 = 0.7$). Therefore, with a perfect splice, our detector would achieve an external quantum efficiency of more than 90%. The polarization sensitivity of the device could be eliminated by defining a ridge waveguide in the semiconductor (which compensates for the TE and TM modal dispersion) and using strained quantum wells (which equalizes the TE and TM absorption).³⁹ By changing the quantum well material composition (from GaAs to InGaAs or GaInNAs), this device can operate at longer wavelengths and prove useful for low cost WDM applications.

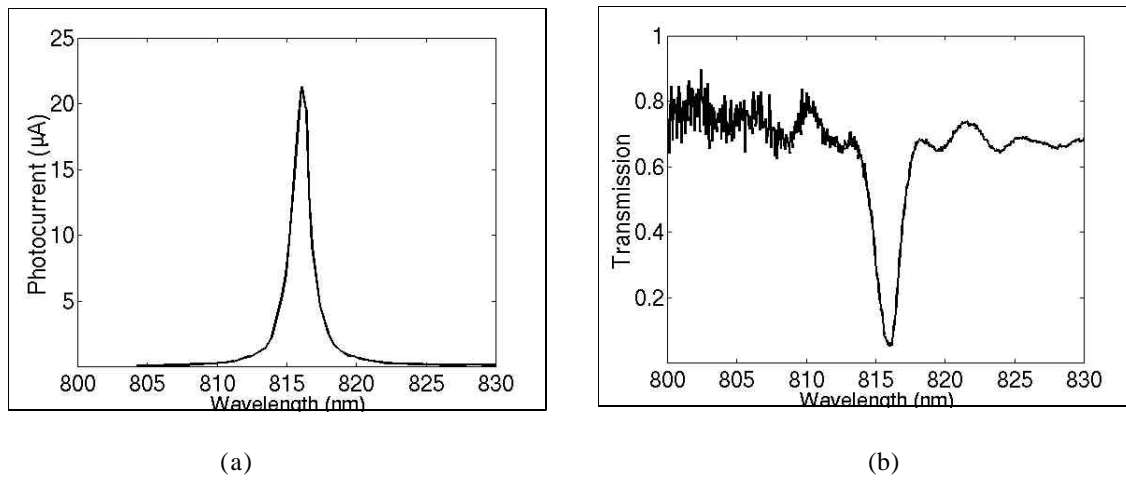


Fig. 4-13 (a) The measured photocurrent response. (b) The measured device transmission.

Chapter 5

In-line fiber modulator

External optical modulators have an important role in high-speed photonic links because of their low chirp characteristics compared with directly modulated semiconductor lasers.^{40,41} In this chapter, the design and experimental demonstration of GaAs/AlGaAs optical intensity modulators based on the ARROW-fiber coupled waveguide structure are presented.

5.1 Quantum well physics

As shown previously, the shape and the position of the resonance dip in an ARROW-fiber system are functions of the refractive indices (both real and imaginary parts) of the ARROW layers. Therefore, by changing these refractive index values, the intensity of the light going through the fiber can be modulated.

The refractive index of a semiconductor structure can be modified through either bulk effects such as carrier injection,⁴² or quantum phenomena such as the quantum confined Stark effect (QCSE).^{43,44} As its name suggests, carrier injection requires the application of an injection current and is therefore less power efficient than the QCSE, which only requires the application of an electric field. As a result, the modulation mechanism chosen for our devices is the QCSE.

5.1.1 Quantum confined Stark effect

In a direct gap semiconductor, the optical absorption near the band edge is affected by bound electron-hole pairs, which are formed as a result of the Coulomb interaction between electrons and holes. These electron-hole pairs are called excitons. A simple theoretical treatment of excitons can be performed by writing the exciton wave

function as a wave packet constructed from the linear combination of electron and hole Bloch functions, and then solving the Schrödinger equation.⁴⁵ The resultant excitonic absorption can be expressed as

$$\alpha(\omega) \propto |d_{cv}|^2 \sum_n |\phi_n(r=0)|^2 \delta(\hbar\omega - E_g + \frac{E_B}{n^2}), \quad (5-1)$$

where $|d_{cv}|^2$ is the interband dipole matrix element, $|\phi_n(r=0)|^2$ specifies the probability to find the electron at the same lattice site as the hole. E_B/n^2 gives the binding energy for the n th excitonic state, where E_B is a constant known as the Rydberg energy. In the case of III-V compound semiconductors, the Rydberg energy ranges from 1 to 100meV, corresponding to Bohr radii of about 10 to 500Å.

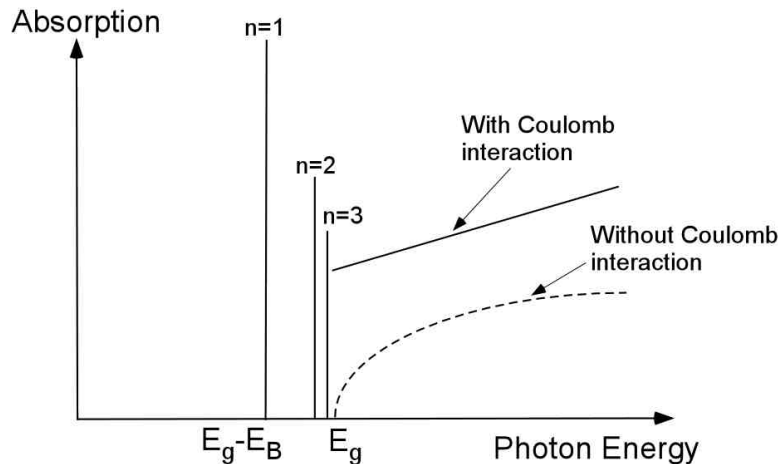


Fig. 5-1. Schematic of a semiconductor absorption spectrum. Coulomb interaction not only creates excitonic resonances below the bandgap, but also enhances the above-bandgap continuum absorption.

The most striking difference between free-carrier absorption (without Coulomb interaction between electrons and holes) and real semiconductor absorption is that the former is nonexistent for energies below the bandgap, whereas the latter consists of discrete lines (excitonic resonances) below the bandgap (Fig. 5-1). However, this effect is rarely observed for bulk semiconductors at room temperature because of impurity and phonon scatterings, which eliminates any practical device concepts utilizing excitonic effects in bulk materials.

If the electrons and holes can be confined spatially in one direction (as in the case of a quantum well with dimensions comparable to the Bohr radius), it is expected that the excitonic absorption spectrum will be different from the bulk (3D) case due to quantum confinement effects. It can be shown that the 2D excitonic absorption (with an infinite potential well in the z-direction) is of the form⁴⁵

$$\alpha^{2d}(\omega) \propto |d_{cv}|^2 \sum_{i,j,n} \left| \langle \zeta_{ei}(z_e) | \zeta_{hj}(z_h) \rangle \right|^2 \left| \phi_n^{xy}(r_{xy}=0) \right|^2 \delta(\hbar\omega - E_n^{2d}), \quad (5-2)$$

where $|d_{cv}|^2$ is the dipole matrix element as in (5-1), $\left| \langle \zeta_{ei}(z_e) | \zeta_{hj}(z_h) \rangle \right|^2$ gives the overlap integral of the electron-hole envelope function in the z-direction, and $\left| \phi_n^{xy}(r_{xy}=0) \right|^2$ is the probability that the electron and the hole are in the same unit cell. E_n^{2d} is expressed as

$$E_n^{2d} = E_g + E_{hj} + E_{ei} - \frac{E_B}{(n-1/2)^2}, \quad (5-3)$$

which corresponds to a series of excitonic transition energies. E_B is the 3-dimensional exciton Rydberg energy, E_{hj} and E_{ei} are the confinement energies of the i th electron subband and the j th hole subband. In practice, the δ -function absorption spectra in a quantum well structure is broadened by several mechanisms, including: interface roughness, well to well thickness fluctuations in multiple quantum well (MQW) samples, background impurity scattering and phonon scattering. In high quality GaAs/AlGaAs MQW samples, the excitonic resonance linewidth is approximately 3 to 4 meV.

Comparing equations (5-1) and (5-2), the most obvious difference lies in the energy term. In the 2D case, not only is the effective bandgap shifted due to electron and hole confinement energies, but also the binding energy is increased as can be seen from the $(n-1/2)^2$ dependence in the denominator (e.g., for n=1, the 2D binding energy is 4 times larger than the 3D binding energy). Also in two dimensions, the relative separation between the electron and the hole is reduced because of quantum confinement. As a result, the $\left| \phi_n^{xy}(r_{xy}=0) \right|^2$ term, which describes the probability that the electron and the hole are in the same location, is larger. The increase in oscillator strengths and binding energies results in sharp absorption peaks which persist up to high temperatures. This feature distinguishes quantum wells from bulk materials and makes quantum well

excitonic devices realizable. It should be mentioned, however, that the exciton situation in a quantum well with finite barrier heights is intermediate between the 2D and 3D cases, although it has most of the qualitative features of the 2D case.

In an infinite potential well, the overlap integral term $\left| \langle \zeta_{ei}(z_e) | \zeta_{hj}(z_h) \rangle \right|^2$ is zero if $i \neq j$. This imposes one of the selection rules for optical absorption in two dimensions: the allowed transitions are those between the quantized electron and hole states with the same quantum numbers. In practical cases, the potential well is always finite and transitions with $i \neq j$ are allowed, albeit weakly. One other selection rule pertains to the dipole matrix element $|d_{cv}|^2$. Calculations⁴⁵ show that for light polarized in the plane of the quantum well, the ratio of the matrix element of the heavy-hole exciton to the light-hole exciton is 3:1. However this ratio is 0:1 for light polarized normal to the plane of the quantum well, suggesting that heavy-hole excitonic transition is not allowed.

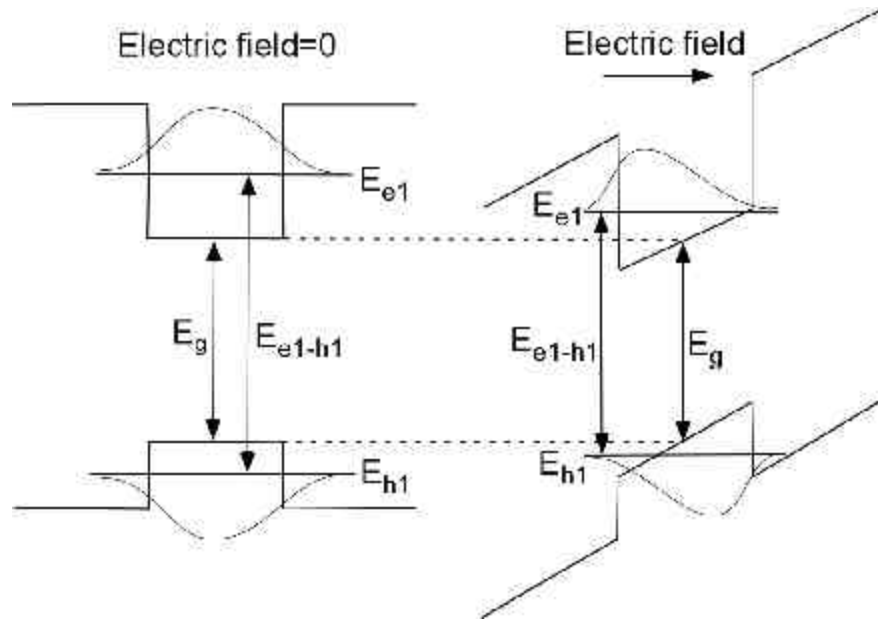


Fig. 5-2. Illustration of the change in confinement energies and wave function overlap when a perpendicular electric field is applied to a quantum well.

When an electric field is applied perpendicular to the plane of a quantum well, the potential energy experienced by the electron and the hole is modified spatially (Fig. 5-2), as are the confinement energies. The field also pushes the electron and the hole to the

opposite walls of the well because of the opposite charges of the two particles, thereby reducing the overlap between the wave functions. As a result, both the position of the absorption peak and the transition strength change due to the applied field. The range of applied electric field strengths and the amount of absorption shift can be greatly enhanced through quantum confinement. In a 3D structure, because the Bohr radius is on the order of 100Å, and the binding energy is on the order of 10~100meV, moderate electric fields of about 10mV per 100Å, or 10kV/cm, are enough to ionize the excitons. This effect can be observed in a quantum well structure when the field is parallel to plane of the well. With a perpendicular field, the potential well confines the carriers, the ionization occurs only if the carriers tunnel out of the well. Therefore it is possible to apply fields as large as 50 times the classical ionization field, inducing red-shifts in the absorption peak 2.5 times the binding energy, and still observe excitonic resonances.⁴⁶ This phenomenon is known as the quantum confined Stark effect (QCSE). In Fig. 5-3, several measured absorption spectra for a MQW sample under different biases are shown.⁴⁷

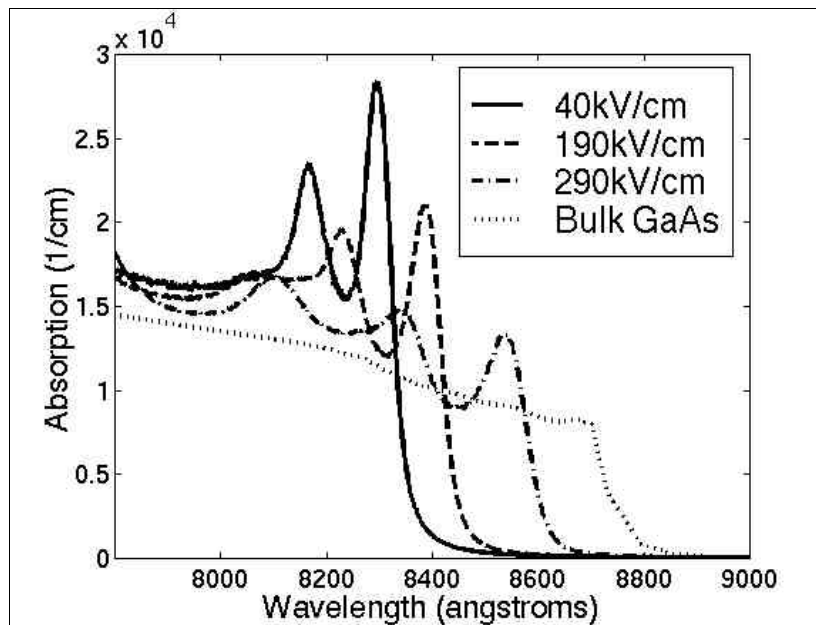


Fig. 5-3. The measured absorption spectra for 75Å GaAs quantum wells with 35Å AlAs barriers. The polarization of the light is TE (parallel to the MQW plane). Details of the experimental procedures can be found in reference 34.

5.1.2 Kramers-Kronig relations

The absorption and dispersion of a material are intimately related. Neglecting any non-linear effects, the relation between the electric polarization of a material and the applied field is expressed as

$$P(\omega) = \epsilon_0(\chi'(\omega) + j\chi''(\omega))E(\omega), \quad (5-4)$$

where P is the polarization, E is the applied field, ϵ_0 is the permittivity of free space, and χ' and χ'' are the real and imaginary parts of the complex susceptibility. Since equation (5-4) describes a linear shift-invariant causal system, the real and imaginary parts of the transfer function $\chi(\omega)$ are related by what is known as the Kramers-Kronig relations:⁴⁸

$$\chi'(\omega) = \frac{2}{\pi} P \int_0^\infty \frac{\omega' \chi''(\omega')}{\omega'^2 - \omega^2} d\omega' \quad (5-5)$$

$$\chi''(\omega) = \frac{2}{\pi} P \int_0^\infty \frac{\omega \chi'(\omega')}{\omega^2 - \omega'^2} d\omega'. \quad (5-6)$$

The ‘P’ in the equations denotes that the Cauchy principal values of the integrals are evaluated, i.e.,

$$\int_0^\infty = \lim_{\Delta \rightarrow 0} \left(\int_0^{\omega-\Delta} + \int_{\omega+\Delta}^\infty \right), \quad \Delta > 0. \quad (5-7)$$

The complex dielectric constant of a material is directly related to its susceptibility

$$\epsilon_r = \epsilon'_r + j\epsilon''_r = 1 + \chi' + j\chi'', \quad (5-8)$$

and the complex index of refraction is defined as

$$N = n - j\kappa = \sqrt{\epsilon_r} = \sqrt{\epsilon'_r + j\epsilon''_r}. \quad (5-9)$$

For semiconductors, one usually finds that $\epsilon'_r \gg \epsilon''_r$ for the wavelength ranges of interest. Therefore equation (5-9) can be approximated as

$$N = n - j\kappa \approx \sqrt{\epsilon'_r} + j \frac{\epsilon''_r}{2\sqrt{\epsilon'_r}}. \quad (5-10)$$

The intensity absorption coefficient can then be written as

$$\alpha(\omega) = \frac{4\pi\kappa(\omega)}{\lambda} = -\frac{\omega}{c\sqrt{\epsilon'_r(\omega)}} \epsilon''_r(\omega) \approx -\frac{\omega}{cn_b} \epsilon''_r(\omega), \quad (5-11)$$

where $\sqrt{\epsilon'_r(\omega)}$ is replaced by a constant, n_b , because in practice, the real part of the refractive index experiences little fractional changes over the relevant wavelengths. Substituting (5-8) into (5-5) and expressing χ in terms of α and ϵ'_r , one obtains

$$\Delta\epsilon'_r(\omega) = \frac{2}{\pi} P \int_0^\infty \frac{-cn_b \Delta\alpha(\omega')}{\omega'^2 - \omega^2} d\omega'. \quad (5-12)$$

With $\Delta\epsilon'_r(\omega) \approx 2n_b \Delta n(\omega)$ and changing the variable from ω to λ , (5-12) becomes

$$\Delta n(\lambda) = \frac{1}{2\pi^2} P \int_0^\infty \frac{\Delta\alpha(\lambda') d\lambda'}{1 - (\lambda'/\lambda)^2}. \quad (5-13)$$

This is the form of the relationship used to calculate refractive index changes due to changes in absorption. For example, when a MQW sample has different absorption spectra under different biases, the difference of these absorption curves could be used to determine the difference in refractive index induced by the field. Fig. 5-4 shows the calculated refractive index based on the absorption values shown in Fig. 5-3.

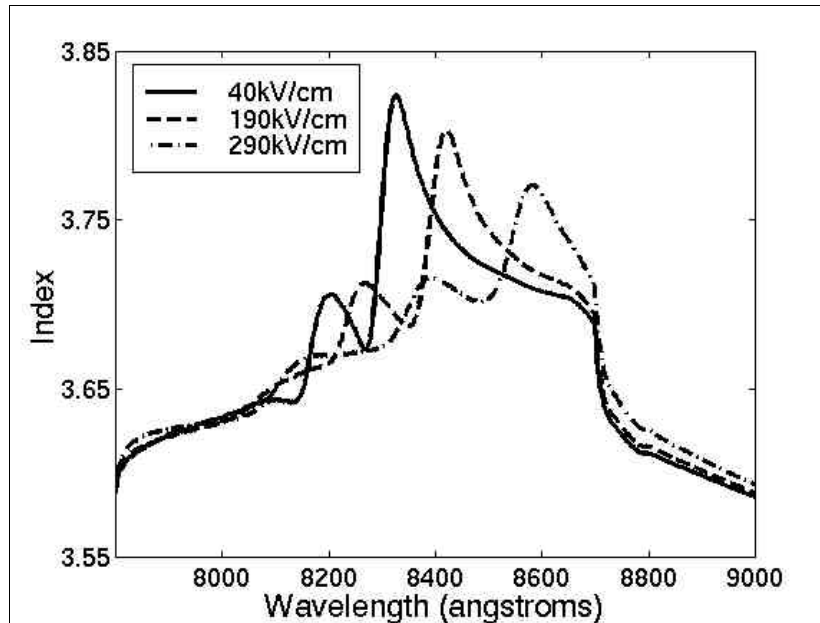


Fig. 5-4. The calculated refractive index for 75 Å GaAs quantum wells with 35 Å AlAs barriers. The index changes with respect to bulk GaAs values are calculated using the Kramers-Kronig relationship. The bulk GaAs index values are taken from reference 11.

5.2 Modulator with single-mirror ARROW

5.2.1 Device design

A simple way to realize in-line fiber light modulation is to use an ARROW which consists of a MQW core layer and a single DBR. When the wafer is attached to a side-polished single mode fiber, waveguiding is achieved in the core layer by reflection from the DBR and total internal reflection from the fiber cladding. By applying an electric field perpendicular to the plane of the quantum wells, the complex index of refraction of the MQW layer is changed through the QCSE, which results in both a shift in the phase-matched wavelength and a change in the shape of the resonance dip. Therefore, intensity modulation of the transmitted light through the fiber can be obtained.

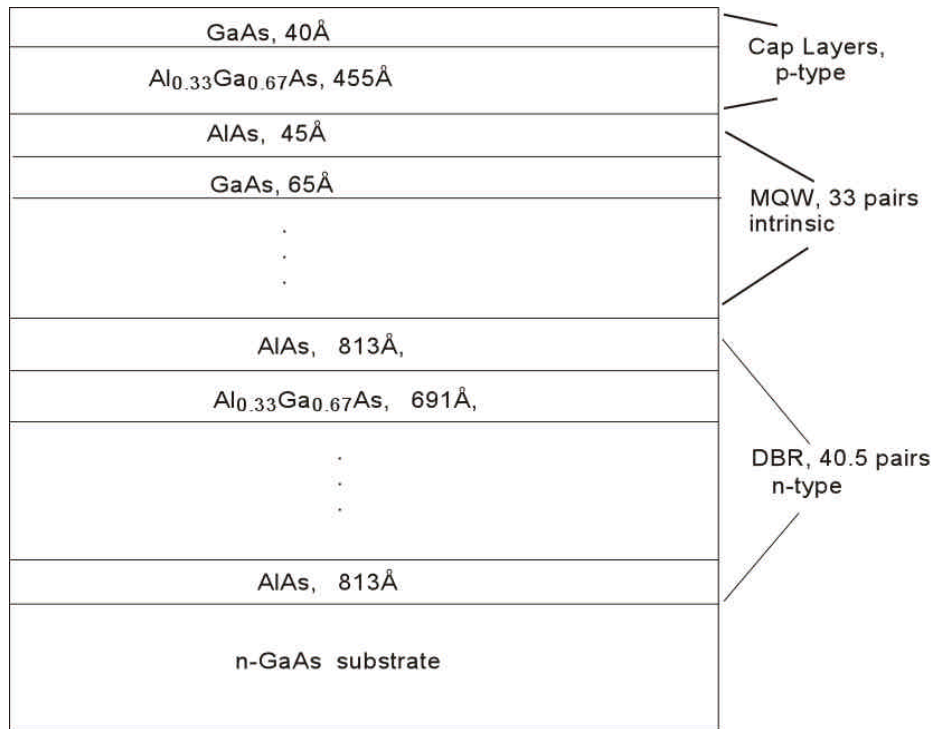


Fig. 5-5. The epitaxial structure of the MQW single mirror ARROW used in the modulator.

The epitaxial structure of the ARROW is shown in Fig. 5-5. In common with other QCSE devices, the MQW active region is located in the intrinsic region of a p-i-n diode structure so that when reverse biased, a large electric field can be applied with negligible current flow. The structure is capped by Al_{0.33}Ga_{0.67}As and GaAs p⁺ contact

layers (doped to 10^{19} cm^{-3}). The field-dependent absorption coefficient and refractive index for the MQW layer were calculated theoretically⁴⁹ and plotted in Fig. 5-6. We designed our phase-matched wavelength to be close to 840nm (for TE polarization), which is about 20nm longer than the heavy-hole exciton resonance wavelength, so that the propagation loss in the semiconductor waveguide is low enough for significant evanescent coupling to occur.

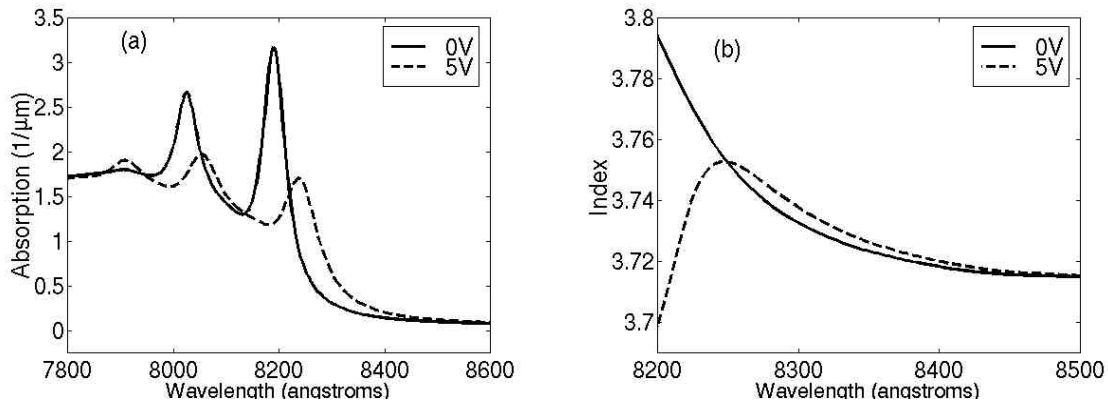


Fig. 5-6. The calculated TE absorption (a) and refractive index (b) values for the MQW in the modulator. At 0V, the built-in electric field of the device is 45kV/cm, and at 5V reverse bias, the electric field is 150kV/cm. The refractive index was calculated using the absorption data and the Kramers-Kronig relationship.

5.2.2 Experimental results and discussion

The processing procedures and testing experimental setup were identical to those used for the detector described in Chapter 4. The TE transmission spectra of several devices, measured with a HP70951A optical spectrum analyzer, are shown in Fig. 5-7. Due to thickness variations in MBE growth, the 0V phase-matched wavelength ranges from 827nm to 840nm, depending on the location of the device on the wafer. The quantum well absorption, however, is not nearly as sensitive to growth variations. A 2% thickness variation in a 65Å GaAs quantum well only leads to a 2nm change in the position of the first heavy hole exciton resonance. Therefore, essentially the same quantum well absorption and index values (Fig. 5-6) should apply for all three devices.

As the phase-matched wavelength of a device gets shorter, the resonance dip gets wider because of the increased quantum well absorption loss.

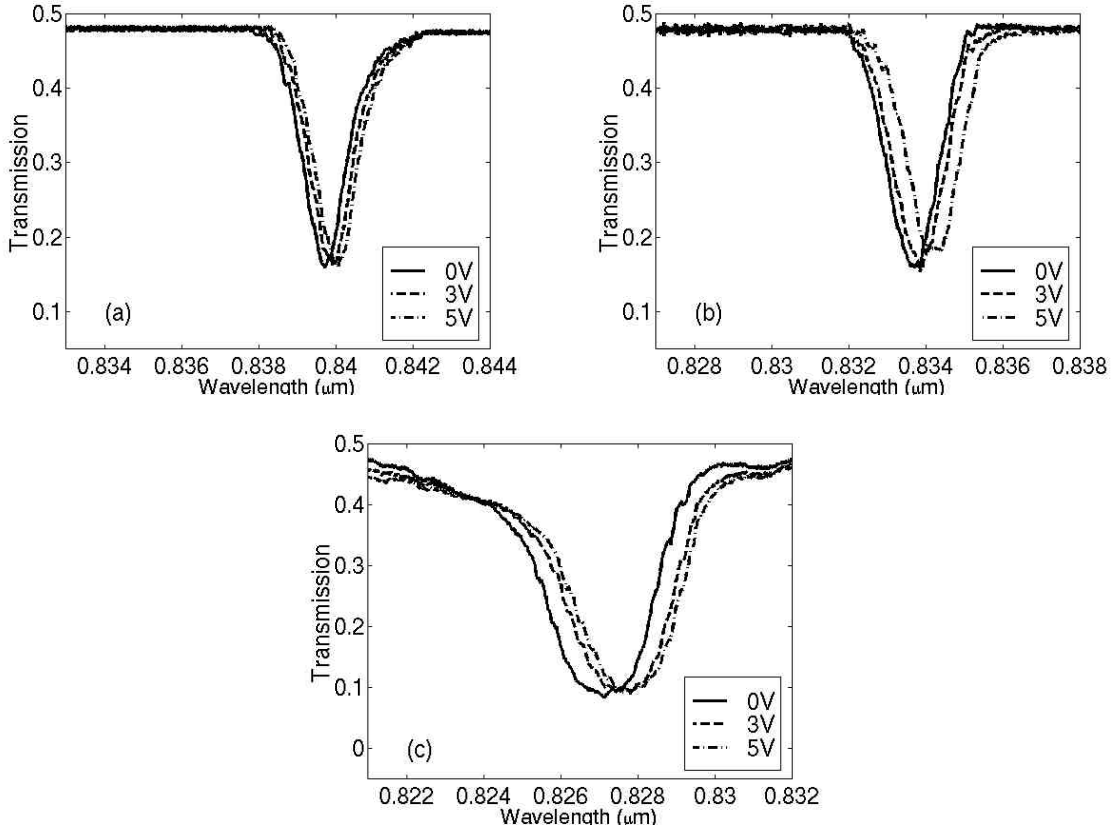


Fig. 5-7. The TE transmission spectra for: (a) device #1, which is near the center of the wafer; (b) device #2, which is halfway between the center and the edge of the wafer; (c) device #3, which is near the edge of the wafer.

When a vertical electric field is applied to the quantum wells, the real part of the refractive index increases and the phase-matched wavelength red-shifts. The amount of red-shift is smaller for devices with longer phase-matched wavelengths, which is qualitatively consistent with the index change shown in Fig. 5-6b. However quantitatively, the amount of the predicted red-shift ranges from 0.1nm to 0.2nm for a 5V swing, which is much smaller than the observed shift of 0.4nm to 0.8nm. This difference is caused by imperfections in the theoretical model used to calculate quantum well absorption. As is the case with most theoretical attempts at quantitatively characterizing the quantum confined Stark effect, the model can accurately predict the positions of the

excitonic resonances, but the Lorentzian lineshape assumed for the transitions is only approximate. Therefore, errors may result in the calculation for the refractive index. The goal of this experiment is to demonstrate modulation effects, hence knowing the position of the excitonic resonances in relationship to the phase-matched wavelength is of primary importance. In the future, photocurrent measurements⁴⁹ can be performed on separate quantum well samples to accurately measure the absorption constants in order to optimize the device design.

Device #3 shows a transmission change from 30% to 14% at 828.5nm with a 5V swing, corresponding to a modulation contrast (defined as $(T_H - T_L)/T_H$) of 53%. As in the previous devices, the off-resonance insertion loss of the device of about 3dB is due to poor fiber splicing. In all our devices, the application of more than 5 volts resulted in reverse breakdown. The electric field applied was only 150kV/cm, which is significantly smaller than the reported breakdown field in GaAs (about 400kV/cm).⁴⁴ There could be two possible mechanisms for the premature breakdown: material defects and electron tunneling through the relatively thin p-type contact layers (Fig. 5-8).

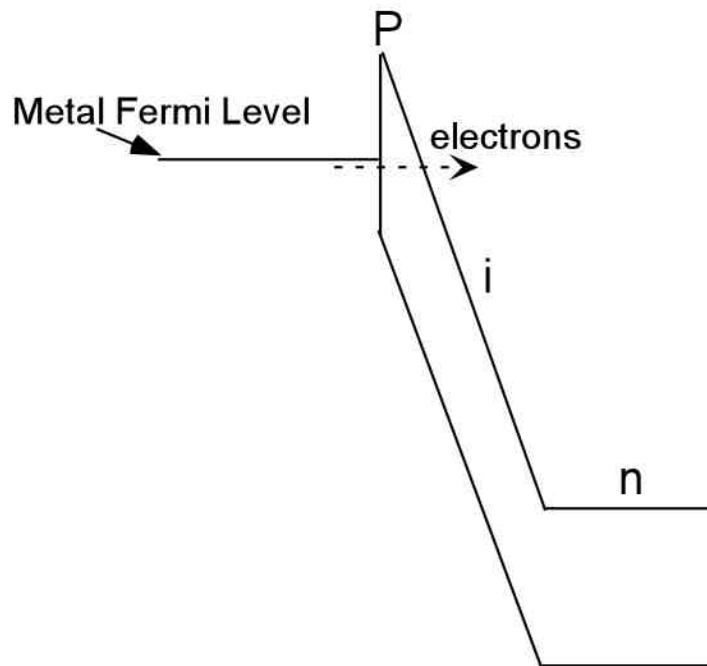


Fig. 5-8. The band diagram of a reverse-biased p-i-n junction. The thin p-type contact layers can be completely depleted at high biases, therefore electrons can tunnel from the metal contact to the intrinsic region, causing junction breakdown.

5.3 Modulator with double-mirror ARROW

5.3.1 Device design

To reduce the electron tunneling current, a thicker p-doped region is required. Instead of simply increasing the thickness of the contact layer, a partially reflective p-type DBR mirror can be used to ensure that most of the optical field remains confined in the MQW region, and that part of it leaks into the fiber cladding. In such a device, when the wafer is attached to the side-polished single mode fiber, waveguiding is achieved in the MQW core by reflection from the n-type DBR on the one side, and a combination of reflection from the p-type DBR and total internal reflection from the fiber cladding on the other side (similar to the detector described in chapter 4).

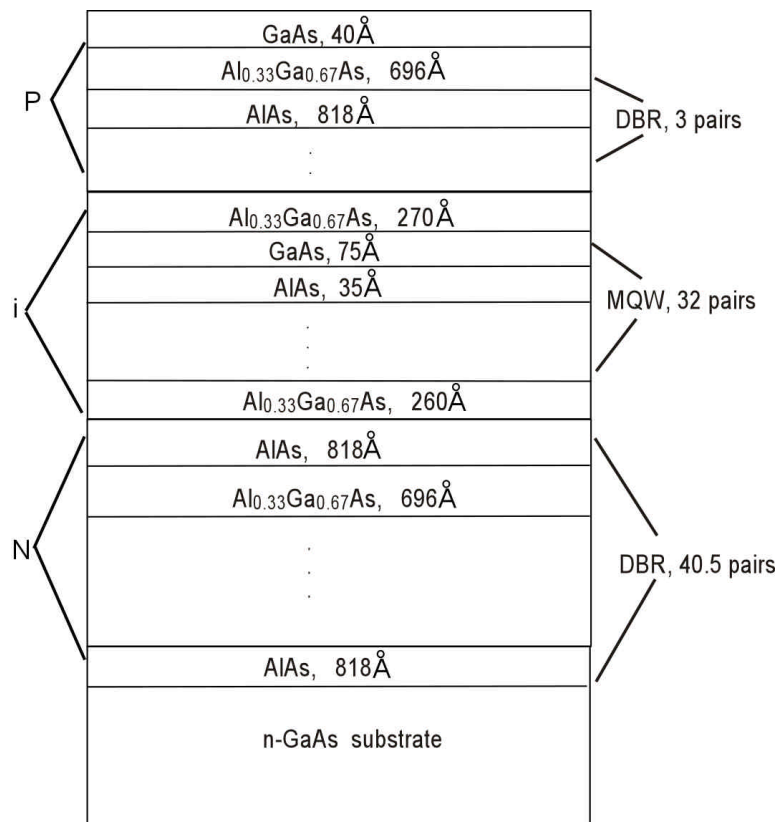


Fig. 5-9. The detailed epitaxial structure of the double mirror ARROW structure. The intrinsic MQW core region is surrounded by a highly reflective DBR (n-doped) and a leaky DBR (p-doped).

The epitaxial structure of the ARROW is shown in Fig. 5-9. The doping concentrations are $1\times 10^{19} \text{ cm}^{-3}$ for the p-type layers and $1\times 10^{18} \text{ cm}^{-3}$ for the n-type layers. The experimentally determined field-dependent absorption coefficients and the calculated refractive indices for the quantum wells used in the ARROW are shown in Fig. 5-3 and Fig. 5-4 respectively. A 40kV/cm field corresponds to the built-in field of our diode structure. The designed phase-matched wavelength of the device is 855nm (for TE polarization), which is about 25nm longer than the first heavy-hole exciton resonance wavelength under zero bias. As in the modulator described in section 5.2, this is to ensure that the propagation loss in the ARROW is low enough for significant evanescent coupling to occur. The calculated effective indices for the ARROW and the fiber are shown in Fig. 5-10.

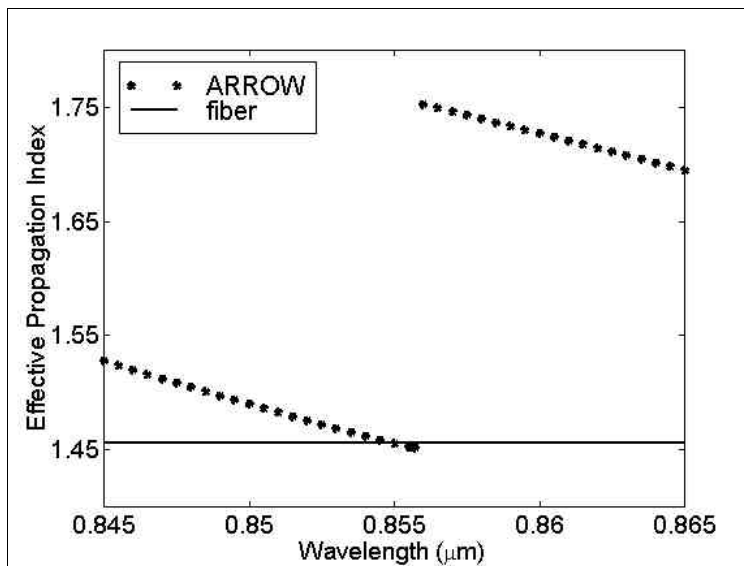


Fig. 5-10. The calculated TE effective propagation indices for the ARROW and the fiber. The ARROW mode is the highest order confined mode.

5.3.2 Experimental results

The TE transmission spectra of a typical device are shown in Fig. 5-11a. Due to thickness variations in MBE growth, the 0V phase-matched wavelength is 845.5nm instead of the designed 855nm. The off-resonance insertion loss of our device is about 3dB, which, as before, can be attributed to poor fiber splicing. As the applied bias is increased from zero, the real part of the MQW refractive index increases, resulting

initially in a red-shift of the phase-matched wavelength. When the bias is large enough such that the first heavy-hole excitonic resonance coincides with the 0V phase-matched wavelength, the absorption in the MQW at that wavelength quenches the transmission dip. The maximum modulation contrast occurs at 845.5nm, where the device transmission changes from 10% to 40% with a 9V swing. As shown in Fig. 5-11b, the modulator has an essentially linear voltage-dependent transmission within certain voltage ranges (such as from 3 to 4.5V, or 6.5 to 7.5V), which lends itself for potential analog applications. The 4:1 on/off ratio at the 0V resonant wavelength also makes it attractive for digital or switching applications. In addition, compared with conventional electro-absorption modulators, this device is more suited for high-power applications because at the high-absorption state of the MQW, most of the light stays in the fiber and very few carriers are generated in the ARROW.

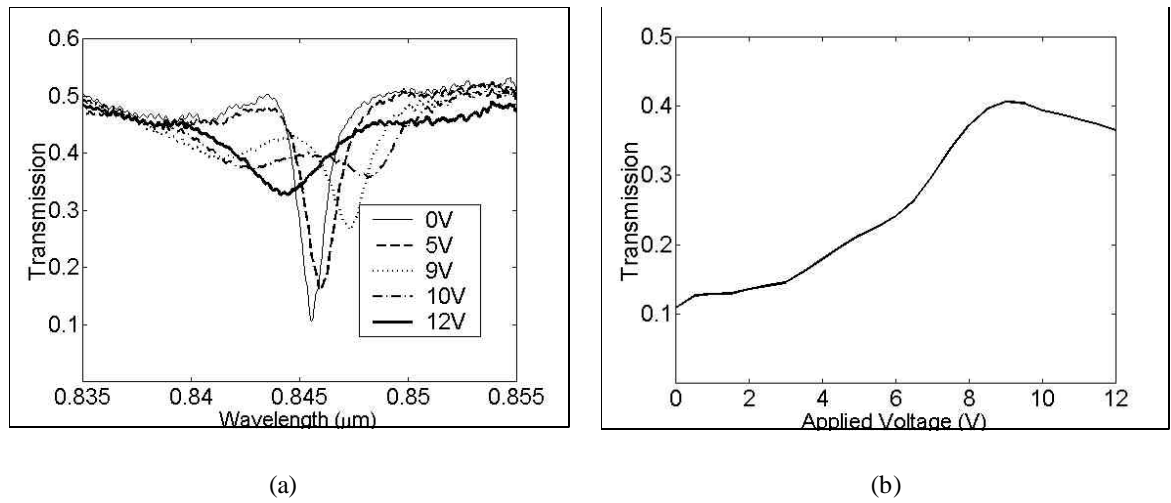


Fig. 5-11. (a) The transmission spectra of the modulator under different bias conditions. (b) Transmission at 845.5nm as a function of applied bias.

5.3.3 Discussion

The appearance of multiple dips in the transmission curves can be explained by the wavelength-dependent absorption coefficients of the MQW. When there is a variation in the MQW absorption (and thus, ARROW propagation loss) near the phase-matched wavelength, the shape of the transmission curve is no longer a simple dip. This behavior is illustrated in Fig. 5-12, where the transmission spectra are calculated by solving the

coupled mode equations (equation 3-6) with assumed ARROW loss spectra, which are roughly based on the MQW absorption data shown in Fig. 5-3.

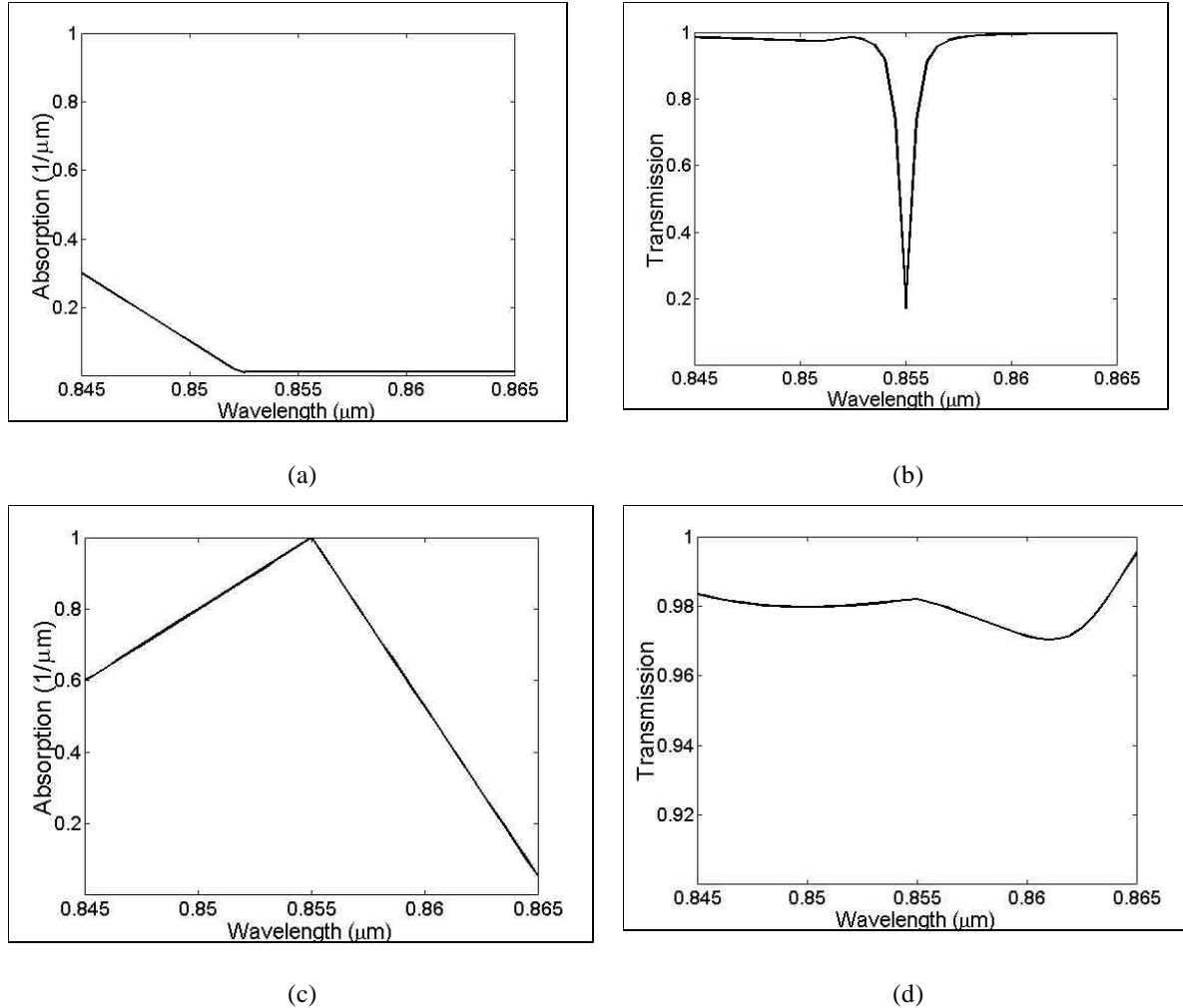


Fig. 5-12. An illustration of the “double-dip” effect in the experimental transmission spectra: (a) and (c) are the assumed wavelength-dependent ARROW propagation loss at two different biases; (b) and (d) show the corresponding transmission spectra calculated with the coupled-mode equations and the dispersion relations shown in Fig. 5-10. The assumed coupling coefficient is 3mm^{-1} , and the interaction length is 1mm.

With the development of silicon V-groove technology, fiber half couplers with arbitrary interaction lengths and polishing depths can be realized. The increase in the interaction length will lead to devices with much larger on/off ratios. As shown in Fig. 5-13, a 5mm long device with otherwise identical parameters as the one in Fig. 5-12, has a calculated on/off ratio of more than 40dB (10000:1).

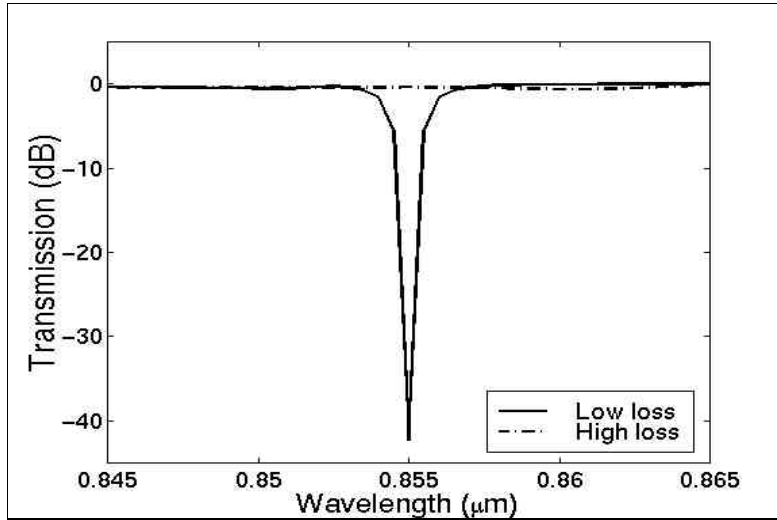


Fig. 5-13. The transmission spectra of a 5mm long in-line modulator, as calculated with the coupled-mode equations. The low- and high-loss cases correspond to the ARROW absorption curves shown in Fig. 5-12a and 5-12c.

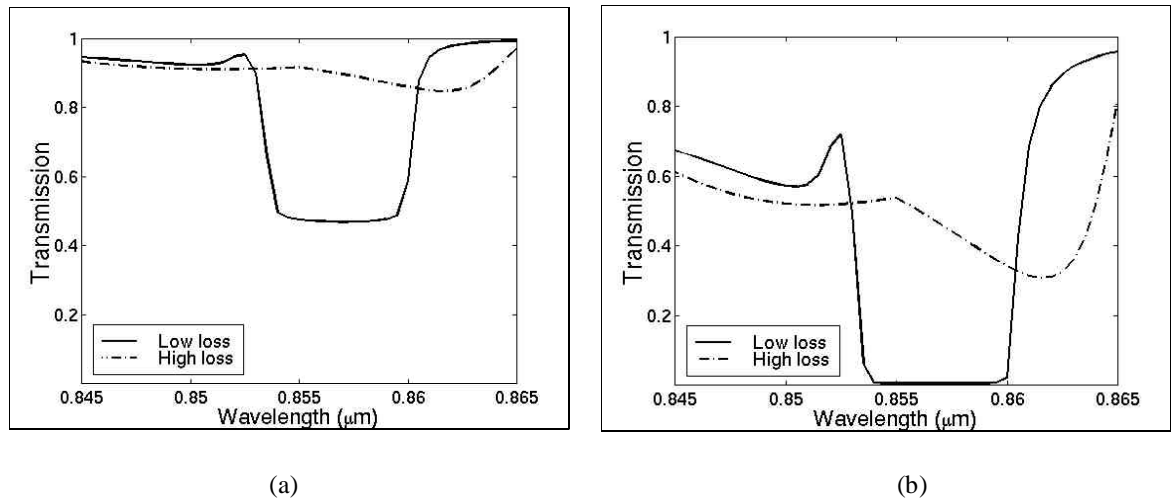


Fig. 5-14. The calculated transmission spectra of an in-line modulator with a tapered ARROW. The coupling coefficient is 3mm^{-1} for (a) and 8mm^{-1} for (b).

The useful linewidth of our device is about 1nm, which is ultimately limited by the width of the resonance dip itself. With a longer half coupler and a tapered ARROW,¹⁷ above the linewidth can be extended. As shown by the calculated transmission spectra in Fig. 5-14, a 5nm linewidth is achievable with a 5mm long device with a 0.5% taper. The main drawback with using a tapered structure is the tradeoff between insertion loss and on/off ratio. In a tapered device, the effective interaction

length for a given wavelength is smaller than that of a normal device of the same total length. Therefore a larger coupling coefficient is needed to obtain a certain on/off ratio, which in turn causes the transmission of the “on” state (high loss state in the ARROW) to decrease. This situation is also illustrated in Fig. 5-14.

5.4 Simulation of traveling wave modulators

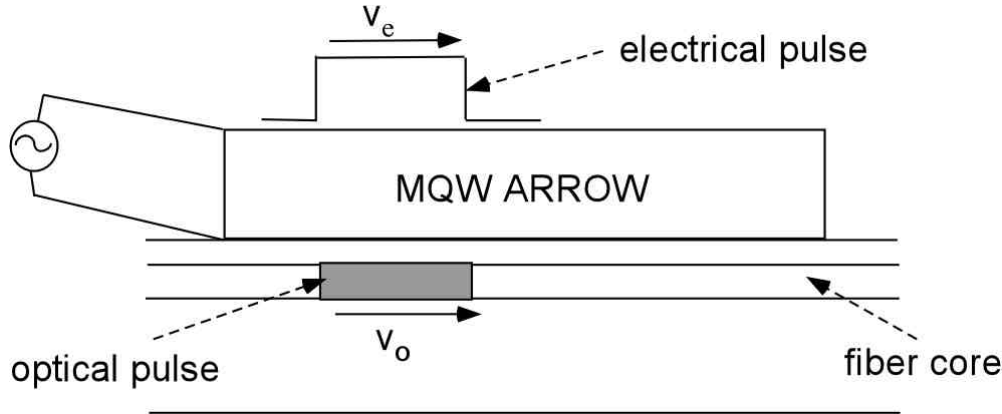


Fig. 5-15. The concept of a traveling wave modulator: the modulation signal (electrical) travels at the same speed as the modulated signal (optical).

The speed of our lumped-element device is limited by its RC time constant. The capacitance of the device can be estimated as

$$C = \frac{\epsilon_r \epsilon_0 A}{d}, \quad (5-14)$$

where ϵ_r is the relative permittivity of GaAs, ϵ_0 is the free space permittivity, A is the area of the device and d is the thickness of the intrinsic region. The smallest possible device area is determined by the size of the fiber core and the interaction length. With a 1mm interaction length and a $5\mu\text{m}$ fiber core diameter, $A = 1\text{mm} \times 5\mu\text{m}$, $\epsilon_r = 13$, and $d = 0.4\mu\text{m}$, the minimum capacitance is about 1.5pF. Ignoring other resistances, and with a microwave source impedance of 50Ω , the RC time constant is 75ps, which means a bandwidth of about 13GHz. The practical limit, however, is expected to be much lower than this, mainly due to parasitics as well as transmission line effects which can be appreciable at these dimensions (with a microwave propagation index of 10, a 13GHz

signal has a wavelength of 2mm in the medium). In order to increase the operating speed, a traveling wave electrode design is needed.^{50,51} In this case, when a voltage pulse is applied to the ARROW, it travels along the waveguide, together with the optical signal (Fig. 5-15). When the propagating velocities of the two signals are matched and when the voltage pulse travels without loss, the device will have no bandwidth limitations.

5.4.1 Transmission line basics

The requirement for a successful traveling wave device design is, therefore, to create a microwave electrode structure on the ARROW, such that there is no difference between the microwave and optical propagation velocities and the microwave propagation loss is minimized. Here the microwave velocity refers to the phase velocity, while the optical velocity refers to the group velocity in the fiber (effective index = 1.45).

The simplest transmission line design on a p-i-n diode is the parallel-plate structure shown in Fig. 5-16a. The line capacitance and inductance (per unit length) are given by⁵²

$$C = \epsilon_r \epsilon_0 w / d, \quad (5-15)$$

$$L = \mu_0 D / w, \quad (5-16)$$

where ϵ_r is the relative permittivity of the material, and w , d and D are defined in Fig. 5-16a. For a standard lossless transmission line, the electrical phase velocity and the characteristic impedance can be expressed as

$$v_\mu = 1/\sqrt{LC} = \sqrt{d/(\epsilon_r \epsilon_0 \mu_0 D)}, \quad (5-17)$$

$$Z_0 = \sqrt{L/C} = w^{-1} \sqrt{\mu_0 D d / (\epsilon_r \epsilon_0)}. \quad (5-18)$$

In a device utilizing the QCSE, the intrinsic region thickness d is usually no more than 1μm in order to limit the operating voltage. Therefore with $D \gg d$, the velocity and the impedance are much smaller than what they would be for a parallel-plate structure homogeneously filled with dielectric. From (5-17), the effective microwave index can be derived:

$$n_\mu = \sqrt{\epsilon_r} \sqrt{D/d} = n_{mat} \sqrt{D/d}, \quad (5-19)$$

where n_{mat} is the material index. With $n_{mat} \approx 3.6$, it is impossible to design a parallel-plate structure on GaAs in which the microwave phase velocity can be matched to the optical signal velocity in the fiber. This situation, which is referred to as the slow-wave effect,^{53,54} can be alleviated by using a planar microstrip (PMS) structure shown in Fig. 5-16b. Even in this case, because the magnetic field extends into the doped regions, the lower limit on the microwave propagation index is still imposed by the material index.

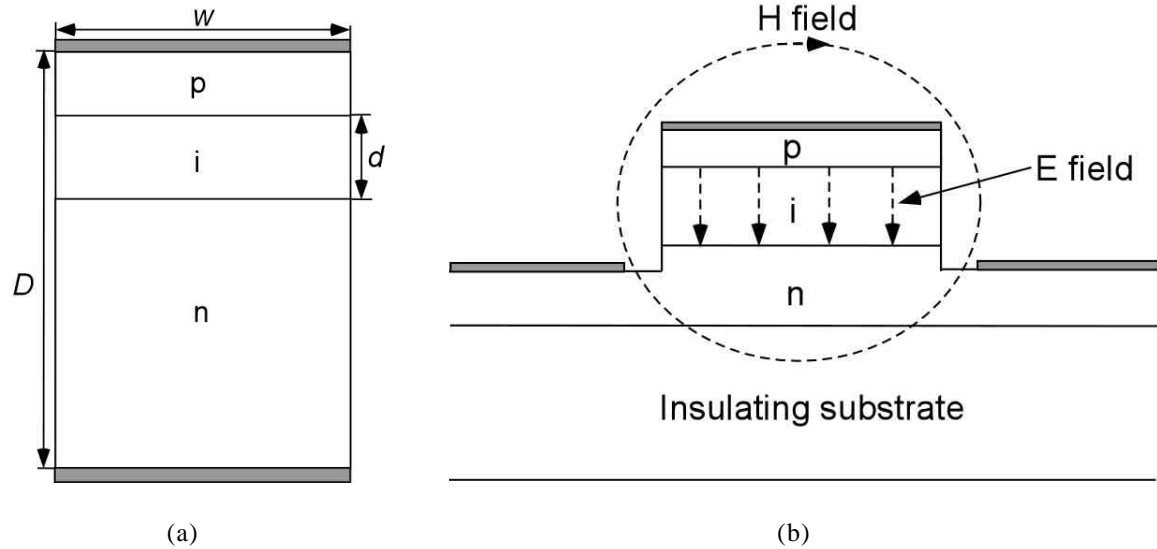


Fig. 5-16 (a) A parallel plate transmission line; (b) A planar microstrip transmission line.

The microwave propagation loss mainly comes from conduction losses in the metal electrodes as well as the doped layers. For the PMS structure (Fig. 5-16b), the metal loss is dominated by the center electrode (signal) because of the high current density it carries. The side electrodes (ground) are usually much wider, hence the current density and the loss are much lower. The attenuation due to metal loss can be expressed as⁵²

$$\alpha_{metal} = \frac{R_s}{wZ_0}, \quad (5-20)$$

where R_s is the skin effect surface resistivity of the metal, w is the electrode width and Z_0 is the characteristic impedance of the transmission line. It is clear that increasing the

electrode width will reduce the attenuation. The surface resistivity is closely related to the penetration depth of the metal, which is expressed as

$$\delta = \frac{1}{\sqrt{\pi f \mu_0 \sigma}}, \quad (5-21)$$

where f is the frequency and σ is the conductivity. For a thick metal (thickness $t > 3\delta$), the surface resistivity is given by

$$R_s = \frac{1}{\sigma \delta}, \quad (5-22)$$

and for a thin metal,⁵⁵

$$R_s \approx \frac{1}{\delta \sigma} \left[\frac{\sinh(2t/\delta) + \sin(2t/\delta)}{\cosh(2t/\delta) - \cos(2t/\delta)} \right]. \quad (5-23)$$

In either case, in order to have a small R_s , the electrode has to be very conductive as well as thick.

The propagation loss caused by the doped layers comes from capacitive currents and induction currents. The capacitive current is the current that charges the p-i-n capacitor. For the structure shown in Fig. 5-16b, because of the finite conductivity of the n-type layer, a resistive loss is incurred when the carriers travel from underneath the center conductor to the side conductors. To reduce this loss, a thicker n-type layer with a higher doping level (i.e., higher conductivity) is needed. The induction current is the current induced by the alternating magnetic field in the doped layer. According to Faraday's law, an alternating magnetic field induces an electric field, which in the presence of a conductive material, produces a current. To reduce this current, the n-type layer needs to be as thin and as resistive as possible. Therefore, a careful choice for the thickness and the doping level of the n-type layer has to be made, so that the combined effect of these two loss mechanisms can be minimized.

5.4.2. Electrode design

A traveling wave electrode design, taking into account such practical considerations as processing constraints and sufficient space for the fiber interface, is shown in Fig. 5-17. The roughly optimized numerical values for the dimensions are:

$w = 3\mu m$, $t = 1\mu m$, $s = 9\mu m$, $a = 2\mu m$, $h = 1\mu m$, $g = 3\mu m$, $d_p = 0.15\mu m$, and $d_n = 2\mu m$.

The contact metal is gold, with a conductivity of $4.4 \times 10^7 S/m$. The doping levels for the n-type and p-type DBRs are $1 \times 10^{18} cm^{-3}$ ($\sigma_n \approx 5 \times 10^4 S/m$) and $1 \times 10^{19} cm^{-3}$ ($\sigma_p \approx 1 \times 10^4 S/m$), respectively. The one major difference between this structure and the structure shown in Fig. 5-16b is that the center conductor is divided into two parts, leaving a slot in the middle for fiber access.

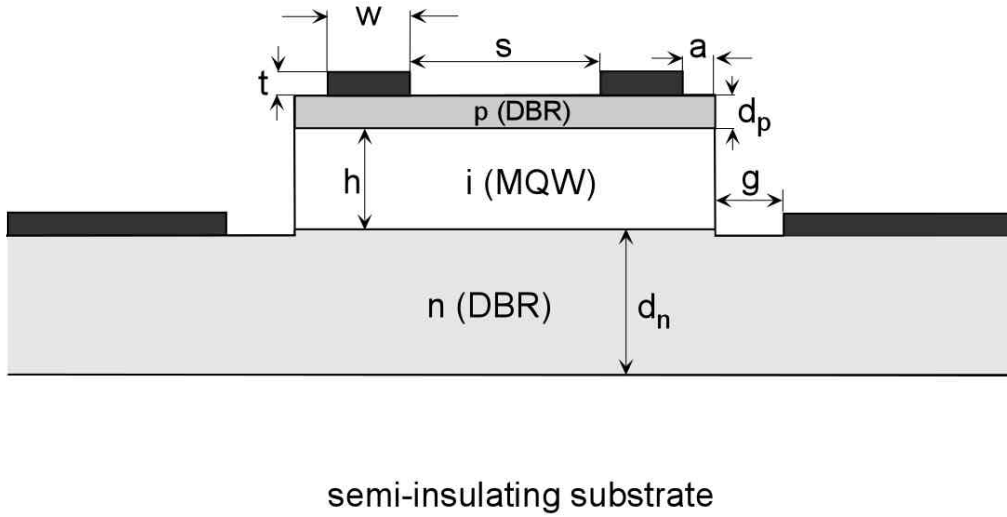


Fig. 5-17. The cross-sectional view of a traveling wave electrode design for an in-line fiber modulator.

The propagation characteristics (propagation index, loss and impedance) of the transmission line are calculated using the HP Momentum package within the Hewlett Packard Advanced Design System (HPADS, version 1.1). The software is based on a numerical discretization technique called the method of moments,⁵⁶ which is used to solve Maxwell's equations for planar multi-layer dielectric structures. The output of the program is in terms of the S-parameters of the transmission line, which can then be converted into propagation parameters using the formulae provided by Eisentadt and Eo.⁵⁷

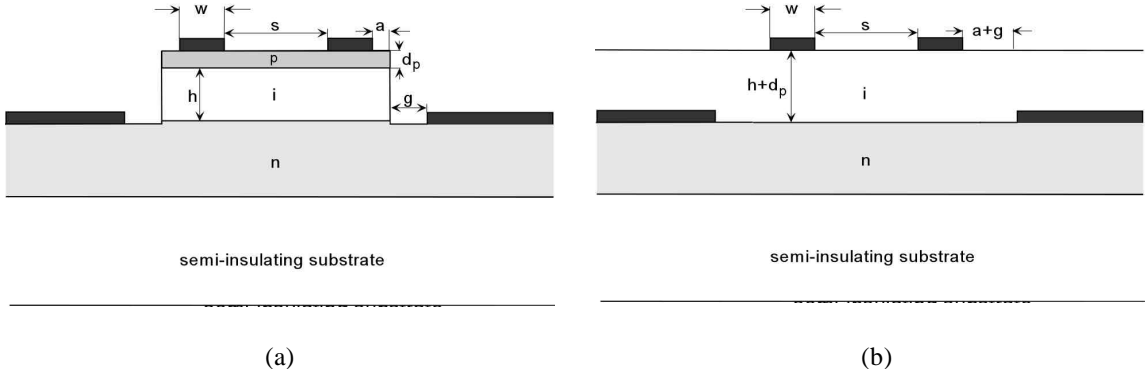


Fig. 5-18. (a) The actual transmission line structure; (b) The model used for HP Momentum calculation.

Because HP Momentum only handles planar dielectric structures, the device schematic shown in Fig. 5-17 has to ‘planarized’ before running the simulation (Fig. 5-18). The p-type layer is omitted in the model because its inclusion would result in gross over-estimation of the unit length capacitance of the device, therefore affecting the calculation of the impedance and the effective index. To correct for this omission, the extra capacitance and loss caused by the p-type layer are added manually after the simulation.

The overall capacitance per unit length of the transmission line can be approximated as

$$C_{tot} = C_{cal} \left(\frac{h + d_p}{h} \right) + \frac{\epsilon_r \epsilon_0 (s + 2a)}{h}, \quad (5-24)$$

where C_{cal} is the capacitance calculated by HP Momentum. Due to the small dimensions of the p-type layer, the loss caused by induction currents is expected to be negligible, while the capacitive current loss dominates. The attenuation coefficient can be derived from first principles (see Appendix A) and written as

$$\alpha = Z_0 R_s (\pi f C_{tot})^2 \left[\frac{1 - \exp(-s\sqrt{C_s \pi f R_s})}{2\sqrt{C_s \pi f R_s}} \right], \quad (5-25)$$

where Z_0 is the transmission line characteristic impedance, $R_s = 1/(\sigma_p d_p)$ is the sheet resistance of the p-type layer, $C_s = \epsilon_r \epsilon_0 / h$ is the device capacitance per unit area and f is the signal frequency.

Despite the many approximations used in the calculation, this method is able to yield results that are consistent with published experimental data (see Appendix B). In Fig. 5-19, the calculated values for the attenuation coefficient, the characteristic impedance and the effective index are plotted as functions of frequency.

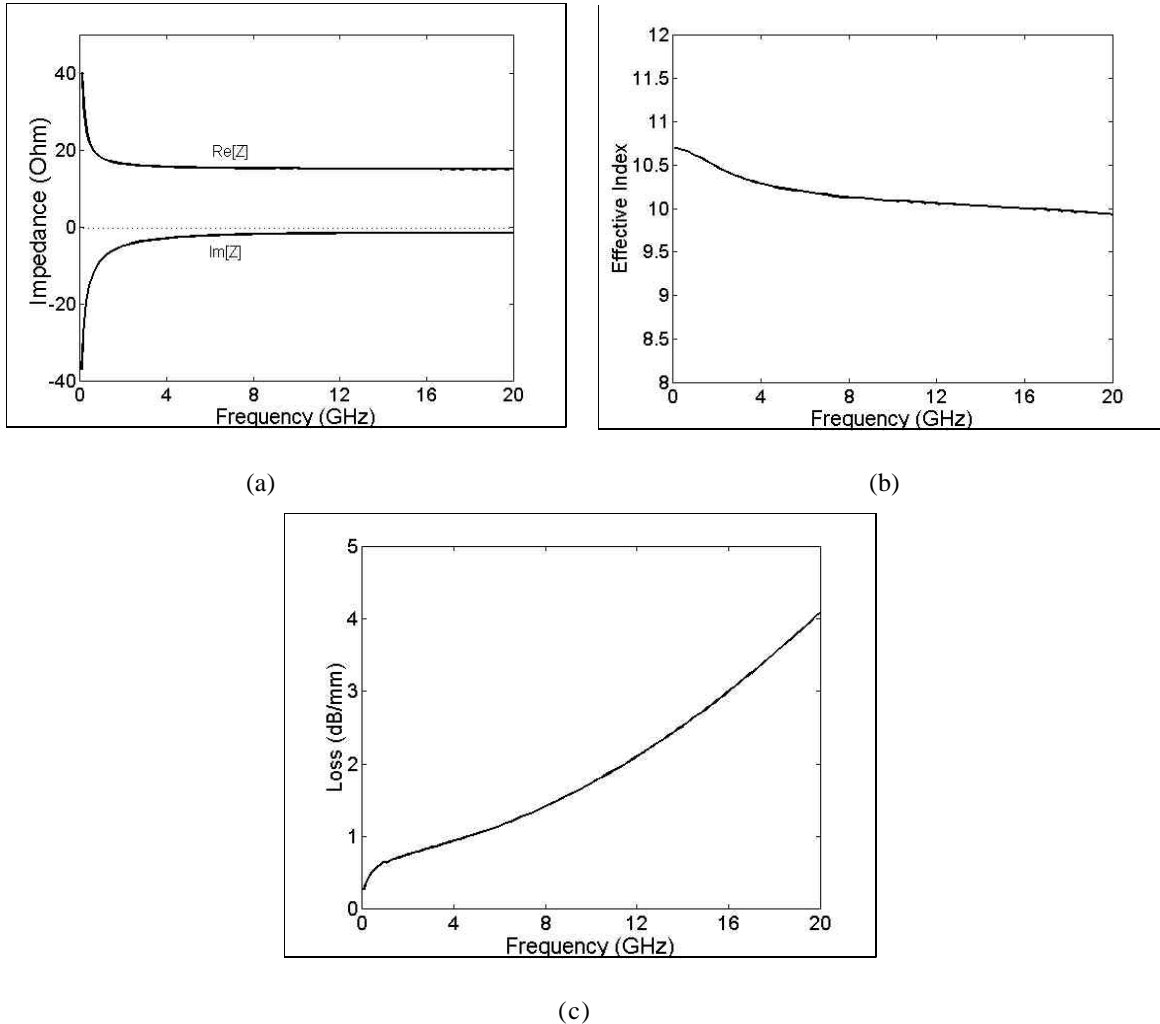


Fig. 5-19. The calculated characteristic impedance (a), effective propagation index (b), and the attenuation coefficient (c) of the traveling wave electrode structure shown in Fig. 5-17.

5.4.3 Frequency response

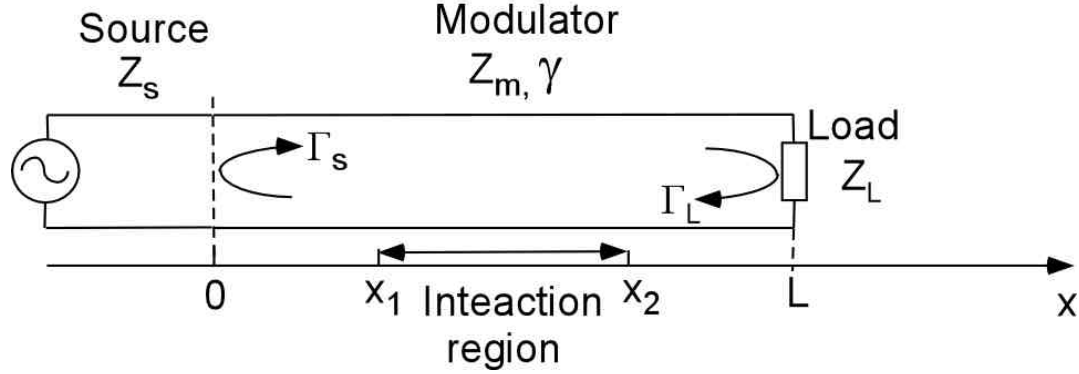


Fig. 5-20. The transmission line model used to calculate the modulator frequency response.

Assuming that the modulator is linear, then its optical response, R , will be proportional to the “accumulation” of the modulation voltage V_m along the device,

$$R \propto \text{Max} \left\{ \left| \int_{x_1}^{x_2} V_m(x, \phi) dx \right| \right\}, \quad (5-26)$$

where x_1 and x_2 are the boundaries of the interaction region, ϕ is a phase variable. By varying the value of ϕ from 0 to 2π , a maximum value of the integral can be obtained, which corresponds to the device response. Using the model shown in Fig. 5-20, and taking into account multiple microwave reflections inside the modulator, V_m can be expressed as⁵⁸

$$V_m(x, t, \phi) = \text{Re} \left[\frac{V_0 T \{ \exp(-\gamma x) + \Gamma_L \exp(\gamma x - 2\gamma L) \} \exp(j\omega t + \phi)}{1 - \Gamma_s \Gamma_m \exp(-2\gamma L)} \right], \quad (5-27)$$

where V_0 is microwave source voltage, T is the transmission coefficient from the source to the modulator, Γ_s and Γ_L are the reflection coefficients at the source and the load, respectively, γ is the complex microwave propagation coefficient, and ω is the microwave frequency. In terms of the impedances, the expressions for the T , Γ_s and Γ_L are

$$T = \frac{2Z_m}{Z_m + Z_s}, \quad (5-28)$$

$$\Gamma_s = \frac{Z_s - Z_m}{Z_s + Z_m}, \quad (5-29)$$

$$\Gamma_L = \frac{Z_L - Z_m}{Z_L + Z_m}. \quad (5-30)$$

The complex propagation coefficient γ is given by,

$$\gamma = \alpha_\mu + j \frac{\omega}{v_\mu}, \quad (5-31)$$

where α_μ is the microwave attenuation and v_μ is the microwave phase velocity.

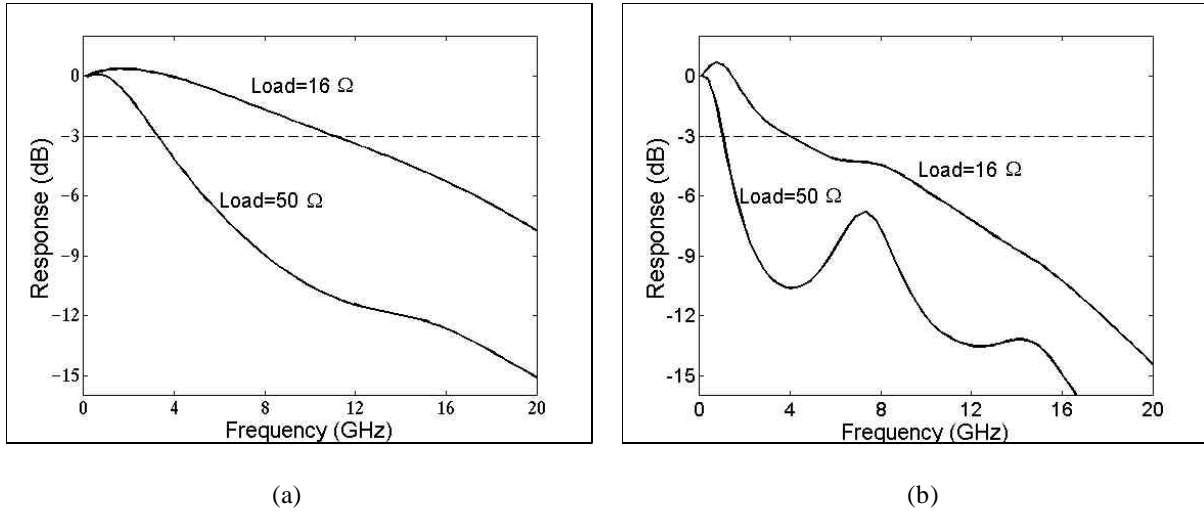


Fig. 5-21. The calculated frequency responses for 1mm long devices (a) with only a fiber, and (b) with a fiber block.

When an optical pulse starts to propagate with optical group velocity v_0 at $t=0$ and $x=0$, it reaches position x at $t = x/v_0$, at which point the modulation voltage it sees is $V_m(x, \phi) = V_m(x, t = x/v_0, \phi)$. Therefore the modulator response can be expressed as

$$R \propto \text{Max} \left\{ \left| \int_{x_1}^{x_2} V_m(x, t = x/v_0, \phi) dx \right| \right\}. \quad (5-32)$$

In an ideal traveling wave modulator, $\alpha_\mu = 0$, $v_0 = v_\mu$, $\Gamma_s = \Gamma_L = 0$, and $T=1$, so

$V_m(x, t, \phi) = V_0 \cos \phi$ and $R \propto |V_0(x_2 - x_1)|$ (obviously the integral reaches its maximum

value when $\phi = 0$). As the situation deviates from the ideal case, the modulation voltage seen by the optical pulse becomes position dependant and the response decays.

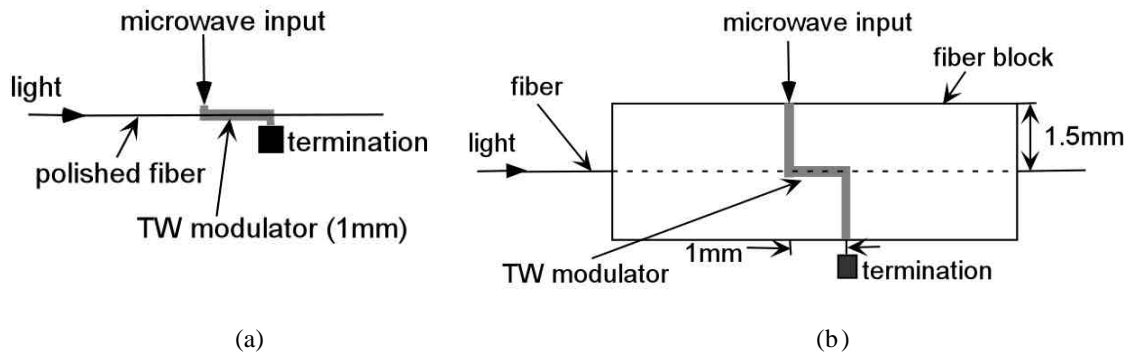


Fig. 5-22. Top view of microwave probing arrangements: (a) with only a fiber where no extra sections of transmission line are needed for microwave input and termination; (b) with a fiber block where extra sections are needed to connect the microwave input and termination to the polished interaction region.

In Fig. 5-21, the calculated frequency responses for a 1mm long device are plotted. When the load impedance (50Ω) is different from the characteristic impedance of the transmission line ($\sim 16\Omega$), a standing wave pattern is created along the interaction region, which degrades the frequency response and lowers the device bandwidth. If during testing, a polished fiber embedded in a fiber block is used (Fig. 5-22b), then additional sections of transmission line are needed to connect the microwave input and termination probes, which leads to higher losses as well as a more pronounced standing wave effect. Therefore by using a smaller fiber block, or better yet, by not using any fiber block at all (i.e., $x_1 = 0$ and $x_2 = L$, using the notation of Fig. 5-20), the device bandwidth can be extended. By the same token, reducing the interaction region length will also increase the bandwidth. Fig. 5-23 shows that a 0.5mm device has a 3dB bandwidth of greater than 20GHz compared with 11GHz for a 1mm device. The drawback, though, is that a shorter device will have a lower modulation contrast (section 5.3.3).

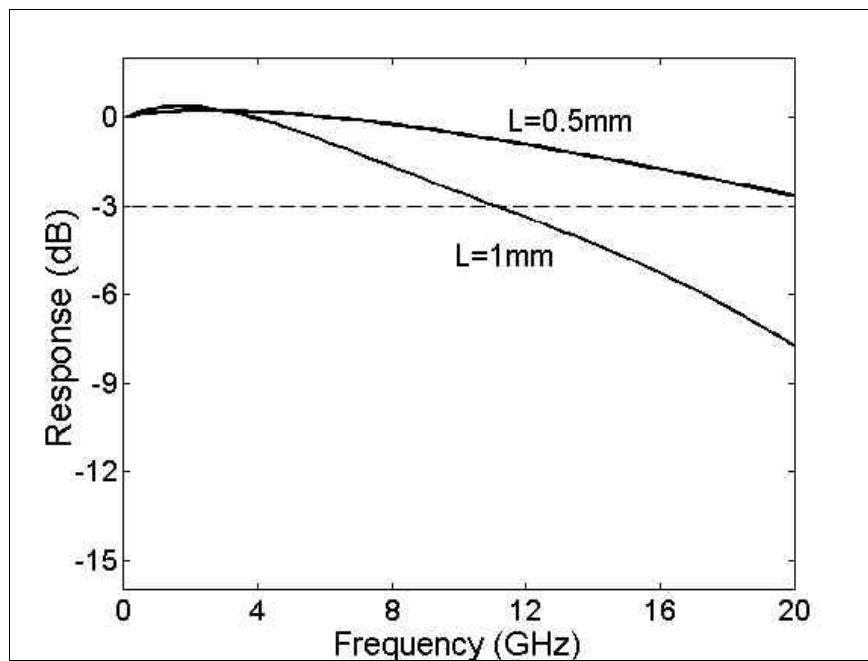


Fig. 5-23. The calculated frequency responses for devices with different interaction lengths, assuming that no fiber block is used.

Chapter 6

In-line fiber light emitter

All devices described so far operate via the coupling of light from the fiber into the ARROW. A coupled waveguide system, upon whose physics all these devices are based, however, is by no means a “one-way street” (i.e., light can travel the other way too). In fact, if the ARROW can be made to generate light or provide optical gain, the ARROW-fiber coupled waveguide structure could become a new device paradigm for fiber-coupled narrowband optical communication sources or in-line fiber optical amplifiers. In this chapter, a proof-of-concept in-line fiber light emitter is presented.

6.1 Device design and experiment

The epitaxial structure used for this experiment is the same as that of the detector (Fig. 4-9). By forward biasing the p-i-n diode, electrons and holes are injected into the intrinsic region and most of them recombine in the quantum well, creating photons. The photons are emitted into multiple modes, and only those that are phase-matched to the fiber mode are coupled into the fiber. Therefore, a narrowband output from the fiber is expected.

After the wafer was grown, proton implantation, which converts doped layers into highly resistive layers by creating defects that trap electrons and holes,^{59,60} was performed as the first processing step to provide electrical isolation and current confinement. The proton doses and energies used are: $4 \times 10^{15} \text{ cm}^{-2}$ at 10keV, $5.01 \times 10^{15} \text{ cm}^{-2}$ at 26keV, $3.33 \times 10^{15} \text{ cm}^{-2}$ at 36keV, and $1.67 \times 10^{16} \text{ cm}^{-2}$ at 50keV. These numbers were chosen based on the TRIM Monte-Carlo ion-implantation simulation,⁶¹ with the criterion that a proton damage density of about 30 times the dopant density is needed for proper isolation.⁶² As a result of these implantation steps, the p-type mirror was rendered

electrically insulating and current injection only occurs at regions in the vicinity of the fiber core (Fig. 6-1), thus the efficiency of the device can be improved. The processing and testing steps that followed were the same as those used for the detector (section 4.3.2), with the exception that the ARROW was forward biased. The optical output in the fiber was observed with an optical spectrum analyzer.

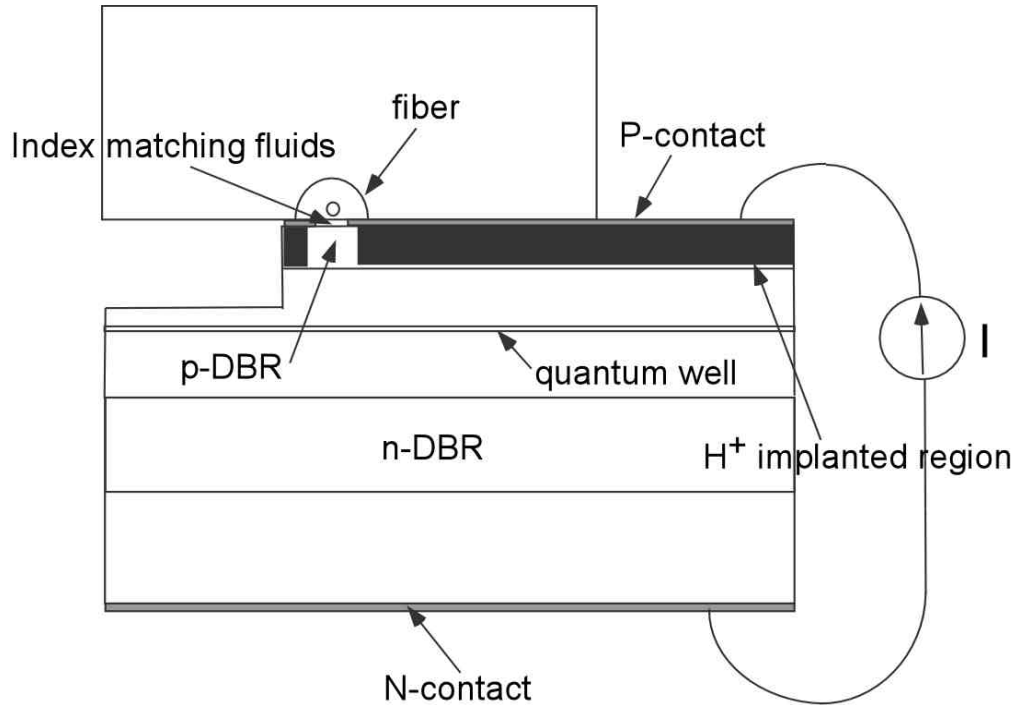


Fig. 6-1. The cross-sectional view of the light-emitting device testing arrangement.

6.2 Results and discussion

The observed output spectra as a function of injection currents is shown in Fig. 6-2. The two groups of emission peaks correspond to TE and TM resonances. The TE resonances have narrower linewidths mainly because of the higher reflectivity of the DBR mirrors, and hence lower ARROW propagation losses. The total output power measured with an optical power meter was about 7nW for an injection current of 100mA. This amount of current results in the injection of about 10^{18} electron-hole pairs per second, which ideally would create an equal number of photons per second. At the photon energy of 1.5eV ($\sim 830\text{nm}$), 10^{18} photons per second corresponds to a power of about 200mW. Therefore, discounting any non-radiative recombination, the emission

efficiency, which is defined as the ratio of the number of photons detected in the fiber to the number of photons generated in the ARROW, could be as low as 3×10^{-8} .

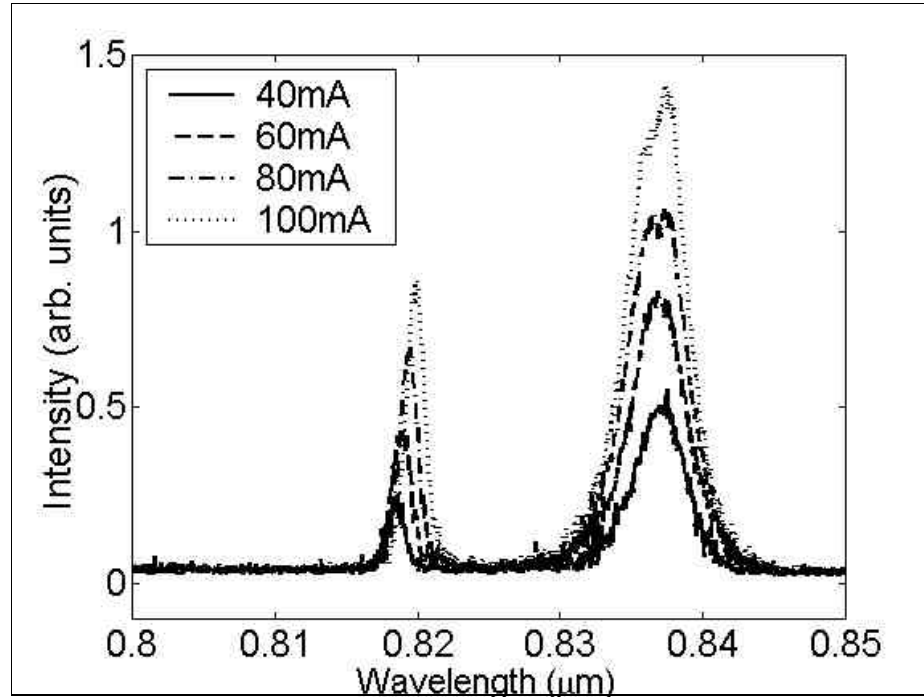


Fig. 6-2. The measured emission spectra as a function of injection currents.

This low efficiency is not surprising since there is no lateral optical confinement defined in the ARROW. Therefore photons can be emitted at angles that are not collinear with the fiber. By lithographically defining a lateral waveguide (such as the configuration shown in Fig. 4-8), the two-dimensional photonic density of states can be reduced to a one-dimensional one, and the number of modes into which photons can be spontaneously emitted is further restricted. However, as with other microcavity devices, there is always the challenge of reducing dimensions without increasing surface trap states which can lead to non-radiative recombination.

The change in the device transmission characteristics under current injection is of interest because if there are enough carriers in the ARROW core to provide optical gain, it is entirely possible for the light wave traveling in the fiber to be amplified (Fig. 6-3). Therefore this device structure might prove useful as an in-line fiber semiconductor amplifier.

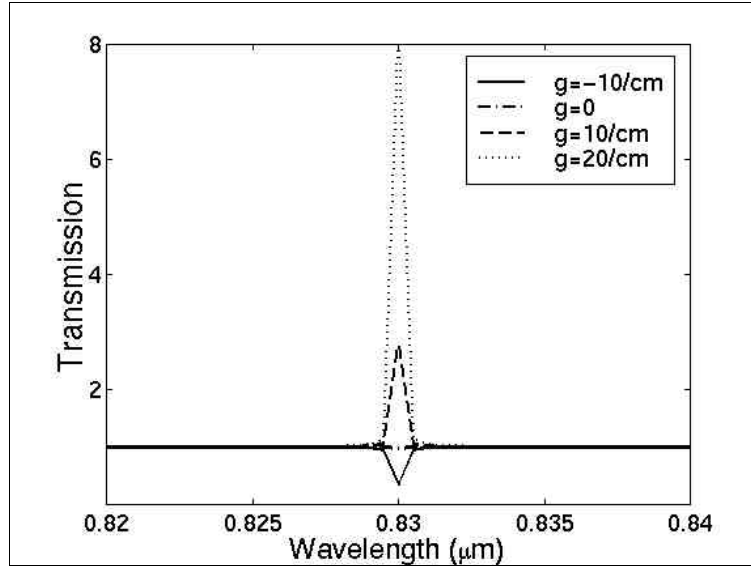


Fig. 6-3. The calculated transmission spectra of the device for different ARROW propagation gains. The calculation was performed using the coupled-mode equations (described in Chapter 3), with an assumed coupling constant of 3mm^{-1} .

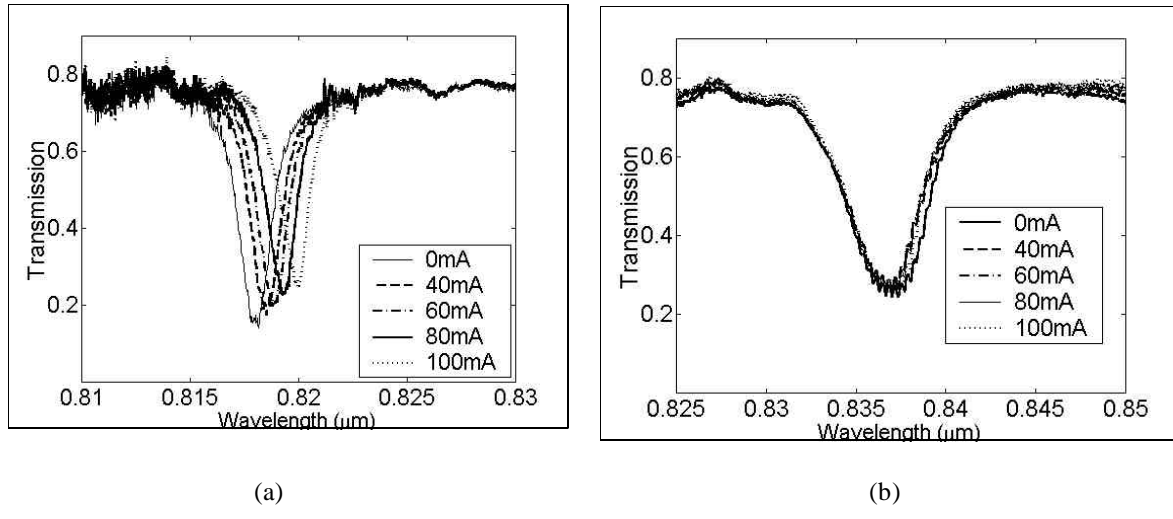


Fig. 6-4. The transmission spectra under different current injection levels for TE polarized light (a) and TM polarized light (b).

The measured transmission spectra under different current injection levels are shown in Fig. 6-4. Due to heating problems, our devices could not sustain more than 100mA. Under this injection level, no transmission gain was observed because there were not enough injected carriers to overcome the quantum well absorption loss. The sheet carrier density in the quantum well can be estimated as follows:

$$n = \frac{J\tau}{e}, \quad (6-1)$$

where J is the injection current density, τ is the carrier lifetime and e is the electronic charge. The non-implanted area of the ARROW was 2mm by 50μm, therefore 100mA of current corresponds to a current density of 100A/cm². Assuming all carriers recombine in the quantum well with a lifetime of 0.5ns,⁶³ the sheet carrier density is about $3 \times 10^{11} \text{ cm}^{-2}$, which is about an order of magnitude less than the injection level needed for transparency (i.e., loss=0).⁶³

The shift in the TE spectra is due to carrier induced refractive index change⁴² in the quantum well. There is hardly any change in the TM spectra, however, and that can be attributed to the split in the heavy and light hole bands in the quantum well. At the present injection level, most holes injected into the quantum well occupy heavy hole states because of their lower energies (Fig. 6-5). For TM polarized light, only the light hole transitions are allowed.⁶⁴ Therefore changes in the injection current result in much larger absorption (and index) changes for TE polarized light than for TM polarized light. This effect is also confirmed by the luminescence data (Fig. 6-2) where the TE emission peak red-shifts with increasing current, while the TM peak does not move.

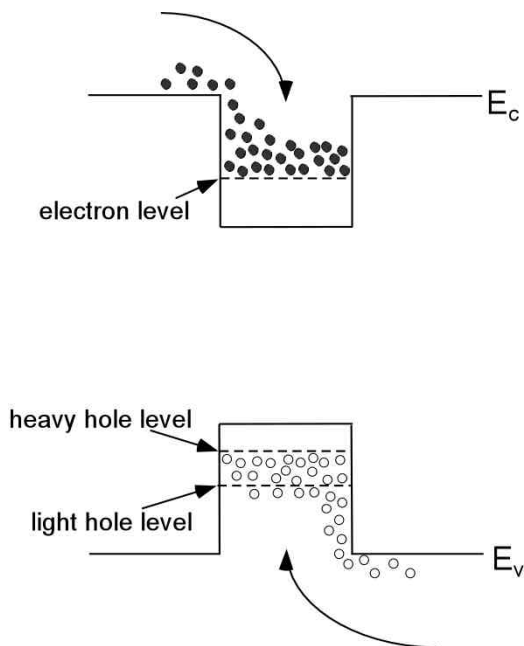


Fig. 6-5. The band diagram of a semiconductor quantum well. The split in the heavy and light hole bands results in most injected holes falling into heavy hole states.

Chapter 7

Conclusion

7.1 Summary

This thesis demonstrated proof-of-concept in-line fiber devices based on evanescent wave coupling between single mode fibers and semiconductor (GaAs) waveguides. This type of device promises to alleviate the problems of high insertion loss and high cost associated with conventional fiber device packaging, as well as to create a new device paradigm for wavelength division multiplexing applications. Due to the large index difference between glass and GaAs, DBR mirrors have to be used in the GaAs waveguide so that phase-matching can be achieved. The mirrors are designed to provide high reflection for a specific mode angle, therefore the optical wave inside the GaAs waveguide can propagate with an effective index that is much lower than the material index.

The first part of the thesis dealt with the theory and design issues of semiconductor in-line fiber devices. The transfer matrix method was used in the design of GaAs/AlGaAs ARROWS, while a simple phenomenological model (couple mode equations) was adopted to characterize the coupling behavior of the fiber-ARROW system. The experimental demonstration of a narrow linewidth filter (FWHM=0.5nm near 830nm for TE light) verified the properties of the in-line device structure. By including a quantum well absorbing layer in the core of the ARROW, a wavelength selective photodetector (FWHM=1.6nm) was demonstrated.

Next, an in-line fiber intensity modulator utilizing the quantum confined Stark effect was investigated. A multiple-quantum-well layer, whose absorption coefficient and refractive index can be changed under the influence of a vertical electric field, was placed in the ARROW core. The electric field changes the fiber transmission spectrum, therefore

intensity modulation at a given wavelength is obtained. The demonstrated device had a maximum on/off ratio of 4:1 with an applied voltage of 9V. Calculations showed that traveling wave electrodes on the ARROW are needed to obtain a high device switching speed. The speed is primarily limited by the microwave propagation loss and the speed mismatch between the microwave and optical signals. The calculated 3dB cut-off bandwidth for a 1mm long device is 11GHz.

Finally, a resonant light emitter was demonstrated by injecting current into the ARROW (same structure as the detector). Emitted photons at phase-matched wavelengths were coupled into the fiber. The current injection also resulted in transmission modulation due to carrier induced index shift.

7.2 Suggestions for future work

The work on semiconductor in-line fiber devices is still in its infancy and there are various avenues remaining for future exploration.

One of the major factors limiting the commercial viability of these devices is their polarization sensitivity, which is an inherent property of any slab dielectric waveguide. The only solution to this is by defining an ARROW ridge waveguide collinear with the fiber. The design of such a structure will likely require a complex numerical routine (such as a 3D Maxwell's equation solver). In addition, for the detector and the modulator, the quantum well layers also need to be made polarization insensitive. This is achievable by using strained quantum wells in which the degeneracy of heavy- and light-hole states is reimposed.³⁹

The interaction length and the coupling strength are two important parameters that affect the performances of an in-line device. The use of silicon V-grooves based fiber half couplers would allow for the easy control of these two parameters, making it possible to design devices tailored for specific applications. For example, as mentioned in Chapter 5, a longer interaction length can drastically increase the on/off ratio of a modulator, and it can also broaden the resonance linewidth with the use of a tapered ARROW.

It is desirable for the modulator to have a lower operating voltage. One possibility is to use coupled quantum wells, through which the field induced carrier separation

modulation effect is achieved,⁶⁵ in place of conventional MQW layers. One could also improve the ARROW cavity design (i.e., to optimize the distance between the phase-matched wavelength and the quantum well excitonic resonance), in order to minimize the operating voltage.

In the area of light emitting devices, one intriguing device possibility is an in-line fiber coupled laser. By forming an oscillator (feedback loop) with the help of fiber Bragg gratings (or a high reflectance coated air-semiconductor interface), it is possible to create a wavelength stabilized, directly fiber-coupled semiconductor laser (Fig. 7-1). This device structure could prove attractive for use as a WDM source or a fiber amplifier pump.

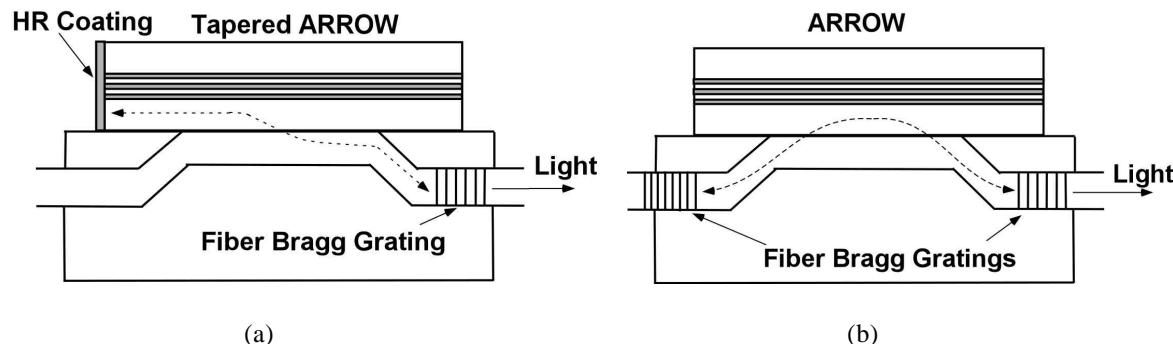


Fig. 7-1. Two possible configurations for an in-line fiber coupled semiconductor laser: (a) the feedback loop is formed between a fiber Bragg grating and a HR-coated air-semiconductor interface; (b) the feedback loop is formed between two fiber Bragg gratings.

Finally, by applying the same device concept and switching to a new material system (such as GaInNAs on GaAs, or InGaAsP on InP), one can fabricate devices operating at $1.3\mu\text{m}$ and $1.55\mu\text{m}$, which are the wavelengths of choice for fiber optic communication systems.

Appendix A

Derivation of microwave resistive loss caused by a doped semiconductor layer

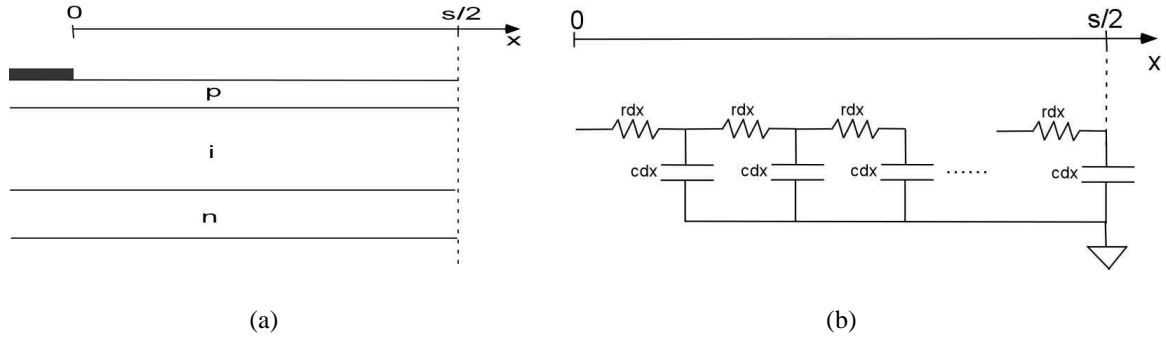


Fig. A-1 (a) The physical structure of a p-i-n diode with a p-contact; (b) An equivalent circuit model used to simulate the situation in (a).

The attenuation caused by the p-type layer in the transmission line structure shown in Fig. 5-17 can be calculated using an equivalent circuit model. The model is illustrated in Fig. A-1b. The current and voltage relationships in the circuit are described by the following differential equations,

$$\frac{\partial v(x,t)}{\partial x} = -i(x,t)r \quad (\text{A-1})$$

$$\frac{\partial i(x,t)}{\partial t} = -c \frac{\partial v(x,t)}{\partial t}, \quad (\text{A-2})$$

where i is the resistor current per unit length (into the paper), c is the capacitance per unit area, and r is the sheet resistance of the doped layer. Assuming an $\exp(j\omega t)$ dependence for i and v , with

$$v(x,t) = \text{Re}[V(x)e^{j\omega t}] \quad (\text{A-3})$$

$$i(x,t) = \operatorname{Re}[I(x)e^{j\omega t}], \quad (\text{A-4})$$

equations (A-1) and (A-2) can be converted into

$$\frac{dV(x)}{dx} = -rI(x) \quad (\text{A-5})$$

$$\frac{dI(x)}{dx} = -j\omega cV(x). \quad (\text{A-6})$$

Differentiate both sides of (A-6) and then substitute (A-5) into the resulting equation, a second order differential equation for $I(x)$ can be obtained,

$$\frac{d^2I(x)}{dx^2} = j\omega crI(x). \quad (\text{A-7})$$

The solution to (A-7) is

$$I(x) = I_0 \exp(-\sqrt{\frac{\omega cr}{2}}x) \exp(-j\sqrt{\frac{\omega cr}{2}}x). \quad (\text{A-8})$$

The solution with positive signs in the exponentials is discarded because of its non-physical nature. At $x=0$, $I(x) = I_0$, which is the amplitude of the total current going into and out of the top electrode.

The power dissipation per unit length (into the paper) w_L can now be expressed in terms of the current distribution,

$$w_L = 2 \times \frac{1}{2} \int_0^{s/2} r |I(x)|^2 dx. \quad (\text{A-9})$$

There is a factor of 2 in front because the device consists of two symmetric arms with a total length of s . (A-9) can be rearranged to yield

$$w_L = I_0^2 r \frac{1 - \exp(-s\sqrt{\pi fcr})}{2\sqrt{\pi fcr}}, \quad (\text{A-10})$$

where f is the signal frequency.

If the voltage signal at one location along the transmission line is expressed as

$$V_s = V_{s0} \cos(2\pi ft), \quad (\text{A-11})$$

then the capacitive charging current is

$$I_c = 2\pi f C_{tot} V_{s0} \cos(2\pi ft), \quad (\text{A-12})$$

where C_{tot} is the total capacitance per unit length for the transmission line. Since the amplitude of I_c should be roughly twice the value I_0 , V_{s0} can be written in terms of I_0 ,

$$V_{s0} = \frac{I_0}{\pi f C_{tot}}. \quad (\text{A-13})$$

The average power carried in the transmission line is then

$$P_{ave} = \frac{V_{s0}^2}{2Z_0} = \frac{I_0^2}{2Z_0(\pi f C_{tot})^2}, \quad (\text{A-14})$$

where Z_0 is the characteristic impedance. Under low loss conditions where the impedance Z_0 is real, the attenuation coefficient of a transmission line is given by⁵²

$$\alpha = \frac{w_L}{2P_{ave}}. \quad (\text{A-15})$$

Substituting (A-14) and (A-10) into (A-15), the final expression for the attenuation due to resistive losses in the doped layer is obtained

$$\alpha = Z_0 r (\pi f C_{tot})^2 \left[\frac{1 - \exp(-s\sqrt{\pi cfr})}{2\sqrt{\pi cfr}} \right]. \quad (\text{A-16})$$

Due to the fact that not all charging current travels laterally through the p-type layer (i.e., some current goes directly underneath the electrodes or $I_c > 2I_0$), equation (A-16) represents a slight overestimation of the attenuation.

Appendix B

Simulation of non-planar transmission lines using HP momentum

In this appendix, the validity of the method of moments as used in simulating non-planar microwave transmission lines is verified by comparing calculated results with published experimental data. The experimental structure chosen here was reported by Liao *et al.*⁵¹ and its dimensions are shown in Fig. B-1a. The structure is a traveling-wave InAsP/InGaP MQW electro-absorption modulator grown on InP for $1.3\mu\text{m}$ operation. Fig. B-1b illustrates the planar model used in the simulation. Similar to the example shown in section 5.4.2, the extra capacitance and loss caused by the top p-type layer are added manually after the simulation.

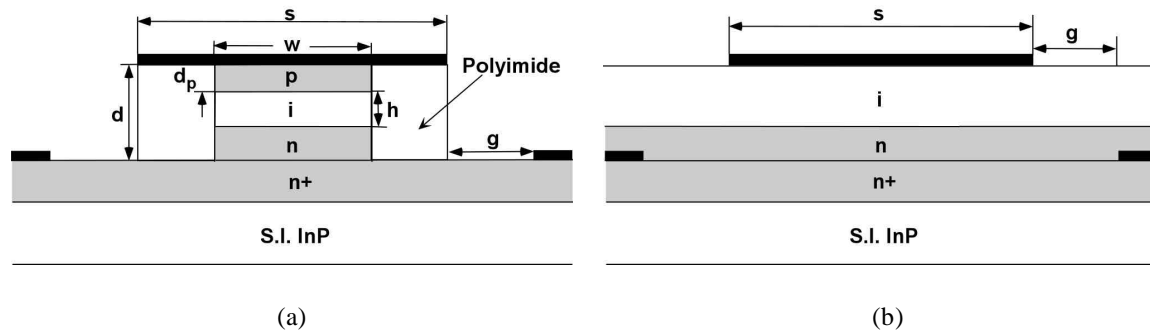


Fig. B-1. (a) The experimental transmission line structure. The dimensions are: $d=2.3\mu\text{m}$, $s=6\mu\text{m}$, $w=3\mu\text{m}$, $h=0.9\mu\text{m}$, $g=2.5\mu\text{m}$ and $d_p=0.8\mu\text{m}$. The contact metal (Au) thickness is $0.6\mu\text{m}$. (b) The model used for HP Momentum calculation.

The overall capacitance per unit length of the transmission line can be approximated as

$$C_{tot} = C_{cal} \left(\frac{w}{s} \right) \left(\frac{h + d_p}{h} \right) + \frac{\epsilon_{pm} \epsilon_0 (s - w)}{d}, \quad (\text{B-1})$$

where C_{cal} is the capacitance calculated by HP Momentum, and ϵ_{pm} is the relative dielectric constant of the polyimide material ($\epsilon_{pm} = 4$ in this case).

The capacitive current loss due to the p-type layer can be derived using the same method as shown in appendix A. If the voltage signal at one location on the transmission line is

$$V_s = V_{s0} \cos(2\pi f t), \quad (\text{B-2})$$

then the capacitive charging current per unit length is

$$I_c = 2\pi f C_{tot} V_{s0} \cos(2\pi f t) = I_0 \cos(2\pi f t), \quad (\text{B-3})$$

where C_{tot} is the total transmission line capacitance per unit length. The average power carried in the transmission line can then be expressed as

$$P_{ave} = \frac{V_{s0}^2}{2Z_0} = \frac{I_0^2}{8Z_0 \pi^2 f^2 C_{tot}^2}, \quad (\text{B-4})$$

where Z_0 is the characteristic impedance. The power dissipated per unit length in the p-type layer is

$$w_L = \frac{1}{2} I_0^2 R_p, \quad (\text{B-5})$$

where R_p is the vertical resistance per unit length (with the dimension $\Omega \cdot m$) of the layer and can be expressed as

$$R_p = \frac{d_p}{\sigma w}, \quad (\text{B-6})$$

where σ is the conductivity. Combining (B-5) and (B-4), the attenuation due to the resistive loss in the p-type layer is therefore

$$\alpha = \frac{w_L}{2P_{ave}} = 2Z_0 \pi^2 C_{tot}^2 f^2 R_p. \quad (\text{B-7})$$

In the simulation, the dielectric constant for the semiconductor layers is taken to be 12.5. The conductivities for the doped layers are derived from the doping levels and published mobility values.⁶⁴ And the numbers are: $8 \times 10^4 S/m$ (n), $4 \times 10^4 S/m$ (n+), and $400 S/m$ (p). The conductivity for the contact metal (gold) is $4.4 \times 10^7 S/m$. The

published experimental data, along with calculated values for the characteristic impedance, the attenuation coefficient and the effective index are plotted in Fig. B-2. There is close agreement between simulation and experiment. Only for the effective index is there significant error, and this can be attributed to the assumption in the model that the intrinsic and n-doped layers extend to infinity in the lateral direction.

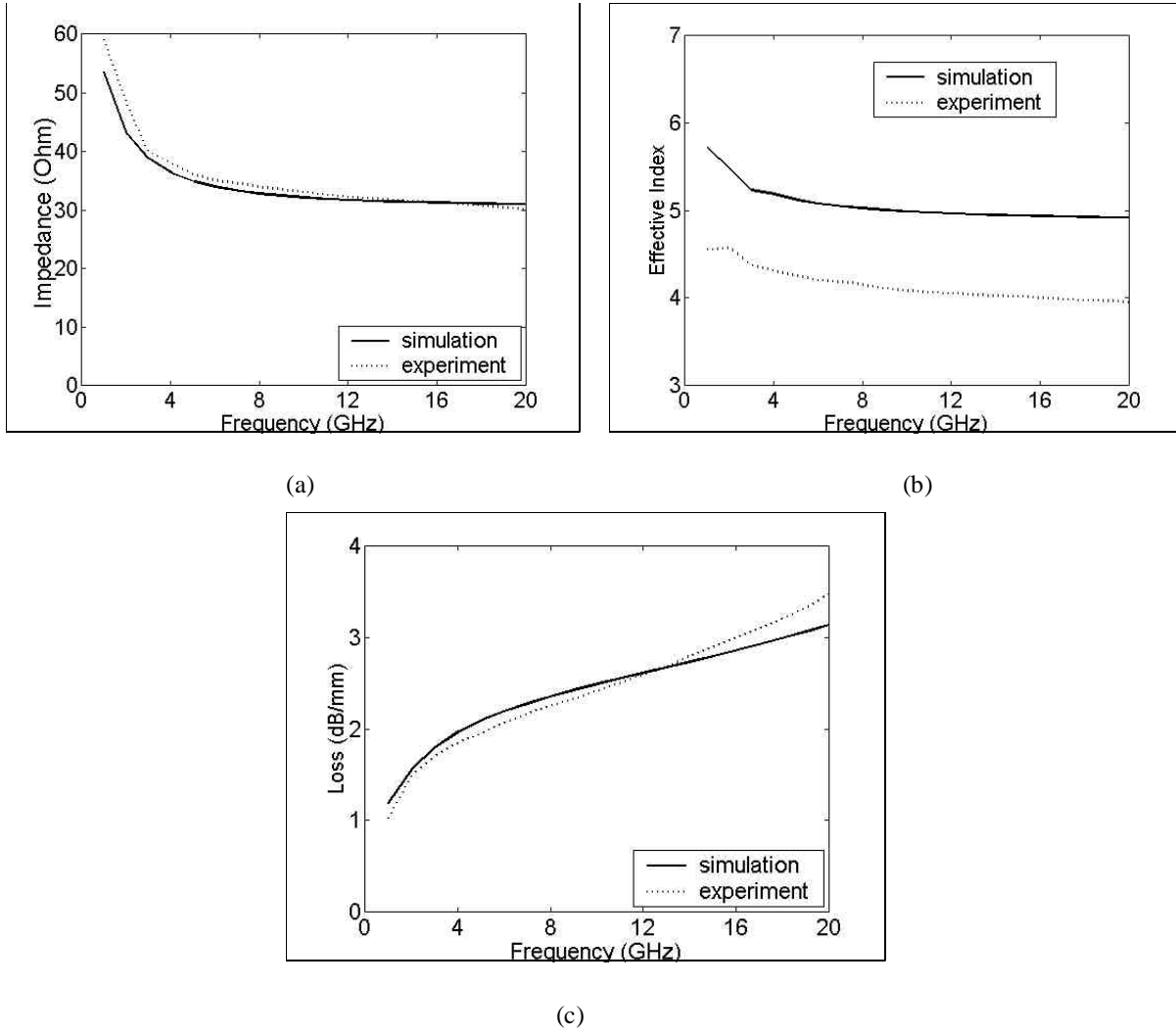


Fig. B-2. Comparison between HP Momentum simulation results and published experimental data for the structure shown in Fig. B-1.

REFERENCES

- ¹ T. H. Maiman, *Nature* **187**, 493 (1960).
- ² N. Holonyak, Jr., and S. F. Bevacqua, *Appl. Phys. Lett.* **1**, 82 (1962).
- ³ W. P. Dumke, *Phys. Rev.* **127**, 1559 (1962).
- ⁴ I. Hayashi, B. Panish, P. W. Foy, and S. Sumuski, *Appl. Phys. Lett.* **17**, 109 (1970).
- ⁵ F. P. Kapron, D. B. Keck, and R. D. Maurer, *Appl. Phys. Lett.* **17**, 423 (1970).
- ⁶ T. Miya, Y. Terunuma, T. Osaka, and T. Miyoshita, *Electron. Lett.* **15**, 106 (1979).
- ⁷ R. Heidemann, *J. Lightwave Technol.* **6**, 1693 (1988).
- ⁸ J. C. Cartledge and G. S. Burley, *J. Lightwave Technol.* **5**, 1591 (1987).
- ⁹ N. A. Olsson, *J. Lightwave Technol.* **7**, 1071 (1989).
- ¹⁰ C. R. Giles, E. Desurvire, J. R. Talman, J. R. Simpson, and P. C. Becker, *J. Lightwave Technol.* **7**, 651 (1989).
- ¹¹ H. Ishio, J. Minowa, and K. Nosu, *J. Lightwave Technol.* **2**, 448 (1984).
- ¹² Special Issue on Wavelength Division Multiplexing, *IEEE J. on Selected Areas in Comm.*, **8**, 1990.
- ¹³ Z. K. Ioannidis, J. P. Giles, and C. Bowry, *Appl. Opt.* **30**, 328 (1991).
- ¹⁴ G. Fawcett, W. Johnstone, I. Andonovic, D. J. Bone, T. G. Harvey, N. Carter, and T. G. Ryan, *Electron. Lett.* **28**, 985 (1992).
- ¹⁵ S. Creaney, W. Johnstone, and K. McCallion, *IEEE Photonics Technol. Lett.* **8**, 355 (1996).
- ¹⁶ M. A. Duguay, Y. Kokubun, T. L. Koch, and L. Pfeiffer, *Appl. Phys. Lett.* **49**, 13 (1986).
- ¹⁷ B. Pezeshki, F. F. Tong, J. A. Kash, and D. A. Kisker, *J. Lightwave Technol.* **12**, 1791 (1994).
- ¹⁸ H. A. Macleod, *Thin Film Optical Filters*, Macmillan Pub. Co., New York, 1986.
- ¹⁹ A. Ghatak, K. Thyagarajan , and M. R. Shenoy, *J. Lightwave Technol.* **LT-5**, 660

-
- (1987).
- ²⁰ A.Yariv, *Optical Electronics*, Saunders College Publishing, Philadelphia, 1991, ch. 3.
- ²¹ M. S. Stern, *IEE Proc. 135, J*, 56 (1988).
- ²² M. S. Stern, *IEE Proc. 135, J*, 333 (1988).
- ²³ W. P. Huang, C. L. Xu, and S. K. Chaudhuri, *IEEE Photonics Technol. Lett.* **4**, 148 (1992).
- ²⁴ B. E. A. Saleh and M. C. Teich, *Fundamentals of Photonics*, John Wiley & Sons, Inc., New York, 1991, ch. 7.
- ²⁵ S. Adachi, *J. Appl. Phys.* **58**, R1 (1985).
- ²⁶ D. Marcuse, *J. Lightwave Technol.* **7**, 122 (1989).
- ²⁷ K. P. Panajotov and A. Tz. Andreev, *J. Opt. Soc. Am. B.* **11**, 826 (1994).
- ²⁸ K. P. Panajotov, *J. Opt. Soc. Am. B.* **13**, 2468 (1996).
- ²⁹ A. Sharma, J. Kompella, and P. K. Mishra, *J. Lightwave Technol.* **8**, 143 (1990).
- ³⁰ H. D. Rudolph and E. G. Newmann, *Nachrichtentech. Z.* **4**, 328 (1976).
- ³¹ A.Y. Cho and J. R. Arther, *Progr. Solid State Chem.*, **10**, 157 (1975).
- ³² M.A. Herman and H. Sitter, *Molecular Beam Epitaxy: fundamentals and current status*, Springer-Verlag, New York, 1989.
- ³³ K. Bacher, B. Pezeshki, S.M. Lord, and J.S. Harris, Jr., *Appl. Phys. Lett.* **61**, 1387 (1992).
- ³⁴ A.Yariv, *Optical Electronics*, Saunders College Publishing, Philadelphia, 1991, ch.4.
- ³⁵ R. A. Bergh, G. Kotler, and H. J. Shaw, *Electron. Lett.* **16**, 260 (1980).
- ³⁶ J. Talghader and J. S. Smith, *Appl. Phys. Lett.* **66**, 335 (1995).
- ³⁷ S.-M. Tseng and C.-L. Chen, *Appl. Optics* **31**, 3438 (1992).
- ³⁸ J. E. Bowers and C. A. Burrus, *Electron. Lett.* **22**, 905 (1986).
- ³⁹ S. Chelles and P. Voison, *Proceedings of Semiconductor Heteroepitaxy: Growth Characterization and Device Applications*, Montpellier, France, 1995, pp. 457.
- ⁴⁰ T. Okiyama, H. Nishimoto, I. Yokota and T. Touge, *J. Lightwave Technol.* **6**, 1686 (1988).
- ⁴¹ S. K. Korotky, G. Eisenstein, A. H. Gnauck, J. J. Veselka, R. C. Alferness, L. L. Buhl, C. A. Burrus, T.C.D. Huo, L.W. Stulz, K.C. Nelson, L.G. Cohen, R.W. Dawson, and

-
- J.C. Campbell, *J. Lightwave Technol.* **3**, 1027 (1985).
- ⁴² B.R. Bennett, R.A. Soref, and J.A. Del Alamo, *IEEE J. Quantum Electron.* **26**, 113 (1990).
- ⁴³ D.A.B. Miller, D.S. Chemla, T.C. Damen, A.C. Gossard, W. Wiegmann, T. H. Wood and C.A. Burrus, *Phys. Rev. B* **32**, 1043 (1985).
- ⁴⁴ B. Pezeshki, Ph.D. thesis, Stanford University, 1991.
- ⁴⁵ N. Peyghambarian, S. Koch and A. Mysyrowicz, *Introduction to Semiconductor Optics*, Prentice Hall, Englewood Cliffs, 1993.
- ⁴⁶ D.S. Chemla, *Physics Today*, 57 (May 1985).
- ⁴⁷ J.A. Trezza, Ph.D. thesis, Stanford University (1995).
- ⁴⁸ L.E. Franks, *Signal Theory*, Prentice Hall, Englewood Cliffs, NJ, 1969.
- ⁴⁹ P. J. Stevens, M. Whitehead, G. Parry, and K. Woodbridge, *IEEE J. Quantum Electron.* **24**, 2007 (1988).
- ⁵⁰ S.A. Hamilton, D.R. Yankelevich, A. Knobles, R.A. Hill, R.T. Weverka, and G.C. Bjorklund, *LEOS '97 34th Annual Meeting*, San Francisco, 1997, pp.387.
- ⁵¹ H.H. Liao, X.B. Mei, K.K. Loi, C.W. Tu, P.M. Asbeck, and W.S.C. Chang, *Proc. SPIE*. **3006**, 291 (1997).
- ⁵² See for example, S. Ramo, J.R. Whinnery, and T. van Duzer, *Fields and waves in Communication Electronics*, John Wiley & Sons Inc., New York, 1994.
- ⁵³ I. Kim, M.R.T. Tan, and S.Y. Wang, *J. Lightwave Technol.* **8**, 728 (1990).
- ⁵⁴ M.M. Mihailidi, J.E. Zucker, M.D. Feuer, M.N. Khan, T.Y. Chang, and N.J. Sauer, *Microwave and Optical Technol. Lett.* **10**, 204 (1995).
- ⁵⁵ S. Ramo, J.R. Whinnery, and T. van Duzer, *Fields and waves in Communication Electronics*, John Wiley & Sons Inc., New York, 1965.
- ⁵⁶ R. Harrington, *IEEE Antennas and Propagation Magazine* **32**, 31 (1990).
- ⁵⁷ W.R. Eisentadt and Y. Eo, *IEEE Trans. Components, Hybrids, and Manufac. Technol.* **15**, 483 (1992).
- ⁵⁸ G.L. Li, C.K. Sun, S.A. Pappert, W.X. Chen, and P.K.L. Yu, *IEEE Trans. Microwave Theory and Technol.* **47**, 1177 (1999).

-
- ⁵⁹ D. Avanzo, *IEEE Trans. Electron. Dev.* **29**, 1053 (1982).
- ⁶⁰ P. Ressel, H. Strusny, S. Gramlich, U. Zeimer, J. Sebastian, and K. Vogel, *Electron. Lett.* **29**, 918 (1993).
- ⁶¹ J. P. Biersack and J.F. Ziegler, 1995.
- ⁶² D. Costa, Ph.D. thesis, Stanford University, 1991.
- ⁶³ See for example, J. Singh, *Physics of Semiconductors And Their Heterostructures*, McGraw-Hill, Inc., New York, 1993, ch.15.
- ⁶⁴ See for example, S.L. Chuang, *Physics of Optoelectronic Devices*, John Wiley and Sons, Inc., New York, 1995, ch. 9.
- ⁶⁵ J.A. Trezza, M.C. Larson, S.M. Lord, and J.S. Harris, Jr., *J. Appl. Phys.* **74**, 1972 (1993).